aerospace

MDPI

Article

Structural Effects of Spatially Non-Uniform Evolution of Material Parameters Under Cyclic Thermo-Mechanical Loading

Peng Yang, Yixiang Huangfu, Jing Xiang, Xiaofeng Yang, Dong Wei, Lei Liu * and Yewei Gui

State Key Laboratory of Aerodynamics, Mianyang 621000, China; ypsaumicro@outlook.com (P.Y.); hfyx280716@foxmail.com (Y.H.); jingxiang1230608@163.com (J.X.); xiaofeng.yang@cardc.cn (X.Y.); wei_dong2020@126.com (D.W.); guiyewei777@126.com (Y.G.)
* Correspondence: liulei_9110176@163.com

Abstract

Metallic thermal protection structures of reusable high-speed vehicles experience aerodynamic heating, high-temperature hold, and cooling in each flight mission, and the hot and cold faces accumulate different temperature and plasticity histories; after multiple missions, the elastic modulus, yield strength, cyclic hardening parameters, and thermal conductivity no longer vary only with mission count, but form a spatial field varying jointly with position and mission count. This paper establishes a mission-to-mission, spatially local property update method: each mission solves the thermo-mechanical response with the current property field. At the end of the mission, the thermal exposure and plasticity accumulation at each integration point are extracted, and the material properties are updated through an evolution relation driven by the dual histories, for use in the next mission; the method is embedded in a non-isothermal Chaboche–Perzyna viscoplasticity program. Under a unified mission profile, a thin plate, a perforated plate, and a thick plate are computed for 50 missions each, that is, 50 thermo-mechanical loading cycles in sequence, with pointwise update (Case C) as the reference and no evolution (Case A) and uniform update (Case B) as comparisons. The results show that ignoring evolution gives higher structural stresses than the evolution-tracking case, with the peak-stress deviation not exceeding about 7% for the reference parameter set over the 50 missions (thin plate 4.2%, perforated plate 6.8%, thick plate less than 0.1%). Assessing the strength margin with the current, degraded strength rather than the peak stress alone shows that ignoring evolution reduces the margin by 12.2% of the reference margin in both the thin plate and the perforated plate, so that the treatment is conservative for these two structures, but only slightly so; the thick plate is marginally non-conservative, by a negligible amount. Ignoring evolution continuously underestimates the damage accumulation, with the maximum accumulated equivalent plastic strain underestimated by about 11.6% at the thin-plate hot face and about 6.0% at the perforated-plate hole edge, biasing life assessment toward the non-conservative side. At mission 50, uniform update deviates by only 0.4% in the thin plate with a mild degradation distribution, and by no more than 1% in the perforated plate with concentrated degradation; over the whole 50-mission window, the largest deviations are about 1.5% and 1.6%, respectively. The evolution parameters are assumed rather than calibrated, so the quantitative results are a sensitivity study rather than experimentally validated predictions.

Keywords: reusable; metallic thermal protection structure; evolution; spatially non-uniform degradation; non-isothermal cyclic viscoplasticity

Check for updates

Academic Editor: Xiao-Wei Gao

Received: 4 September 2026
Revised: 29 September 2026
Accepted: 4 October 2026
Published: 9 October 2026

Copyright: © 2026 by the authors. Licensee MDPI, Basel, Switzerland. This article is an open access article distributed under the terms and conditions of the Creative Commons Attribution (CC BY) license.

1. Introduction

Reusable high-speed vehicles repeatedly experience aerodynamic heating, high-temperature hold, cooling, and ground cooling processes during multiple flight missions. Each mission produces a significant temperature gradient in the thermal protection structure and, under the combined effect of thermal expansion constraints and aerodynamic pressure, forms complex stresses and plastic deformation [1–3]. With the development of reusable launch vehicles, the design service life of metallic thermal protection structures has reached tens to hundreds of missions [4,5]; structural design must not only judge whether the first mission is safe, but also evaluate the change in material properties after multiple missions and whether such change degrades the insulation and load-bearing capacity of the structure. If the design does not consider the influence of material property evolution on the structural response, prediction deviations in the cold-face temperature, cold-face heat flux, stress peak position, and plastic zone extent may arise, which in turn affect the thermal protection thickness design, reuse count assessment, and in-service inspection location determination.

Metallic thermal protection structures possess high-temperature resistance, impact resistance, maintainability, and reusability, and are among the important forms of thermal protection systems for high-speed vehicles [6,7]. GH4169 (Inconel 718) has good high-temperature strength, oxidation resistance, and machinability, and has been used in aero-engines, rocket engines, and other high-temperature load-bearing components [8,9]. Under repeated thermo-mechanical loading, its elastic modulus, yield strength, cyclic hardening parameters, and thermal conductivity may evolve irreversibly with thermal exposure and plasticity accumulation [9,10]; because different positions of the structure experience different temperature and plasticity histories, the material properties after multiple missions not only change with mission count but also form spatial differences within the structure.

For this material state, which varies with service history, engineering analysis usually adopts two treatments: the first does not track the mission-to-mission evolution of material properties, and all missions are computed with the initial properties; the second reduces the material properties with a spatially uniform property retention factor, with the reduction amplitude determined by a representative service history [9,10]. Both treatments simplify the data input and state update, but at the cost of respectively ignoring the inter-mission property evolution effect itself and the spatial non-uniformity of that evolution. How large these ignored structural effects are and whether they affect design decisions is currently not well understood at the structural level.

To clarify the meaning of the two treatments, this paper expresses the material property at position x in mission N as

$$P_i(x, t, N) = P_{i,0}[T(x, t)] r_i(x, N), \tag{1}$$

where $P_{i,0}(T)$ denotes the reversible change in the material property with the current temperature, and $r_i(x, N)$ is the property retention factor, representing the remaining proportion of the property after multiple missions, with an initial value of 1 and decreasing irreversibly with the service history. Even if the material property does not undergo long-term evolution, a non-uniform temperature field still makes $P_{i,0}[T(x, t)]$ vary with position; this instantaneous property difference caused by the current temperature can already be described by conventional temperature-dependent material models. This paper focuses on whether the retention factor $r_i(x, N)$ forms a spatial distribution because of different local service histories, and whether such a distribution affects the structural response of subsequent missions.

https://doi.org/10.3390/aerospace13100920

The evolution laws of material properties are usually obtained from low-cycle fatigue, thermo-mechanical fatigue, or high-temperature exposure tests. The temperature and nominal stress/strain distributions in the gauge section of a standard specimen are approximately uniform [11–13]; the test results are therefore usually expressed as a relation between the material property and the accumulated service history:

$$r_i = f_i(H), \tag{2}$$

where H is the accumulated history of temperature, plastic strain, etc., experienced by the specimen. Because each position in the gauge section experiences nearly identical test conditions, the test yields a single property value or one evolution curve, rather than a spatial distribution of properties in an actual structure. When Equation (2) is applied to structural analysis, the same calibration relation f_i applies to all material points, but each point should input its own local history:

$$r_i(x, N) = f_i[H(x, N)]. \tag{3}$$

Since the temperature peak, high-temperature dwell time, stress level, and plasticity accumulation differ among positions, the retention factor given by Equation (3) generally varies with position. If instead a representative history $H^{rep}(N)$, such as the mean temperature, the mean plasticity accumulation, or the history of a representative position, is input into Equation (2), the resulting retention factor is a scalar without spatial position:

$$r_i^U(N) = f_i[H^{rep}(N)], \tag{4}$$

When it is applied to the entire structure, all material points adopt the same retention factor:

$$P_i^U(x, t, N) = P_{i,0}[T(x, t)] r_i^U(N). \tag{5}$$

This paper refers to this treatment as "uniform update" (Case B): "uniform" only means that the retention factor is identical in space; the material property can still vary with the local temperature through $P_{i,0}(T)$, but the degradation difference formed by different service histories at each point is ignored. The first question studied in this paper concerns the influence of the spatial non-uniformity of material property evolution on the structural response, that is, how and whether the structural response differs when the retention factor at each point varies with position (Equation (3)) compared with a scalar given by a representative history (Equation (5)).

Besides the spatial distribution, there is also a mission-to-mission mutual influence between the material property evolution and the temperature and stress fields: the local temperature and plastic deformation in the current mission determine the thermal exposure and plasticity accumulation, thereby driving the property evolution. The evolved thermal conductivity, elastic modulus, yield strength, and cyclic hardening parameters in turn change the temperature field, stress field, and plastic deformation of the next mission, thereby affecting the next evolution. The second question studied in this paper concerns the effect of this mission-to-mission feedback, that is, the inter-mission property evolution effect itself, on the structural response, and how the prediction of the structural response changes when this feedback is ignored.

To address these questions, the existing studies are reviewed from two aspects: structural design and material models. At the structural design level, the transient heat transfer and thermo-mechanical analysis methods for metallic thermal protection structures are relatively complete, covering the transient thermo-mechanical response of superalloy thermal protection structures under aerodynamic heating [14], the thermo-mechanical behavior

of honeycomb sandwich panels under non-steady thermal loading [15], and the optimal design of thermal protection structures considering thermo-mechanical properties [16]. Structural design studies of reusable launch vehicles have also been extensively carried out, covering multidisciplinary optimization of the overall configuration [17], material design for extreme environments [18], and system-level technical reviews [5]. These works provide a basis for the structural response computation under repeated missions; however, in these works, the material properties usually vary only with the current temperature, and the property evolution formed by the service history after multiple missions has not yet entered structural design.

At the material model level, unified viscoplastic constitutive models can describe cyclic hardening, back-stress evolution, and strain-rate effects [19–22], but their internal variables retain only the cyclic state within the current mission, and the elastic modulus, thermal conductivity, and other material properties themselves do not undergo long-term changes over multiple missions. Continuum damage mechanics and material degradation models mostly describe property degradation with a single damage variable or temperature–time equivalent parameters [23–28], with the coupling between degradation and response limited to the same loading process; such models are oriented toward material points or damage and crack behavior.

Based on the literature survey, existing studies of metallic thermal protection panels have not addressed, at the structural level, the response deviations caused by spatially non-uniform property evolution. The above two aspects of research provide this paper with structural response computation methods and pointwise update tools. On this basis, this paper sets up comparison cases of three update treatments under completely identical structure, loading, and evolution laws, and examines the structural dependence of the above effects with three structures—a thin plate, a perforated plate, and a thick plate—answering when inter-mission property evolution must be considered in design and when simplified treatments can be adopted.

Spatially varying creep and oxidation damage in cooled turbine components has been studied extensively [22,25,26], and history-dependent property loss governing subsequent structural behavior is likewise recognized in repeated-load and deployable-structure contexts [29,30]. The gap addressed here is therefore not the absence of degradation or of load-history tracking in general, but the lack of a spatially resolved, dual-history-driven description of property evolution for metallic thermal protection panels, together with a quantification of how the choice of spatial treatment of that evolution propagates into the structural response. Existing structural studies of metallic thermal protection systems use either temperature-dependent properties only or a single uniform degradation factor, so that the interaction between the spatial non-uniformity of the property field and the stress and temperature fields of the panel itself remains unquantified.

Life-assessment arguments that ignore the degradation feedback are also known to bias the estimate toward the non-conservative side in other structural contexts [31,32], which motivates the present rate-, temperature- and stress-state-dependent of failure within a Perzyna-type overstress formulation rather than rate-independent plasticity. Creep and time-dependent deformation must likewise be characterized experimentally before being embedded in a constitutive framework [33], and the irreversible property changes accumulated over a thermo-mechanical history have a measurable physical basis rather than resting on a purely phenomenological construct [34].

Finally, the pointwise degradation maps obtained in Section 4.1 identify the locations at which process-level repair would be required, such as the hole edge and the hot face, connecting the spatial degradation results to repair modeling [35].

To study the above questions, this paper first establishes a mission-to-mission, spatially local material property update method: each mission solves the thermo-mechanical response with the current material property field; after the mission, the thermal exposure and plasticity accumulation at each integration point are extracted, and the material properties are updated for the next mission. The property evolution adopts a phenomenological form driven by the dual histories of thermal exposure and plasticity accumulation; this form is a replaceable model component; its parameters are assumed rather than calibrated, with the variation trends taken from existing GH4169 test data and literature results; the method is embedded in a non-isothermal Chaboche–Perzyna viscoplasticity constitutive program, with mission-to-mission sequential thermo-mechanical coupling.

Under this framework, three comparison cases are set up. Case A does not consider the inter-mission evolution of material properties; it corresponds to the current analysis practice that does not track evolution. Case B updates the material properties with a spatially uniform history, corresponding to the spatially uniform retention factor treatment (the field-reduction rule adopted for the uniform history depends on the structure: the thin plate takes the volume average, and the perforated plate takes the field maximum). Case C updates the material properties separately with the local history of each point, corresponding to the pointwise evolution-tracking practice. The three cases adopt identical geometric models, mission profiles, initial material parameters, boundary conditions, and finite element meshes, differing only in the material property update method; the difference between Case A and Case C gives the inter-mission property evolution effect itself, and the difference between Case B and Case C gives the contribution of the spatial non-uniformity of that evolution.

To examine the role of structural features, two variants are set up on the basis of the thin plate ($50 \times 50 \times 5$ mm, baseline): a perforated plate (central in-plane hole $d = 10$ mm) and a thick plate (thickness 20 mm); a single variable difference is maintained among the structures, each executing 50 missions; the structural setup is given in Section 3.1.

The main contributions of this paper are threefold. First, the structural effects of mission-to-mission, spatially non-uniform evolution of material properties are given: three structures—a thin plate, a perforated plate, and a thick plate—cover the complete range from strong degradation to weak degradation, with the degradation of the perforated plate concentrated at the hole edge. The mission-to-mission acceleration of the in-service plasticity accumulation (about threefold within 50 missions) is found, with the cyclic constitutive behavior as the main cause, on top of which property degradation further reduces the hardening parameters, making the accumulation faster and widening the spatial gap; the deviations caused by the two common simplified treatments are quantitatively given.

Keeping the properties unchanged overestimates the structural stress in strength checks, with the design conservative for the thin plate and the perforated plate (not exceeding about 7% for the reference parameter set within the 50-mission window) and marginally non-conservative for the thick plate by a negligible amount. The same treatment underestimates the damage accumulation used in life assessment, biasing the assessment toward the non-conservative side (about 11.6% for the thin plate and about 6.0% at the perforated-plate hole edge). The deviation of the uniform update from the pointwise update grows as the degradation distribution becomes less uniform: at mission 50, it is about 0.4% for the thin plate with a mild degradation distribution and about 1% for the perforated plate with degradation concentrated at the hole edge; over the whole window, the largest deviations are about 1.5% and 1.6%, respectively. The retention factor of the uniform update is, however, more conservative than the pointwise hole-edge value, because the representative history is taken as the field maximum. In addition, the field-uniform thermal conductivity degradation alters the temperature field itself. The results provide a

basis for thermal protection thickness design, in-service inspection location determination, and reuse count assessment.

Second, a mission-to-mission, spatially local property update method supporting the above comparison is established, extending the material properties after multiple missions from a scalar varying with mission count to a spatial field varying jointly with position and mission count, with the property evolution relation being replaceable.

Third, the method is embedded in a non-isothermal cyclic viscoplasticity constitutive program and realizes mission-to-mission feedback among material properties and the temperature and stress fields; the correctness of history accumulation, property mapping, and inter-mission activation is verified through layered cases with prescribed history paths.

2. Theoretical Model and Program Verification

This paper takes a single thermo-mechanical mission as the advancement unit. Within each mission, the temperature field and cyclic viscoplastic response are solved using the current material parameters; at the end of the mission, the temperature and plasticity histories are extracted from the material integration points, the material properties for the next mission are updated, and the plastic strain, kinematic hardening internal variables, and isotropic hardening variable are transferred. The intra-mission material response adopts the Chaboche–Perzyna model, and the inter-mission property change is driven by the thermal exposure and accumulated plastic deformation.

The computation adopts the small-strain and quasi-static assumptions (the ratio of the characteristic times of thermal diffusion and elastic wave propagation is about 10^6 at the model scale of this paper). Within a single mission, thermal analysis and mechanical analysis are performed sequentially; the material property retention factor remains unchanged within one mission interval and is updated at the end of the mission. Plastic dissipation heat, thermoelastic coupling heat, oxygen diffusion, crack initiation, and crack propagation are not included in the current model. This paper assumes that material properties change monotonically with accumulated mission history; the corresponding evolution curves and parameters are assumed rather than calibrated, with the variation trends taken from the GH4169 test data and literature results of Section 2.2.3.

2.1. Mission-to-Mission Material Parameter Driving Method

Let N denote the mission index, x the material point position, and T the current temperature. The i-th class of material parameter is written as

$$P_i(x, T, N) = P_{i,0}(T) r_i(x, N), i \in \{E, k, C, \sigma_y, Y_{sat}\}. \tag{6}$$

where $P_{i,0}(T)$ is the temperature-dependent parameter in the absence of inter-mission property change, and $r_i(x, N)$ is the property retention factor at the beginning of mission N. The material properties whose evolution is considered in this paper include the elastic modulus E, thermal conductivity k, kinematic hardening modulus C, initial yield strength σ_y, and saturated cyclic yield strength Y_{sat}.

Equation (6) separates the reversible change produced by the current temperature from the inter-mission change produced by accumulated service history. Even when $r_i = 1$, the material parameter can still vary with the local temperature; when r_i varies with position, the material property also contains a spatial difference formed by the local service history.

Before the first mission,

$$r_i(x, 1) = 1, h_p(x, 1) = 0, h_T(x, 1) = 0, \tag{7}$$

where h_p and h_T, respectively, denote the plasticity accumulation and thermal exposure accumulation used for property update.

Mission N uses $r_i(x, N)$ to compute the temperature and mechanical responses. At the end of the mission, the history variables at each integration point are updated according to

$$h_a(x, N+1) = h_a(x, N) \ + \Delta h_a(x, N), a \in \{p, T\} \tag{8}$$

The retention factor is then determined from the updated accumulated history:

$$r_i(x, N+1) \ = \ f_i\big[h_p(x, N+1), h_T(x, N+1)\big]. \tag{9}$$

Equation (8) represents the local update form. When a spatially uniform update is adopted, Δh_a is first reduced to a single spatially uniform value by the field-reduction rule adopted for the structure (volume average or field maximum), and then the uniform accumulated history is updated; the specific configuration is given in Section 3.4.

The constitutive state to be read at the beginning of a mission includes the plastic strain ε^p, accumulated equivalent plastic strain p, kinematic hardening internal variables α_j, and isotropic hardening variable R. At the end of the mission, the terminal values of these variables serve as the initial values of the next mission:

$$\begin{aligned} \varepsilon^p_{N+1} &= \varepsilon^{p,end}_N, \\ p_{N+1} &= p^{end}_N, \\ \alpha_{j,N+1} &= \alpha^{end}_{j,N}, \\ R_{N+1} &= R^{end}_N. \end{aligned} \tag{10}$$

After the property parameters are updated, the next mission starts from the end-of-mission temperature and constitutive state; the retention factor takes effect at the beginning of the next mission (lagged activation). The program saves and transfers state variables between missions according to this definition. The mission-to-mission computation procedure is shown in Figure 1: each mission sequentially completes the thermal analysis, the mechanical analysis, and the end-of-mission property update, and then transfers the end-of-mission temperature field and constitutive state to the next mission, proceeding cyclically up to the prescribed total number of missions.

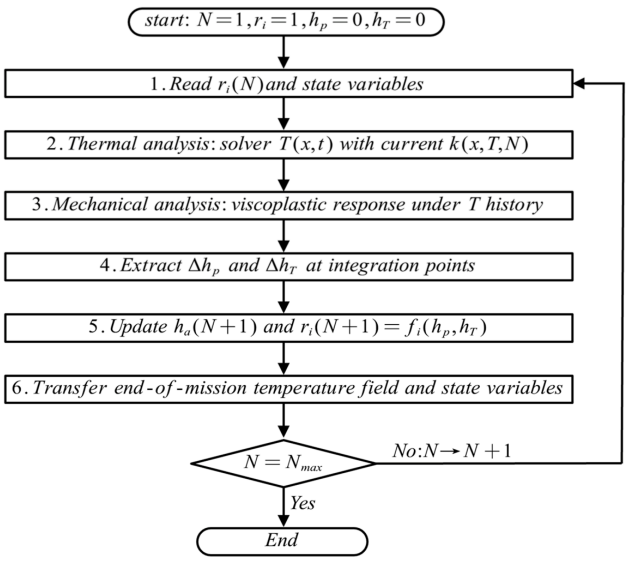


Figure 1. Mission-to-mission material parameter driving and state transfer procedure.

2.2. Constitutive Relation and Property Evolution

2.2.1. Non-Isothermal Chaboche–Perzyna Viscoplasticity

The total strain is decomposed into elastic, plastic, and thermal parts:

$$\varepsilon = \varepsilon^e + \varepsilon^p + \varepsilon^{th}. \tag{11}$$

The thermal strain is

$$\varepsilon^{th}(T) = [\int_{T_{sf}}^{T} a_T(\theta) d\theta] I, \tag{12}$$

where a_T is the coefficient of linear thermal expansion, T_{sf} is the stress-free temperature (taken as 20 °C), and I is the second-order identity tensor.

The stress is computed by Hooke's law:

$$\sigma = D_e(E, \nu) : \left(\varepsilon - \varepsilon^p - \varepsilon^{th}\right) \tag{13}$$

where D_e is the elastic stiffness tensor and ν is Poisson's ratio.

The elastic modulus adopts

$$E(x, T, N) = E_0(T) r_E(x, N). \tag{14}$$

The total back stress is

$$X = \sum_{j=1}^{n_b} X_j, \tag{15}$$

Let s be the stress deviator; the equivalent stress accounting for the back stress is

$$q = \sqrt{\frac{3}{2}(s - X) : (s - X)}. \tag{16}$$

The current yield surface radius is written as

$$Y = \sigma_y(x, T, N) + R, \tag{17}$$

where

$$\sigma_y(x, T, N) = \sigma_{y0}(T) r_\sigma(x, N). \tag{18}$$

The yield function is

$$F = q - Y. \tag{19}$$

The Perzyna viscoplastic flow relation takes the form

$$\dot{p} = \gamma_0(T) \left[\frac{max(F, 0)}{\sigma_{ref}(x, T, N)}\right]^{m(T)}, \tag{20}$$

$$\dot{\varepsilon}^p = \frac{3}{2} \dot{p} \frac{s - X}{q}. \tag{21}$$

When $q = 0$, $\dot{\varepsilon}^p = 0$ is taken. Here, γ_0 and m are rate-dependent parameters, and the reference stress is taken as

$$\sigma_{ref} = \sigma_{y0}(T) r_\sigma(x, N) + R. \tag{22}$$

That is, the reference stress is taken as the current yield surface size Y (Equation (17)). In the softening stage ($R < 0$), the reference stress decreases accordingly; under the same boundary displacement, the overstress $max(F, 0) = q - Y$ increases while the normaliza-

tion basis $\sigma_{ref} = Y$ decreases, and the viscoplastic flow rate increases significantly; this convention is consistent with the σ^0 of the Abaqus built-in *RATE DEPENDENT.

The kinematic hardening takes the kinematic hardening internal variable α_j as the state variable; its evolution relation and the corresponding back stress are

$$\begin{aligned} \dot{\alpha}_j &= \dot{\varepsilon}^p - \gamma_j(T)\alpha_j\dot{p}, \\ X_j &= \tfrac{2}{3}C_j(x,T,N)\alpha_j. \end{aligned} \tag{23}$$

where

$$C_j(x,T,N) = C_{j0}(T)r_C(x,N). \tag{24}$$

The current model adopts the same inter-mission retention factor r_C for the kinematic hardening moduli corresponding to each internal variable, while C_{j0} and γ_j can take different values for different components and temperatures. The back stress X_j is not saved as an independent history state, but is computed from the saved α_j and the current C_j according to Equation (23).

The isotropic hardening relation is written as

$$\dot{R} = b(T)[R_{sat}(x,T,N) - R]\dot{p}, \tag{25}$$

where

$$R_{sat} = Y_{sat,0}(T)r_{sat}(x,N) - \sigma_{y0}(T)r_\sigma(x,N). \tag{26}$$

When $R_{sat} > 0$, the yield surface radius increases with plasticity accumulation; when $R_{sat} < 0$, the model exhibits cyclic softening. The computation requires $\sigma_y + R > 0$.

At the mission boundary, ε^p, p, α_j, and R are transferred continuously. When material parameters are updated, no preset instantaneous scaling is applied to α_j or R; since X_j is derived from the current C_j and α_j, the back stress can change accordingly after C_j is updated; the magnitude of this change does not exceed the degradation amplitude of r_C (no more than about 8% in the present cases).

The Chaboche–Perzyna model is used to compute the rate-dependent cyclic deformation and stress relaxation under a given mission profile, covering the main deformation processes within the mission time scale of this paper. The above model relations are derived from references [36,37]. The parameters of these relations are assumed in this paper rather than calibrated against dedicated tests: creep and time-dependent deformation must be characterized experimentally before being embedded in a constitutive framework [33], and the premise that a thermo-mechanical history leaves an irreversible change in the properties is likewise not a purely phenomenological construct but one with a measurable physical basis in the alloy [34]. The rate-, temperature- and stress-state-dependent form adopted here, in preference to rate-independent plasticity, reflects the fact that these three variables jointly control failure in other material classes as well [31,32].

2.2.2. Local Plasticity History and Thermal Exposure History

The dimensionless plasticity history increment within mission N is defined as

$$\Delta h_p(x,N) = \frac{1}{p_{ref}}\int_0^{t_{cyc}} \dot{p}(x,t,N)dt = \frac{\Delta p(x,N)}{p_{ref}}, \tag{27}$$

where p_{ref} is the reference accumulated equivalent plastic strain and t_{cyc} is the duration of a single mission. The integration range covers heating, high-temperature hold, cooling, and post-mission cooling stages.

The constitutive state variable p participates in the constitutive integration of the current mission; the dimensionless accumulated history h_p accumulates $\Delta p/p_{ref}$ mission by mission and is used for inter-mission property update. In the spatially uniform configuration, h_p is reduced to a single spatially uniform value of the dimensionless increments by the field-reduction rule adopted for the structure (volume average or field maximum, Section 3.4), while p still evolves independently at each integration point.

The dimensionless thermal exposure history increment within mission N adopts the normalized temperature-compensated time:

$$\Delta h_T(x,N) = \frac{1}{t_{ref}} \int_0^{t_{cyc}} \exp\left[-\frac{Q}{R_g}\left(\frac{1}{T(x,t,N)} - \frac{1}{T_{ref}}\right)\right] dt, \tag{28}$$

where t_{ref} is the reference time, Q is the effective activation energy, R_g is the gas constant, and all temperatures are on the absolute scale. When $T = T_{ref}$, an exposure lasting t_{ref} corresponds to a unit thermal exposure history increment.

Both h_p and h_T are dimensionless accumulated histories that represent the contributions of plasticity accumulation and thermal exposure to material property change. This paper treats the two types of history as two separable phenomenological channels and examines the influence of each channel and their combination on the structural response through control cases.

2.2.3. Property Retention Factor

For the i-th class of material property and history channel a, the normalized history is defined as

$$u_{a,i} = min(\frac{h_a}{h_{c,a,i}}, 1), a \in \{p, T\}, \tag{29}$$

where $h_{c,a,i}$ is the dimensionless characteristic history of the i-th property under history channel a; it is dimensionless, same as h_a, and represents the history that needs to be accumulated for the property change in that class under that channel to reach the saturation amplitude. If the value is too small, the evolution saturates after the first few missions; if too large, the material barely evolves within its service life. This paper does not carry out dedicated calibration tests; $h_{c,a,i}$ is estimated to a reasonable order of magnitude from fatigue and creep data and then reasonably assumed (the order-of-magnitude constraint is given at the end of this section). For engineering applications, $h_{c,a,i}$ can be calibrated from tests dominated by a single channel: the thermal exposure channel is determined by high-temperature exposure tests measuring the evolution of properties with hold time, converted to h_T via Equation (28), and the history corresponding to the plateau of the property evolution curve is taken. The plasticity channel is determined by isothermal low-cycle fatigue tests measuring the evolution of properties with accumulated plastic strain, converted to h_p via Equation (27), and similarly determined. If the material property does not reach a plateau within the test period, the accumulated history at the end of the test is taken as $h_{c,a,i}$.

The normalized history $u_{a,i}$ is the fraction of the accumulated history relative to the characteristic history, i.e., the evolution progress of that channel: $u_{a,i} = 0$ corresponds to the initial state before service, and $u_{a,i} = 1$ corresponds to the accumulated history reaching the characteristic value, at which point the property change reaches the saturation amplitude. The min operation in Equation (29) implies that after the accumulated history exceeds the characteristic value, the property change in that channel no longer grows. Different properties can have different characteristic histories under the same channel; for example, the thermal conductivity and elastic modulus require different histories to reach

their respective saturation amplitudes, so $u_{a,i}$ carries both the channel subscript a and the property subscript i. The property change caused by history channel a is written as

$$D_{a,i} = D_{a,i}^{max}[1 - (1 - u_{a,i})^{s_{a,i}}], \tag{30}$$

where $D_{a,i}$ is the property change caused by history channel a, i.e., the proportion by which the i-th property has changed relative to its initial value; $D_{a,i}^{max}$ is the saturation change magnitude, i.e., the maximum change proportion that the channel can cause, and is a given model parameter. From Equation (30), when $u_{a,i} = 0$, $D_{a,i} = 0$ and the property has not yet changed; when $u_{a,i} = 1$, $D_{a,i} = D_{a,i}^{max}$ and the change reaches the saturation amplitude. The shape parameter $s_{a,i}$ controls how the property change approaches the saturation amplitude: when $s_{a,i} = 1$, the property change grows linearly with evolution progress; when $s_{a,i} > 1$, the property change grows faster in the early stage and gradually slows down near the saturation amplitude; when $s_{a,i} < 1$, the property change grows more slowly in the early stage and accelerates near the saturation amplitude. The property retention factor under the joint action of the two types of history is

$$r_i = (1 - D_{p,i})^{n_{p,i}}(1 - D_{T,i})^{n_{T,i}}. \tag{31}$$

In Equation (31), $1 - D_{a,i}$ is the remaining property proportion after channel a acts alone, and the remaining proportions of the two channels are combined multiplicatively; the channel coupling exponent $n_{a,i}$ adjusts the relative weight of each channel: the larger $n_{a,i}$ is, the stronger the influence of that channel on the retention factor. Equations (29)–(31) give the specific computational form of the retention factor r_i in Equation (1); the r_i of each property appears in Sections 2.2.1 and 3 in the subscripted forms r_E, r_k, r_C, r_σ, and r_{sat}.

The parameters satisfy

$$h_{c,a,i} > 0,\ 0 \le D_{a,i}^{max} < 1, s_{a,i} > 0, n_{a,i} > 0. \tag{32}$$

Before the first mission, $h_p = h_T = 0$; from Equations (29)–(31), $r_i = 1$. As the history increases, r_i decreases monotonically; when the property changes in both channels reach the saturation amplitude, r_i reaches its lower bound:

$$r_i^{min} = (1 - D_{p,i}^{max})^{n_{p,i}}(1 - D_{T,i}^{max})^{n_{T,i}} > 0. \tag{33}$$

Different material properties adopt their own h_c, D^{max}, s, and n; therefore, the elastic modulus, thermal conductivity, and strength parameters are not required to vary by the same proportion. Equation (31) applies to the monotonic, bounded property change process assumed in this paper. If the material property does not decrease monotonically with the number of cycles—for example, if the property improves during service—the corresponding property evolution relation needs to be redesigned.

The thermophysical, elastic, and constitutive base parameters of the material are taken from the "China Aeronautical Materials Handbook" [38] (the c_p data for 20–227 °C are taken from [39]) and the calibration results of GH4169 thermo-mechanical fatigue tests [40]. Parameters between temperature points are taken by piecewise linear interpolation; the 20 °C values of the kinematic hardening, isotropic hardening, and rate-dependent parameters are taken as the 300 °C values; and the main constitutive parameters at 650 °C are given in Section 2.3.1. Two conversion conventions apply: the kinematic hardening parameters in [40] are given in terms of the back-stress saturation value C_j/γ_j, which differs from the convention of Equation (23), and the $C_{j0}(T)$ of this paper have been converted to 3/2 times the literature values with $\gamma_j(T)$ unchanged; $Y_{sat,0}$ is converted from the signed cyclic softening offset Q_∞ in [40] (−380 MPa at 650 °C) via $Y_{sat,0} = \sigma_{y0} + Q_\infty$, and $Y_{sat,0} < \sigma_{y0}$

corresponds to cyclic softening ($R_{sat} < 0$ in Equation (26)); the rate-dependent parameters are converted from the Norton law parameters. The property evolution parameters are assumed in this work and are listed in Table 1.

Table 1. Property evolution parameters (assumed in this work; channel coupling exponents $n_{p,i} = n_{T,i} = 1.0$).

Property	$h_{c,p,i}$	$D_{p,i}^{max}$	$s_{p,i}$	$h_{c,T,i}$	$D_{T,i}^{max}$	$s_{T,i}$
E	100	0.08	0.6	40	0.01	4.0
k	off	—	—	8.3	0.05	4.0
C	200	0.05	0.9	8.3	0.03	4.0
σ_y	150	0.10	0.9	8.3	0.05	4.0
Y_{sat}	150	0.15	0.9	8.3	0.04	4.0

The GH4169 alloy considered in this paper is a wrought nickel-based superalloy in the solution-treated and double-aged condition (AMS 5662/5663 type: solution treatment near 980 °C, followed by aging at about 720 °C and 620 °C), with a nominal composition of Ni-19Cr-18Fe-5Nb-3Mo-0.9Ti-0.5Al (wt.%) and a grain size of ASTM 8–10. This is the condition used for load-bearing superalloy thermal protection panels; the strengthening phases are the body-centered-tetragonal gamma-double-prime precipitates, with gamma-prime and grain-boundary delta phases as secondary constituents.

The material parameters used in this paper fall into four groups, each with a stated origin. The thermophysical and elastic constants are taken from the "China Aeronautical Materials Handbook" [38] for the same wrought, solution-treated-and-aged condition. The cyclic plastic parameters are converted from the GH4169 thermo-mechanical fatigue calibration of [40], again, for the wrought and aged condition. The thermal exposure integral is anchored to the Larson–Miller and thermal-strength-parameter relations of [38] and to the intermediate-temperature stress-relaxation activation energy of [41]. The property evolution parameters of Table 1 are not taken from any single source but are assumed, constrained only in order of magnitude by fatigue and creep anchors, as described below.

The first three groups therefore refer to a consistent initial condition, whereas the fourth is a modeling assumption rather than a measured property of a specific heat of the alloy; the consequences of this distinction are discussed in Sections 2.3 and 5.

Where the literature reports properties for other product forms, such as additively manufactured or long-term-service material, those data are not used as the basis of the initial state, although they inform the expected direction of the property change.

The remaining evolution constants are $p_{ref} = 2 \times 10^{-3}$, $Q = 260$ kJ/mol, $T_{ref} = 650$ °C, and $t_{ref} = 300$ s; the characteristic history relates to the program input coefficient by $A_{a,i} = 1/h_{c,a,i}$; the thermal exposure channel of E takes $h_{c,T,E} = 40$ (corresponding to $A_{T,E} = 0.025$), intentionally weakening the thermal channel of E so that the plasticity channel dominates. This choice is physically motivated rather than arbitrary: the elastic modulus of wrought GH4169 is governed mainly by the gamma-double-prime volume fraction [8] and is only weakly affected by thermal history alone, whereas it is reduced measurably once the alloy is cyclically deformed; the reported behavior of the alloy under long-term thermal exposure [9,10] supports a small thermal contribution to the modulus change relative to the plasticity contribution. Making the thermal channel of the elastic modulus deliberately weak therefore reflects this asymmetry; the influence of the assumption is nevertheless quantified directly, since the extended sensitivity analysis of Section 4.5 doubles the thermal channel contribution as one of its cases.

The order of magnitude of the evolution parameters is constrained by two types of anchors from fatigue and creep data. The plasticity channel is inferred from the Coffin–Manson/Morrow low-cycle fatigue relation [42–44]: under typical GH4169 thermo-mechanical fatigue conditions, the failure cycle count is $N_f \sim 10^2$–10^3 and the accumulated plastic strain increment per mission is $\Delta p \sim 10^{-3}$–10^{-2}; the total degradation must accumulate to a discernible magnitude within the service life, giving an order-of-magnitude constraint on the per-mission plasticity degradation rate of 10^{-3}–10^{-2}, corresponding to the $h_{c,p,i}$ and $D_{p,i}^{max}$ values in Table 1.

The thermal exposure channel is anchored by the Larson–Miller relation [27] and the GH4169 thermal-strength-parameter comprehensive equation given in the "China Aeronautical Materials Handbook" [38] ($C_{LM} = 25.125$; the rupture life at 650 °C is of order 10^2 h). With $t_{ref} = 300$ s (the peak dwell duration of a single mission), the high-temperature dwell of a single mission at T_{ref} corresponds to $\Delta h_T \sim 1$, the normalized upper bound; the hold-stage temperature in the present cases is below 650 °C, and the actual per-mission Δh_T is about 0.12, so that the thermal channel saturates at about 70 missions. Taking $h_{c,T,i} = 8.3$ makes the thermal-channel degradation exhibit a form that is significant in the early stage and saturates in the later stage within a structural life window of about 10^2 missions.

The activation energy of the thermal exposure integral, $Q = 260$ kJ/mol, is consistent with the intermediate-temperature stress relaxation activation energy of GH4169 [41]. This setting is a reasonable assumption for a controlled mechanism study; the robustness of the main conclusions to the evolution parameter values is examined by a parameter sweep with amplitudes of 0.5–2 times (Section 4.4).

2.3. Verification of Constitutive and Evolution Programs

This section examines the implementation of the non-isothermal cyclic viscoplasticity constitutive program and the material property evolution program of the relations established in Sections 2.1 and 2.2. The material property evolution parameters are assumed rather than calibrated, and are listed in Table 1; the object of verification in this section is the consistency between the program implementation and the assumed model relations, not the evolution parameters themselves. It is therefore a numerical verification and not a physical validation: it does not establish how accurately those relations reproduce the actual behavior of GH4169. The verification is organized in two layers: Section 2.3.1 examines the constitutive integration with property evolution turned off, demonstrating that the program correctly implements the constitutive relations of Section 2.2.1; Section 2.3.2 examines the property evolution module, demonstrating that the history accumulation, property mapping, and inter-mission update timing given by the program conform to the evolution behavior expected by the model relations of Sections 2.2.2 and 2.2.3. The two layers of verification together provide a reliable computational basis for the structural case studies in Sections 3 and 4.

2.3.1. Constitutive Relation Verification

In the constitutive verification, both material property evolution channels are turned off, so that the five property retention factors are constantly

$$r_i(x, N) = 1, i \in \{E, k, C, \sigma_y, Y_{sat}\}. \tag{34}$$

Under this condition, the constitutive program reduces to the non-isothermal Chaboche–Perzyna viscoplasticity constitutive model (Equations (11)–(26)). Its numerical implementation is examined through four layers of comparison: the first and second layers, respectively, adopt the combined-hardening and rate-dependent benchmark cases

from the Abaqus official Verification Guide [45], examining whether the implementations of the kinematic/isotropic hardening and the viscoplastic rate-dependent term are consistent with the official built-in model. The third layer adopts the GH4169 material parameters of this paper for an isothermal cyclic comparison, examining whether the cyclic response (dual back stress, cyclic softening) under actual parameters is consistent with the Abaqus built-in nonlinear combined-hardening model. The fourth layer applies a prescribed temperature–strain history for a non-isothermal comparison, examining whether the temperature-dependent parameter invocation and the non-isothermal integration are consistent with an independent material-point reference program. The benchmark comparisons apply surface pressure or boundary displacement according to the Abaqus benchmark cases; the isothermal and non-isothermal comparisons apply uniform mechanical strain through boundary displacement; all comparisons adopt a single C3D8 three-dimensional solid element (1 mm × 1 mm × 1 mm).

The first layer of verification adopts the Material 1 parameter set of the "Mises plasticity with combined isotropic/kinematic hardening" benchmark in §2.2.10 of the Abaqus Verification Guide (official input file mplcho3nt1); a uniaxial tensile surface pressure of 701 MPa is applied as specified in the benchmark case, and the user-defined material (UMAT) subroutine is compared with the Abaqus built-in combined-hardening model in the rate-independent limit ($\gamma_0 = 10^8\ \mathrm{s}^{-1}$). The stress–strain curves of the two models nearly coincide: the peak stresses are identical (both 701.000 MPa), and the maximum deviation over the whole process is $max|\Delta S_{11}| = 1.82$ MPa (relative difference 0.26%), indicating that the implementation of the kinematic and isotropic hardening is consistent with the official benchmark (Figure 2a).

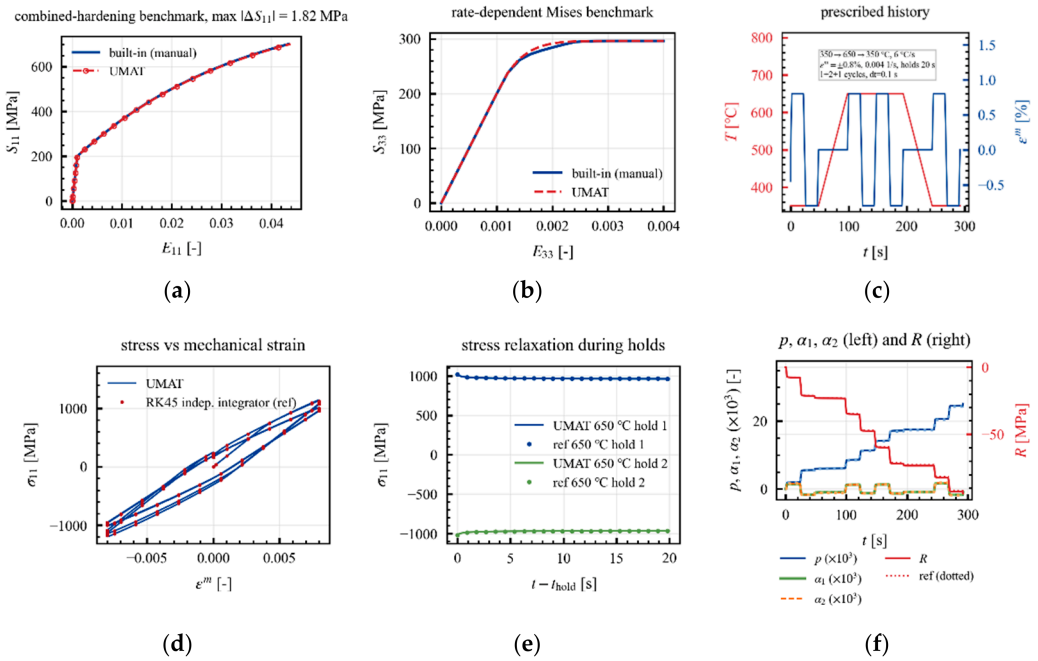


Figure 2. Constitutive program verification. (**a**) Stress–strain curve of the official combined-hardening benchmark comparison; (**b**) stress–strain curve of the official rate-dependent benchmark comparison; (**c**) non-isothermal temperature and mechanical strain history (parameters annotated in the figure); (**d**) stress–mechanical strain curve of the program value and the reference value; (**e**) stress relaxation during the hold segments; (**f**) evolution of p, α_1, α_2, and R.

The second layer of verification adopts the "Rate-dependent Mises plasticity" benchmark in §2.2.11 of the Abaqus Verification Guide (official input file mprooo3hut.inp); the tabulated hardening curve of the benchmark is fitted by the Voce form of Equation (25)

in this paper, a uniaxial tensile strain is applied (strain rate 0.2 s^{-1}), and the user-defined material (UMAT) subroutine is compared with the Abaqus built-in *RATE DEPENDENT model. The two models coincide completely in the plastic saturation stage, with identical terminal stresses of 296.246 MPa; in the early plastic stage, the maximum deviation is $max|\Delta S_{33}| = 8.20$ MPa (relative difference 2.77%), originating from the fitting difference between the Voce curve and the manually tabulated hardening representation, and the two models coincide after the plasticity is fully developed (Figure 2b). This comparison also verifies the reference-stress convention of the rate-dependent term: Equation (22) takes the current yield surface size $\sigma_y + R$ as the reference stress, consistent with the σ^0 convention of the built-in model, and in the softening stage ($R < 0$), the reference stress decreases with the yield surface contraction, which has a substantial influence on the rate-dependent response of cyclic-softening materials.

The third layer of verification adopts the GH4169 parameters of this paper for a 650 °C isothermal cyclic comparison: $\sigma_{y0} = 518$ MPa, $Y_{sat,0} = 138$ MPa ($Y_{sat,0} < \sigma_{y0}$, corresponding to cyclic softening), $b = 13.20$, dual back stress $C_1 = 207{,}158$ MPa, $\gamma_1 = 345$, $C_2 = 150{,}675$ MPa, and $\gamma_2 = 305$. Four symmetric total-strain cycles are applied (strain amplitude ±0.8%, tensile and compressive peaks each held for 20 s), and the user-defined material (UMAT) subroutine is compared with the Abaqus built-in nonlinear combined-hardening model in the rate-independent limit ($\gamma_0 = 10^8$ s^{-1}). The kinematic hardening evolution equation of the Abaqus built-in model has the same form as that of the user program, and under the von Mises equivalence, the effective back stresses of both sides are $\sum_j (C_j/\gamma_j)(1 - e^{-\gamma_j p})$. The kinematic hardening parameters are therefore input with the same numerical values; the 3/2 conversion between the convention of [40] and that of Equation (23) has already been performed once in the material parameter preparation. The isotropic hardening is input in the built-in model as the offset $Q_\infty = Y_{sat,0} - \sigma_{y0} = -380$ MPa, and the rate-dependent term takes near-rate-independent parameters, so that the comparison is not affected by the reference-stress convention. The results are listed in Table 2 (isothermal comparison column).

Table 2. Constitutive program verification results and acceptance.

Comparison Quantity	Isothermal Comparison (Reference: Abaqus Built-In Model)			Non-Isothermal Comparison (Reference: Independent Integration Program)		
	Program	**Reference**	**Rel. Diff. (Threshold)**	**Program**	**Reference**	**Rel. Diff. (Threshold)**
Tensile peak stress (MPa)	945.2	945.5	0.03% (≤0.5%)	1138.4	1136.4	0.17% (≤2.0%)
Compressive peak stress (MPa)	−982.1	−982.4	0.03% (≤0.5%)	−1192.3	−1190.7	0.14% (≤2.0%)
End-of-hold stress (MPa)	936.0/−938.7	936.4/−939.2	≤0.05% (≤0.5%)	1070.0/−1085.5	1073.2/−1089.9	≤0.40% (≤2.0%)
End-of-cycle p	0.022769	0.022727	0.19% (≤1.0%)	0.025131	0.024858	1.10% (≤2.0%)
End-of-cycle R (MPa)	−98.65	−98.49	0.16% (≤0.5%)	−94.14	−93.28	0.92% (≤2.0%)
Stress-history error e_σ (Equation (39))	4.26×10^{-4}	—	$\leq 1 \times 10^{-3}$	3.42×10^{-3}	—	$\leq 5 \times 10^{-3}$

The fourth layer comparison applies a prescribed temperature–strain history: one mechanical strain cycle is applied at an initial 350 °C (0–48 s); the temperature is raised to 650 °C at 6 °C/s (48–98 s). Two cycles are applied at 650 °C (98–194 s); the temperature

is then lowered to 350 °C at 6 °C/s (194–244 s); finally, one cycle is applied at 350 °C (244–292 s). Each mechanical strain cycle is 0 → +0.8% (strain rate 0.004 s^{-1}, 2 s) → tensile peak held for 20 s → +0.8% → −0.8% (4 s) → compressive peak held for 20 s → back to 0 (2 s), totaling 48 s; the history parameters are annotated in Figure 2c. Each stage of the history corresponds to a class of behaviors to be checked: the forward and reverse loading of the first 350 °C cycle checks the initial yield, reverse plasticity, and kinematic hardening; the two 650 °C cycles check the cycle-by-cycle evolution of the isotropic hardening. The tensile and compressive peak-hold segments check the viscoplastic relaxation; the heating and cooling segments check the invocation of temperature-dependent parameters; the last 350 °C cycle has the same strain path as the first cycle, used to compare the consistency of the temperature-parameter return path. The stress–mechanical strain curve, the stress relaxation during the hold segments, and the evolution of the internal variables computed by the two programs are shown in Figure 2d, Figure 2e, and Figure 2f, respectively.

The program computes the thermal strain using the secant coefficient of thermal expansion:

$$\varepsilon^{th}(T) = \alpha_{sec}(T)\left(T - T_{sf}\right) I, \tag{35}$$

Equation (35) is equivalent to Equation (12): the secant coefficient of thermal expansion is the ratio of the integral term in Equation (12) to the temperature difference $T - T_{sf}$. In the numerical implementation, the secant coefficient of thermal expansion is taken by piecewise linear interpolation with temperature; the a_T given in [38] is the mean coefficient of linear expansion from 20 °C to the corresponding temperature (secant value). If the literature gives the instantaneous (tangent) coefficient of linear expansion, it must be converted to the secant value using its mean from the stress-free temperature before use, so as to avoid a systematic bias in the thermal strain at high temperature. The corresponding mechanical strain is

$$\varepsilon^{m}(t) \ = \varepsilon(t) - \varepsilon^{th}[T(t)]. \tag{36}$$

The reference solution is given by an independent material-point integration program: it reads the same temperature, total strain, and time sequences as the finite element case, but does not call the user-defined material (UMAT) subroutine and does not share its state-update code; the integration adopts an adaptive fourth-order Runge–Kutta method (relative tolerance 10^{-8}, absolute tolerance 10^{-10}). The comparison quantities include the stress, accumulated equivalent viscoplastic strain, two kinematic hardening internal variables, and the isotropic hardening variable:

$$\sigma(t), p(t), \alpha_1(t), \alpha_2(t), R(t). \tag{37}$$

The program saves the kinematic hardening internal variable α_j; the back stress is not saved as an independent state, but is derived from the current kinematic hardening modulus:

$$X_j = \frac{2}{3} C_j \alpha_j. \tag{38}$$

Therefore, the internal-variable verification focuses on α_j; the X_j obtained from Equation (38) is compared as a diagnostic output. The normalized root-mean-square error of the stress history is defined as

$$e_\sigma = \sqrt{\frac{\sum_l \left[\sigma_{num}(t_l) - \sigma_{ref}(t_l)\right]^2}{\sum_l \sigma_{ref}^2(t_l)}}. \tag{39}$$

The acceptance thresholds are specified before the computation and are listed together with the results in Table 2. The time-discretization convergence check adopts four levels of maximum time increment—Δt, $\Delta t/2$, $\Delta t/4$, $\Delta t/8$ (baseline $\Delta t = 0.1$ s)—while keeping the history and its physical duration unchanged.

In the table, the end-of-hold stress is listed as "end of tensile hold/end of compressive hold"; the deviations of the end-of-cycle kinematic hardening internal variables α_1 and α_2 do not exceed 1.3% and are not listed. The reference values of stress and p in the isothermal comparison are taken from the Abaqus built-in model (maximum time increment 0.0125 s); the reference values of α_1, α_2, and R are taken from the independent integration program (same constitutive relation, rate-independent limit $\gamma_0 = 10^8$ s^{-1}). The non-isothermal comparison is under the Perzyna rate-dependent condition, with backward-Euler implicit integration on the program side and adaptive RK45 explicit integration on the reference side; the difference between the two arises from the use of different integration schemes and converges at first order as the step size is refined (e_σ decreases from 3.42×10^{-3} at the baseline step to 4.35×10^{-4} after successive refinement). All comparison quantities meet the acceptance thresholds specified before the computation.

2.3.2. Material Property Evolution Program Verification

Section 2.3.1 has independently verified the constitutive implementation; on this basis, this section examines whether the implementation of the entire evolution chain—"history accumulation → property change → retention factor → inter-mission update"—conforms to the behavior expected by the model of Sections 2.2.2 and 2.2.3.

Following the parameter assumption approach of Section 2.2, the driving end of this chain is determined by the environment and loading, and the response-end material properties varying with mission count can be measured experimentally. According to the design of the material evolution model, the driving-end thermal exposure history h_T is determined by integrating the temperature history via Equation (28) and grows approximately linearly with mission count; the plasticity history h_p is accumulated by the constitutive integration via Equation (27).

If there were no material property degradation, h_p would also grow linearly with mission count, but since material property degradation causes the yield surface to contract, the per-mission plasticity increment is amplified accordingly, so h_p grows slowly at first and then faster with mission count (Figure 3a). The response-end retention factors of each property decrease with mission count in a pattern that can be directly measured by repeated thermo-mechanical coupling experiments.

Since such experiments are complex and costly and not yet available for this work, the decrease pattern is assumed rather than measured, and follows the direction of the trends reported for GH4169 in the literature (the order-of-magnitude constraint is given in Section 2.2.3). The intermediate mapping (Equations (29)–(31)) maps the known driving-end curve to the expected response-end curve; its parameterized form and parameter values are designed so that the driving end and the response end are self-consistent.

In addition, the update timing convention is that the retention factor used in mission N is determined by the history at the end of the previous mission (lagged activation):

$$r_i^{(N)} = f_i\left(h_a^{(N-1)}\right), r_i^{(1)} = 1, \tag{40}$$

where $h_a^{(N)}$ is the channel history accumulated at the end of mission N (Equations (27) and (28)), and f_i is the evolution mapping of Equations (29)–(31); the property value within the current mission remains unchanged during the mission, and at the end of the mission, the property value for the next mission is computed from the updated accumulated history; the

constitutive state (ε^p, p, α_j, R) is transferred continuously across missions (Equation (10)). The implementation of the evolution program should reproduce the above expectations item by item: history accumulation is executed according to Equations (27) and (28); mapping is evaluated pointwise according to Equations (29)–(31); update takes effect according to the timing of Equation (40); and the material property decreases monotonically and boundedly with the accumulated history, with the degradation amplitude ordered by mechanism sensitivity.

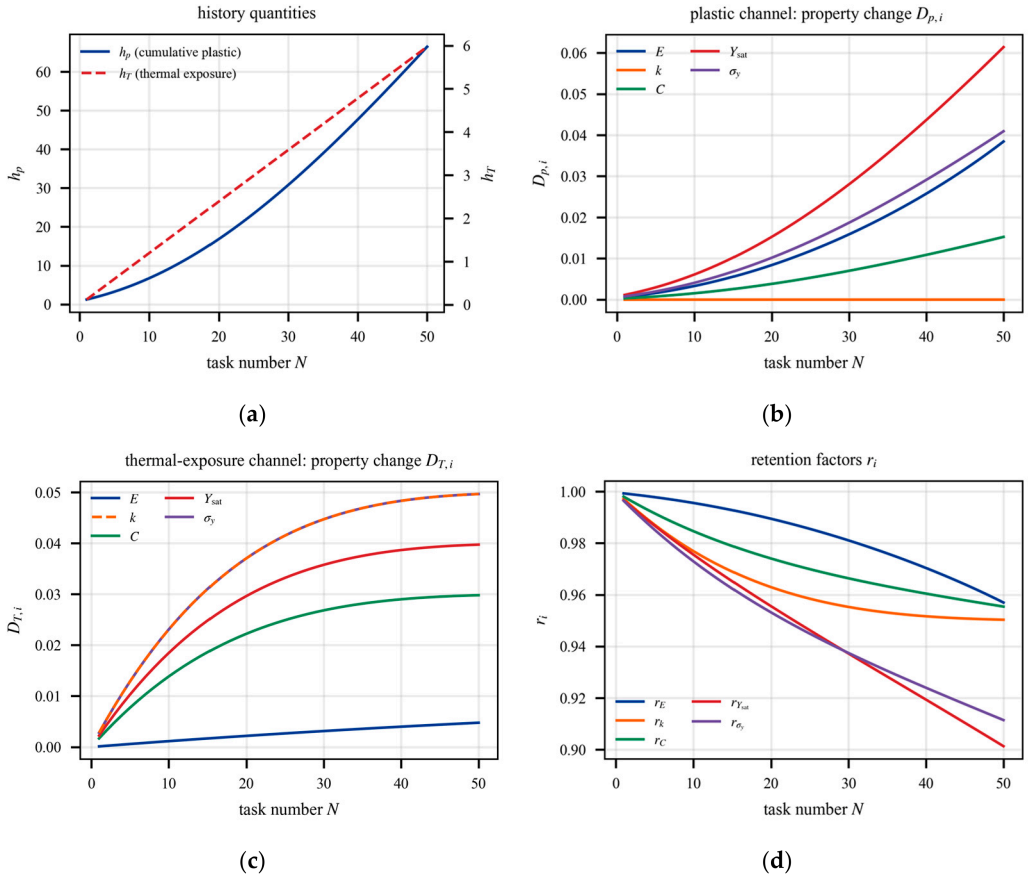


Figure 3. Verification of the material property evolution chain for structural Case C (top layer, hot face $z = 4.5$ mm, 50 missions). (**a**) Variation in the history quantities h_p, h_T with mission count; (**b**) plasticity-channel property change $D_{p,i}$; (**c**) thermal-exposure-channel property change $D_{T,i}$ (the k and σ_y curves coincide); (**d**) evolution of the five retention factors r_i with mission count.

A 50-mission chain is executed on the same local plate case as the main Case C (50 mm × 50 mm × 5 mm, hot-face aerodynamic heating and aerodynamic pressure, side elastic foundation $\eta = 4$; the setup is given in Section 3) to examine the behavior of the evolution module under a realistic service history. The evolution parameters take the final assumed values in Table 1 (five properties × two channels). For fast iteration, the in-plane mesh is 6 × 6 with 5 layers through the thickness (180 C3D8 elements). This fast model is consistent with the main-case converged mesh (14 × 14 × 5) in temperature field and plasticity history (h_p difference $\leq 0.1\%$, S_{11} difference ≤ 0.4 MPa). Under the final parameters, a 50-mission chain review confirms that the top-layer retention factor trajectories of the two nearly coincide (e.g., r_E at mission 50 is 0.9556 vs. 0.9557). The evolution response is insensitive to in-plane mesh refinement, and the evolution behavior verified in this section is representative of the main case.

In the early missions, the thermal channel dominates (σ_y degrades deeper than Y_{sat}); as h_p increases, the contribution of the plasticity channel rises, and Y_{sat} overtakes σ_y in the later stage.

The curves in Figure 3b–d are also analytically recomputed using Equations (30) and (31), and are pointwise consistent with the program state-variable output.

The parameter update at the mission boundary is verified separately on a single material element. Because the program commits the pending retention factors to the active state at the first increment of each mission step, the state immediately before the update corresponds to frame 0 and the state immediately after the update to frame 1 of that step.

Three closed-form checks are carried out. First, the effective elastic modulus back-solved from the elastic strain and stress agrees with the value declared by the program to within 0.002%. Second, the back-stress jump across the boundary is quantified: since the back stress is the product of the kinematic hardening modulus and the transferred internal variable, and the modulus is scaled by its retention factor while the internal variable is transferred continuously, a jump is an inherent consequence of the formulation rather than an arbitrary modeling choice.

The evolution parameters of this single-element case are not those of Table 1: the kinematic hardening retention factor is driven far deeper, falling to 0.5752 at saturation (a total degradation of 42.5%) against 0.9215 (7.85%) for the structural cases, so that the boundary update is exercised well beyond the degradation range of the structural computations. The measured jump magnitude reaches 17.7% at the start of the third mission and agrees with the predicted ratio to within 0.14%; it decreases as the degradation saturates and falls to 0.001% once the retention factor of the kinematic hardening modulus stabilizes, so that the jump is confined to the first few missions of the service life.

Third, the release of stored energy associated with the modulus reduction is reproduced by its closed-form decomposition with a relative deviation of 0.000%. In addition to the above comparisons, the constitutive program has also been tested in other aspects, including pure elasticity, free and constrained thermal expansion, initial yield, pure shear yield, and the consistency verification of the algorithmic tangent.

The above results indicate that, under the given evolution parameters, the program correctly implements the established constitutive relations and property evolution relations, and can provide a reliable material model basis for the subsequent structural response analysis.

3. Numerical Model and Computational Method

3.1. Problem Description and Model Abstraction

This paper extracts a local plate from the large-area region of the thermal protection structure of a high-speed vehicle as the object of study, serving as the structural application case of the material evolution model of Section 2. The local model retains the outer-surface aerodynamic heating, aerodynamic pressure, through-thickness heat transfer, and surrounding-structure constraints, and is used to analyze the material property field formed by the local service history and its influence on the subsequent structural response.

To examine the structural effects of spatially non-uniform evolution of material properties, three plate structures—a thin plate, a perforated plate, and a thick plate—are set up (Figure 4), with a single variable difference maintained among the structures to isolate the effect of structural features: the thin plate (length $L = 50$ mm, width $W = 50$ mm, thickness $B = 5$ mm) is the baseline structure, corresponding to an independent thermal protection panel. The perforated plate has a through-hole of diameter $d = 10$ mm at the in-plane center of the thin plate, corresponding to a panel with connection holes/piping openings; the thick plate has a thickness of $B = 20$ mm (four times that of the thin plate), corresponding to an integrated load-bearing thermal protection panel. The three structures differ only in geometry; the mission profile, thermal boundary conditions, and mechanical constraints are completely identical (Section 3.3), and the material parameters and comparison schemes are the same (Section 3.4).

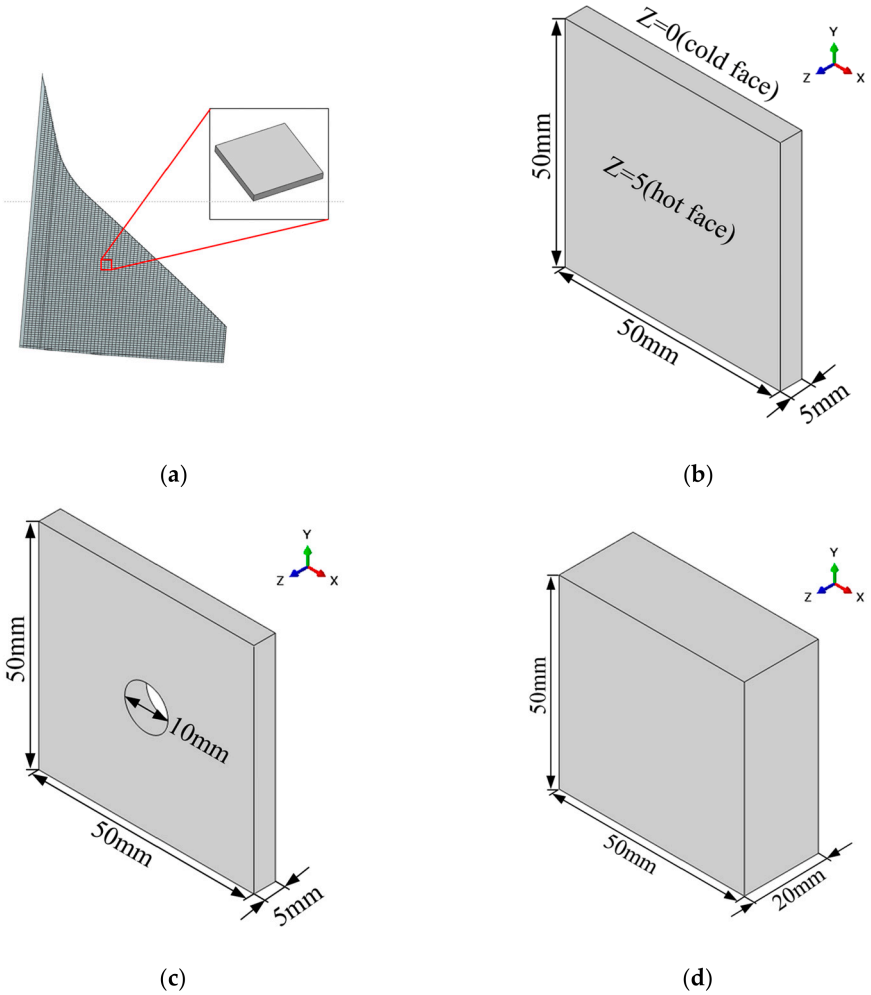


Figure 4. Extraction location of the local plate model in the large-area thermal protection structure, and the three plate structure models and coordinate system. (**a**) Extraction location schematic; (**b**) thin plate 50 × 50 × 5 mm; (**c**) perforated plate 50 × 50 × 5 mm + central hole $d = 10$ mm; (**d**) thick plate 50 × 50 × 20 mm. The hot face, cold face, and thickness coordinate z are annotated in the figure.

The outer surface is subjected to aerodynamic heating and aerodynamic pressure, and the inner surface is adjacent to the thermal environment of the vehicle's internal structure. This paper takes the thickness coordinate z as pointing from the inner surface to the outer surface ($z = 0$ is the inner surface, $z = B$ is the outer surface), and refers to the outer surface subjected to aerodynamic heating as the hot face and the inner surface adjacent to the internal thermal environment as the cold face.

3.2. Governing Equations and Thermo-Mechanical Coupling Procedure

The temperature field and mechanical response of the local thermal protection plate are solved by a sequential thermo-mechanical coupling method. The transient temperature field under aerodynamic heating is first computed; the complete temperature history is then transferred to the mechanical model, and the aerodynamic pressure load with the same time period is applied. The inter-mission update of material properties, the accumulation of history variables, and the transfer of constitutive state are all executed according to the method described in Section 2.

The temperature field within mission N satisfies the transient heat conduction equation:

$$\rho c_p \dot{T} = \nabla \cdot (k \nabla T), k = k_0(T) r_k. \tag{41}$$

where ρ is the density, c_p is the specific heat capacity, $k_0(T)$ is the temperature-dependent thermal conductivity in the initial state, and r_k is the thermal conductivity retention factor used in mission N. The current model does not consider volumetric heat sources or plastic-deformation heat generation.

After neglecting inertial and body forces, the quasi-static mechanical equilibrium equation of the plate is

$$\nabla \cdot \sigma = 0, \tag{42}$$

where σ is the stress tensor, determined by the non-isothermal cyclic viscoplasticity constitutive relation established in Section 2. The transient temperature field enters the mechanical analysis through the thermal strain and temperature-dependent material parameters, and the aerodynamic pressure is applied as a normal load on the outer surface.

3.3. Mission Profile, Initial Conditions, and Boundary Conditions

During flight, a high-speed vehicle typically experiences aerodynamic heating and aerodynamic forces through ascent, high-level hold, and descent phases. To characterize this main temporal feature and simplify the mission profile, this paper uses a trapezoidal function to describe the aerodynamic heating and aerodynamic force loads. Let $g(t)$ be the normalized trapezoidal function shown in Figure 5; the aerodynamic heat flux and aerodynamic pressure are, respectively,

$$q_a(t) = q_m g(t), p_a(t) = p_m g(t), \tag{43}$$

where q_m and p_m are, respectively, the peak aerodynamic heat flux and peak aerodynamic pressure, taken as $q_m = 145$ kW/m^2 and $p_m = 0.1$ MPa. These values follow from the one-dimensional steady-state thermal balance of the mission segment, $\varepsilon\sigma_s(T_s^4 - T_0^4) + h_b(T_s - T_b) \approx q_m$. The equilibrium hot-face temperature corresponding to this heat flux is about 620 °C, within the temperature upper limit of 650 °C for the material parameters in Table 1. The bending stress of the plate produced by the 0.1 MPa aerodynamic pressure is only a few MPa, negligible relative to the thermal stress, and the pressure is retained only for load integrity. The trapezoidal mission sequentially includes loading (110 s), peak hold (300 s), unloading (110 s), and a post-mission cooling stage.

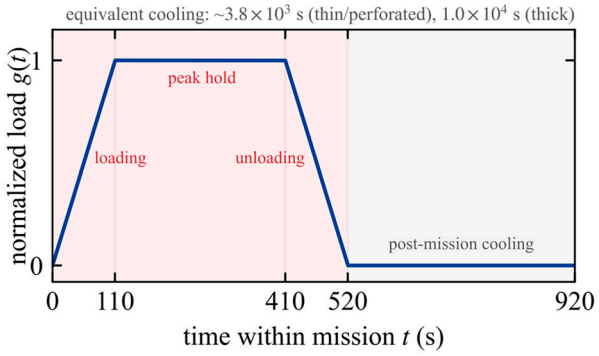


Figure 5. Normalized trapezoidal mission profile and thermo-mechanical coupling sequence. The vertical bands mark the successive stages of a mission: the light red bands are the heating, hold, and unloading stages, and the light grey band is the post-mission cooling stage.

The post-mission cooling stage is unloaded cooling: considering that the interval between adjacent flight missions is usually much larger than the time required for structural cooling, this paper does not simulate the complete inter-mission parking process. Instead, an equivalent cooling time is first determined through a single-mission pre-computation (cooling until the structural temperature essentially recovers to the ambient temperature

and the plastic strain increment is negligible; about 3.8×10^3 s for the thin plate and perforated plate, and 1.0×10^4 s for the thick plate). In the formal computation, after the aerodynamic heating and aerodynamic pressure are unloaded, unloaded cooling continues for this duration; the remaining ambient-temperature parking time is then omitted, and the end-of-mission temperature field, constitutive state variables, and material property parameters are continuously transferred to the next mission.

The thermal boundary conditions are given separately for the load–hold–unload stage and the post-mission cooling stage. The load–hold–unload stage (FLIGHT) is

$$\begin{aligned} k\nabla T\cdot n &= q_a, \text{ heated outer surface,} \\ -k\nabla T\cdot n &= h_b(T - T_b), \text{ inner surface,} \\ -k\nabla T\cdot n &= \varepsilon\sigma_s\left(T^4 - T_0^4\right), \text{ outer-surface radiative dissipation,} \\ \nabla T\cdot n &= 0, \text{ side surfaces} \end{aligned} \tag{44}$$

The post-mission cooling stage (PARK) is

$$\begin{aligned} k\nabla T\cdot n &= 0, \text{ heated outer surface (aerodynamic heat flux removed),} \\ -k\nabla T\cdot n &= h_{out}(T - T_0) + \varepsilon\sigma_s\left(T^4 - T_0^4\right), \text{ outer-surface natural convection and radiation,} \\ -k\nabla T\cdot n &= h_b(T - T_b), \text{ inner-surface weak convective heat transfer,} \\ \nabla T\cdot n &= 0, \text{ side surfaces} \end{aligned} \tag{45}$$

where n is the outward boundary normal; h_b is the equivalent convective heat transfer coefficient of the inner surface during the mission stage, taken as $h_b = 200$ W/(m^2·K). This value is the equivalent order of magnitude for the back of a large-area metallic thermal structure conducting heat through heat pipes or frame/stringer structures: natural convection of about 10 W/(m^2·K) corresponds to a closed internal bay without heat pipes, whereas forced convection of about 10^3 W/(m^2·K) corresponds to an actively cooled structure. This paper takes an intermediate order of magnitude for the passive large-area plate; $T_b = 20$ °C is the internal ambient temperature; $h_{out} = 20$ W/(m^2·K) is the weak natural convective heat transfer coefficient of the outer surface during the cooling stage; $\varepsilon = 0.8$ is the surface emissivity; σ_s is the Stefan–Boltzmann constant; $T_0 = 20$ °C is the ambient temperature.

Aerodynamic radiative heating (shock-layer gas radiation) is negligible relative to aerodynamic convective heating at the cruise-type mission magnitude of this paper and is not included. The self-radiative dissipation term of the heated surface accounts for about 20% of the heat flux at the hot face during the hold stage (at a hot-face temperature of 619 °C, $\varepsilon\sigma(T^4 - {T_0}^4) \approx 28$ kW/m^2 against a heat flux of 145 kW/m^2), but is retained throughout to share the same radiation model with the cooling stage and to ensure the completeness of the thermal balance.

Here, $q_a > 0$ is defined as heat entering the plate, and $p_a > 0$ as pressure pointing toward the interior of the plate. During the cooling stage, the inner surface reverts to weak convective heat transfer $h_b = 20$ W/(m^2·K) (the order of magnitude of natural convection in the internal environment after heat-pipe-type devices are turned off or weakened).

The initial temperature of the first mission is 20 °C, consistent with the internal ambient temperature; the initial temperature field of subsequent missions is continuously transferred from the previous mission.

The plate model established in this paper geometrically represents a local region extracted from the large-area thermal protection structure, but the model does not reconstruct the real load-bearing structure around the wing or fuselage. Considering that this paper aims to reveal the relative influence of material property evolution on the structural response under a fixed thermo-mechanical mission profile, the computational domain is defined as a representative plate with fixed dimensions and idealized boundary conditions.

The three structures share the same set of mechanical constraints (Figure 6 details the thin plate; the perforated plate and thick plate adopt the same set): the elastic foundation stiffness is defined by the in-plane characteristic dimension and is independent of the plate thickness; the thick plate therefore shares the same stiffness value as the thin plate, ensuring a "thickness-only" single-variable comparison.

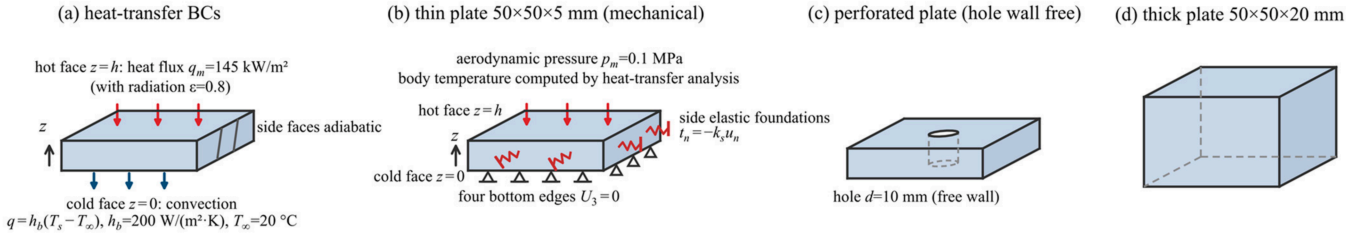


Figure 6. Boundary conditions of the plate model. Red arrows denote the hot-face heat flux and the aerodynamic pressure, blue arrows denote the cold-face convection, the spring symbol denotes the normal elastic foundation on the four side surfaces, and the triangular symbols denote the through-thickness displacement constraint U3 = 0. (**a**) Thermal boundary conditions: hot-face heat flux q_m= 145 kW/m^2 with radiation (ε = 0.8), cold-face convection h_b = 200 W/(m^2·K) at T_∞ = 20 °C, and adiabatic side faces; (**b**) mechanical constraints of the thin plate: aerodynamic pressure pm = 0.1 MPa on the hot face, through-thickness displacement constraints U_3 = 0 on the four edges of the lower surface (cold face), and normal elastic foundations $t_n = -k_s u_n$ on the four side surfaces; (**c**) perforated plate (hole wall free); (**d**) thick plate, both adopting the same set of mechanical constraints.

The mechanical constraints are set in two parts (Figure 6). First, the through-thickness displacement is constrained on the four edges of the lower surface of the plate to support the plate and balance the normal load; the in-plane displacement of the four edges remains free. Second, the local plate is taken from a larger load-bearing structure, and its in-plane thermal expansion is partially constrained by the surrounding structure; this paper equates the action of the surrounding structure on the in-plane expansion to a finite-stiffness elastic foundation in the side-surface normal direction, i.e., on the four side surfaces,

$$t_n = -k_s u_n, k_s = \eta \frac{E_{ref}}{L}, \tag{46}$$

where t_n is the side-surface normal distributed reaction, u_n is the side-surface normal displacement, k_s is the elastic foundation stiffness per unit area, η is the dimensionless constraint coefficient, E_{ref} is the elastic modulus of the initial material at the reference temperature, and $L = 50$ mm is the in-plane characteristic dimension of the plate. This paper takes $\eta = 4$ (corresponding to $k_s \approx 1.6 \times 10^4$ N/mm^3), placing the in-plane constraint between fully free and fully rigid; this value is determined by trial computation. Under the thermal load matching the mission of this paper, the peak thermal stress in the plate corresponding to $\eta = 4$ is about 1.1×10^3 MPa, between the near-zero stress of free expansion and the 1.8×10^3 MPa of rigid constraint, producing a moderate elastoplastic response; the tangential displacement of the side surfaces remains free, without introducing additional shear constraints. The normal elastic foundations of the four side surfaces and the edge constraints of the lower surface together eliminate all rigid-body motion modes of the model, so no additional point constraints are applied; all mission cycles adopt the same mechanical constraint conditions.

3.4. Computational Schemes and Result Extraction

To examine the influence of the mission-to-mission feedback of material property evolution and its spatial treatment on the computational results, three comparison schemes are set up. The three schemes adopt the same geometric model, mission profile, initial

material parameters, boundary conditions, and finite element discretization, and differ only in the material property update method.

In Case A, all property retention factors remain constant at 1; material property evolution is not fed back to subsequent missions, and its structural response is equivalent to the no-feedback update treatment; the plastic strain, accumulated plastic strain, kinematic hardening internal variables, and isotropic hardening variable are still transferred continuously between missions. In addition, in Case A, the property evolution estimate is computed in a diagnostic manner according to the local history increment at each integration point; this diagnostic quantity does not enter subsequent missions and is used only for comparison with the actual evolution path of Case C.

In Case B, a spatially uniform value is obtained from the local history increment computed in the current mission, and the spatially uniform material property used in the next mission is updated accordingly; its field-reduction rule differs by structure. The thin plate takes the volume average (the degradation spatial distribution is mild, and the average is representative), and the perforated plate takes the field maximum (the volume average in a structure with concentrated degradation would pull down the history at the deepest-degradation position to the average level, systematically underestimating the local degradation and biasing toward the non-conservative side; the field maximum approximates the deepest-degradation position in a conservative manner).

Case B is not computed for the thick plate (according to pre-computation, the thick plate barely evolves). In Case C, the local history of each integration point is retained, and the local material property used in the next mission is updated separately.

The computational results of Case A and Case C are used to evaluate the influence of ignoring the mission-to-mission feedback on the structural response; the comparison between the diagnostic evolution path of Case A and the actual evolution path of Case C is used to evaluate the influence of feedback on the property evolution prediction itself. The computational results of Case B and Case C are used to evaluate the prediction deviation of the spatially uniform update relative to the local update. Since the two update methods form different temperature, stress, and plasticity histories in subsequent missions, the difference between Case B and Case C represents the overall deviation formed by the entire inter-mission evolution process.

All three structures adopt a sequential thermo-mechanical coupling chain computation: each mission first performs thermal analysis (reading the end-of-previous-mission property field) and then mechanical analysis (restart continuation, reading the thermal-analysis temperature field), for a total of 50 missions. One mission is one thermo-mechanical loading cycle, so the 50 missions are 50 cycles computed in sequence. The thermal-analysis field output interval is 20 s (mission segment) and 50 s (parking segment for the thin plate and perforated plate) or 100 s (thick plate); the mechanical-analysis field output interval is 50 s; the restart file retains only the end-of-step state.

The computational results are extracted according to the local service history, material properties, thermal response, and mechanical response. Variables distributed along the through-thickness direction are represented by the in-plane average at the corresponding thickness position, to reduce the influence of local numerical fluctuations on the overall variation pattern. The local service history includes the thermal exposure accumulation and the per-mission plasticity history increment. The material property results include the variation in each property retention factor with mission count and its through-thickness distribution. The thermal response mainly extracts the through-thickness temperature, the cold-face average temperature, the cold-face heat flux, and the heat transfer per mission. The mechanical response mainly extracts the in-plane compressive stress, the maximum compressive stress and its thickness position, the per-mission accumulated plastic strain

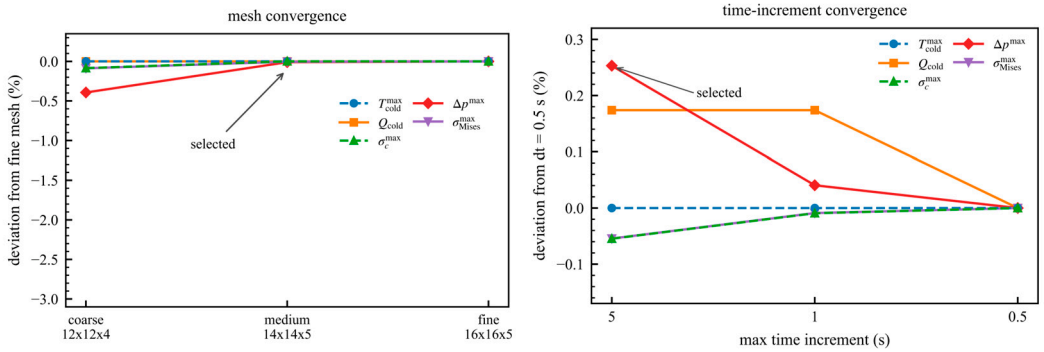
increment, and the extent of the plastically affected zone. The extracted quantities are consistent across the three structures, with two additional structure-related statistics: for the perforated plate, the results are grouped by hole-edge ($r < 8$ mm) and far-field ($r > 30$ mm); for the thick plate, through-thickness profiles are extracted in 8 layers and the peak-position trajectory is tracked.

Under the biaxial in-plane stress state, the compressive stress is characterized by the smaller in-plane principal stress. The peak compressive stress is taken as the maximum over all thickness positions and computation instants within a single mission, and the corresponding thickness position and occurrence time are recorded. If a fixed mission stage is analyzed, all three schemes adopt the same extraction instant. The comparison between Case B and Case C uses the absolute difference and relative difference in the response quantities. Temperature, heat transfer, peak compressive stress, and plastic response are normalized separately; response quantities of different dimensions are not directly compared. The peak-position difference is normalized by the plate thickness.

3.5. Finite Element Discretization and Convergence Verification

The thermal analysis and mechanical analysis respectively adopt DC3D8 eight-node linear heat transfer elements and C3D8 eight-node three-dimensional solid elements; the two types of models adopt the same geometry and node arrangement to reduce the numerical error introduced by temperature field transfer. The mesh size is determined by convergence verification.

Three sets of meshes—coarse, medium, and fine (12 × 12 × 4, 14 × 14 × 5, 16 × 16 × 5)—are used, keeping the material parameters, boundary conditions, mission profile, and time increment identical, and the cold-face maximum temperature, heat transfer per mission, maximum compressive stress, compressive-stress peak position, and maximum per-mission plastic strain increment are compared using the results of mission 1 of Case C (Figure 7a).



(**a**) (**b**)

Figure 7. Mesh and time-increment convergence verification. (**a**) Deviation of each evaluation quantity relative to the fine-mesh value (16 × 16 × 5) under three sets of meshes; (**b**) deviation of each evaluation quantity relative to the maximum time-increment 0.5 s value. In (**a**), the T_{cold}^{max} and Q_{cold} curves nearly coincide, as do the σ_c^{max} and σ_{Mises}^{max} curves; in (**b**), the σ_c^{max} and σ_{Mises}^{max} curves nearly coincide.

When the mesh is refined from coarse to medium, the compressive-stress peak position shifts from z = 4.375 mm to z = 4.5 mm (a one-element-layer jump, a relative change of 2.9%, exceeding the 1% criterion), the maximum per-mission plastic strain increment changes by 0.4%, and the other evaluation quantities do not exceed 0.1%. When refined from medium to fine, the maximum relative change in all evaluation quantities does not exceed 0.01%, and the compressive-stress peak position is located in the same element layer. Considering both

computational accuracy and cost, the medium mesh (14 × 14 in-plane, 5 layers through the thickness) is adopted for the subsequent analysis.

The influence of the time increment is likewise determined by comparing three sets of maximum time increments (Figure 7b): between the maximum time increment of 5 s and 0.5 s, the maximum difference is 0.3% (maximum per-mission plastic strain increment), and the stress and heat transfer per mission do not exceed 0.2%.

The final meshes of the three structures are shown in Figure 8. The thin plate adopts the aforementioned medium mesh (14 × 14 × 5). The perforated plate maintains a similar overall resolution and adopts an 8-block fan-shaped partition to achieve a structured mesh, with 40 circumferential divisions (9° each), 10 radial divisions, and 5 layers through the thickness. The thick plate retains 14 × 14 in-plane and 8 layers through the thickness (2.5 mm per layer). In terms of computational cost, one 50-mission chain (100 jobs of thermal and mechanical analyses) takes about 12–15 h on a common workstation, and all the computations for the three structures and three treatments are completed within one week.

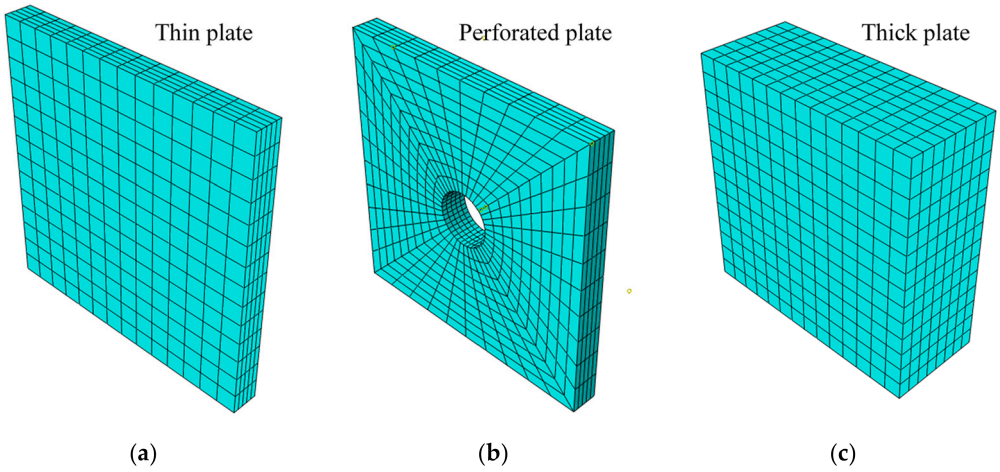


Figure 8. Finite element meshes of the three structures. (**a**) Thin plate; (**b**) perforated plate (8-block fan-shaped partition); (**c**) thick plate.

4. Results and Discussion

4.1. Material Evolution Behavior of the Three Structures

This section holds the structure fixed and sequentially presents the evolution of the local service history and material property field of the thin plate, perforated plate, and thick plate with mission count. The service history (plasticity history h_p and thermal exposure history h_T) is the driving end of property evolution; its distribution form and accumulated amount directly determine the distribution and degradation amplitude of the property field; the property field is formed by pointwise mapping of the local history through Equations (29)–(31).

4.1.1. Service History Field of the Thin Plate

The thermal exposure history of the thin plate is first analyzed. Figure 9a,b show the evolution of the Case C thermal exposure history field with mission count. In mission 1, the three treatments—Case A, B, and C—adopt the same initial thermophysical properties, and the thermal exposure increment of the three treatments within this mission is completely identical. By the end of mission 50, the Case C thermal exposure accumulation at the hot face, mid-thickness, and cold face respectively increases from 0.119, 0.077, and 0.049 to 6.07, 3.85, and 2.42, with the maximum always located at the hot face. The regions with higher thermal exposure correspond spatially to the regions with higher temperature; at

the end of the high-temperature hold stage of mission 50, the in-plane average temperature of each layer through the thickness monotonically increases from 590.9 °C at the cold face to 619.3 °C at the hot face.

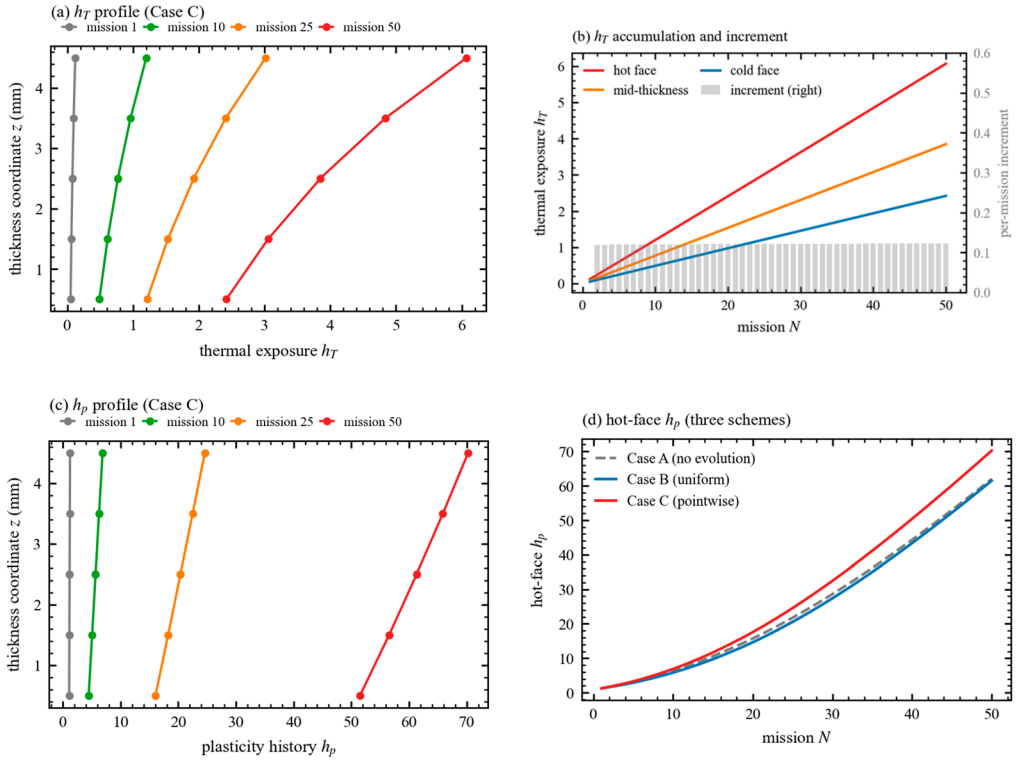


Figure 9. Evolution of the service history field of the thin plate with mission count (Case C; (**d**) includes the Case A reference). (**a**) Through-thickness profile of the thermal exposure history; (**b**) thermal exposure accumulation trajectory and per-mission increment; (**c**) through-thickness profile of the plasticity accumulation field; (**d**) variation in the hot-face plasticity history with mission count.

The thermal exposure accumulation has two features worth noting. First, the accumulation process is approximately linear. The temperature field of Case A does not vary with mission, and its hot-face thermal exposure increment per mission is constantly 0.1195; the increment of Case C slowly increases from 0.1195 to 0.1226 with mission count, rising by only 2.6% within 50 missions. The slow rise is because thermal conductivity degradation causes the hot-face temperature to slightly increase mission by mission, and the temperature exponential weighting in Equation (28) makes the thermal exposure per mission slightly increase accordingly.

Second, the ratio of the thermal exposure accumulation at the hot face to that at the cold face of Case C remains 2.45–2.51 throughout, i.e., the distribution shape—more at the hot face, less at the cold face, monotonically decreasing from the hot face to the cold face—does not change with mission count.

The temperature field of Case C is approximately repeated mission by mission and the distribution shape remains stable; the reasons are: first, the mission profile of this paper is within the normal service temperature range of GH4169 (650 °C), no over-temperature load is applied, and therefore the assumed property degradation amplitude is small. The thermal conductivity degradation does not exceed 5%, and the change to the temperature field is less than 1 °C (the actual material property degradation should be measured experimentally). Second, the thin plate is only 5 mm thick; the in-plane conductive thermal resistance is much smaller than the cold-face convective thermal resistance; the temperature difference between the hot face and cold face is only about 28 °C; the temperature is approximately

uniform through the thickness; and the thickness difference in the thermal exposure is therefore stable.

Because the change in thermal conductivity is bounded (at most about 5%) and its effect on the temperature field is small (about 1 °C), the thermal exposure accumulates at an approximately constant rate over the service, with no significant degradation-accelerating accumulation. This behavior contrasts with the feedback amplification of the plasticity-history accumulation discussed below.

The distribution form of the plasticity history is similar to that of the thermal exposure history, but the temporal behavior differs. Figure 9c,d show the evolution of the Case C plasticity accumulation field with mission count, where Figure 9d includes the Case A reference trajectory. In mission 1, the whole plate yields: the maximum equivalent plastic strain is 2.498×10^{-3} for all three treatments, and the through-thickness difference is small (the ratio of the largest to the smallest layer maximum is only about 1.13), so the plasticity is not concentrated near the hot face.

By mission 50, the Case C hot-face plasticity history reaches 70.2, with the position always at the hot face. Unlike the linear accumulation of the thermal exposure, the plasticity accumulation accelerates mission by mission from mission 2 onward. The hot-face per-mission plasticity increment is 2.5×10^{-3} in mission 1, drops back to about 0.9×10^{-3} in mission 2. This drop originates from the special starting state of mission 1.

Mission 1 starts from a stress-free, plasticity-free initial state: the compressive stress in the heating stage increases continuously from zero, the hot-face layer begins to yield at about 150 s within the mission at a compressive stress of about −850 MPa, and the viscoplastic flow continues to develop throughout the 300 s hold stage, which contributes a plasticity increment of about 2.2×10^{-3}.

During cooling, the thermal expansion vanishes and the structure tends to recover its dimensions, but the hot-face layer has undergone unrecoverable plastic flow in the compressive direction during the hold stage, which is equivalent to this layer being permanently shortened. When the surrounding material that has remained essentially elastic recovers its full length, it pulls the shortened layer outward, so that the hot-face layer ends the parking stage with a residual tensile stress of about +170 MPa, and the cooling stage is accompanied by a reverse-yielding increment of about 0.3×10^{-3}.

Mission 2 starts with this residual tensile stress. The thermal compressive stress produced by heating must first offset the residual tensile stress and the back stress formed in mission 1 before the material can enter compressive yielding, so the onset of yielding is delayed from about 150 s to about 250 s; the overstress during the hold stage decreases accordingly, and the plasticity increment of this stage drops to about 0.6×10^{-3}, while the reverse yielding of the cooling stage is essentially unchanged. The total increment of mission 2 is therefore only about 0.9×10^{-3}.

From mission 2 onward, each mission starts from a similar residual-stress state, and the transient component of the first loading no longer appears. The increment then increases mission by mission, reaching 4.1×10^{-3} at mission 50; in terms of the dimensionless history increment ($\Delta h_p = \Delta p / p_{ref}$, $p_{ref} = 2 \times 10^{-3}$), the segmental averages are 0.69 (missions 1–10), 1.18 (missions 11–25), 1.72 (missions 26–40), and 1.98 (missions 41–50), the later stage being about 2.9 times the early stage. The main source of this acceleration is the cyclic softening and back-stress evolution determined by the hardening rate of the constitutive model. As the cycling proceeds, the yield surface size contracts mission by mission, and the viscoplastic overstress under the same load history increases accordingly.

Case A, which does not consider degradation, likewise accelerates by 2.7 times (dimensionless segmental average 0.64 → 1.76). Property degradation acts further on this basis: it lowers the yield strength and hardening modulus, making the yield surface size

smaller, and the overstress of the material under the same external load is larger and the viscoplastic flow is faster (Equation (20)). The per-mission plasticity increment of Case C is therefore 2% (mission 2) to 16% (mission 25) higher than that of Case A, with a slight decline thereafter (12% higher at mission 50). Note that this figure refers to the per-mission increment; the corresponding underestimation of the accumulated plastic strain is reported in Section 4.3.3. The per-mission plasticity increment difference between Case C and Case A is small because the assumed degradation amplitude of the property retention factor is small. The strength material parameters decrease by no more than about 16% within 50 missions (on the basis of the cyclic yield strength at the hole edge); when the degradation amplitude is larger, the difference between the two will increase accordingly.

This means that the plasticity accumulation of subsequent missions is not a simple repetition of the initial response. Even if the material properties do not degrade at all, linear extrapolation based on the first-mission plasticity increment would significantly underestimate the later accumulation rate.

The average histories of the three treatments are very close, but the spatial distributions differ, and the formation time of the feedback amplification is worth noting. Case B adopts volume-average history update; its through-thickness average thermal exposure at mission 50 (4.054, averaged over the layer averages of five thickness layers) differs from that of Case C (4.047) by about 0.2%. This indicates that the average histories of the two treatments evolve along similar paths, but the spatial distributions are completely different (Case B has no through-thickness difference). The degree of feedback amplification is measured by comparing the history of Case C with that of Case A.

Case A does not update properties, but the program still records the local history at each point; the history of Case C is accumulated under the condition that each mission continues to be computed with the updated properties, i.e., the degradation of the previous mission affects the response and accumulation of the next mission. The excess of the Case C hot-face plasticity history relative to the Case A record at missions 5, 10, 25, and 50 is +3.1%, +7.1%, +12.9%, and +13.3%, respectively; mission 25 already reaches 97% of the total excess over 50 missions. The excess of the Case C hot-face thermal exposure relative to the Case A record, within the same mission range, monotonically increases from +0.19% to +1.63%.

The differentiation of the through-thickness plasticity gradient among the three treatments can be clearly distinguished in the later missions (about missions 40–50); at mission 50, the ratio of the difference between the hot-face and cold-face layer-average plasticity accumulation to their average is 30.8% for Case C, 29.9% for Case A, and only 0.5% for Case B. The gradient of Case B nearly vanishes because the whole field degrades according to the same retention factor: the history difference between the hot face and the cold face is averaged out, and the plasticity accumulation through the thickness tends to be uniform.

4.1.2. Property Retention Factor Field of the Thin Plate

In the thin plate, the variation in the property retention factor formed by the three treatments with mission count is shown in Figure 10, and the comparison of the evolution paths of Case A and Case C is quantified in the following paragraph. By mission 50, the Case C hot-face retention factors of the elastic modulus, thermal conductivity, and initial yield strength are 0.956, 0.950, and 0.910, respectively, and the saturated cyclic yield strength retention factor is 0.900; the corresponding cold-face values are 0.971, 0.963, 0.934, and 0.926. The degradation amplitude decreases in the order of saturated cyclic yield strength, initial yield strength, thermal conductivity, kinematic hardening modulus, and elastic modulus; this ordering is consistent with the setting order of mechanism sensitivity. Spatially, the degradation of the strength parameters is deeper at the hot face than at the

cold face, corresponding to the hot-face-dominated history distribution discussed above in this section.

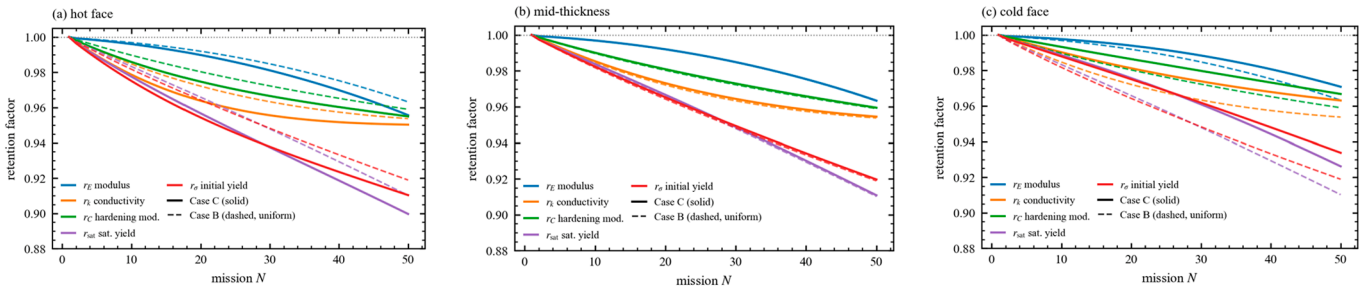


Figure 10. Variation in the property retention factor at representative positions of the thin plate under the three schemes with mission count. Solid lines: Case C, dashed lines: Case B (uniform update).

The influence of feedback on the property evolution prediction itself is measured by the path difference between Case A and Case C: substituting the hot-face layer-average history recorded by Case A (plasticity history 61.98, thermal exposure history 5.974) into Equations (29)–(31) for offline computation gives an initial yield strength retention factor of 0.9141, while the actual Case C hot-face value is 0.9104, a difference of +0.0037. Under the same algorithm, the perforated-plate hole edge gives 0.8766 vs. 0.8753 (difference +0.0013), and the thick-plate hot face gives 0.999248 vs. 0.999255 (difference about -1×10^{-5}). In all three rows, the comparison is between the offline computation from the history recorded by Case A and the actual Case C value at the same position, which is a different pairing from the recomputation verification of Table 3; the recomputed values there are paired with the program output of the same case, and the two pairs must not be cross-read. The path differences in all three structures are small, indicating that under the degradation amplitude assumed in this paper, the influence of feedback on the prediction of the property evolution path (retention factor trajectory) is limited.

Table 3. History recomputation verification of the property retention factor (mission 50; region-averaged basis: layer averages for the thin and thick plates, through-thickness averages for the perforated plate).

Position	h_p	h_T	Recomputed r_σ (Equations (29)–(31))	Program-Output r_σ	Deviation
Thin-plate hot face	70.23	6.072	0.9091	0.9104	−0.0013
Thin-plate cold face	51.48	2.420	0.9324	0.9338	−0.0014
Perforated-plate hole edge	144.96	4.054	0.8742	0.8753	−0.0011
Perforated-plate far field	43.76	4.042	0.9299	0.9310	−0.0012
Thick-plate hot face	0.62	0.016	0.9992	0.9993	-1×10^{-5}
Thin-plate hot face (offline computation from Case A recorded history)	61.98	5.974	0.9141	0.9104 (Case C actual value)	+0.0037

It should be emphasized that this holds only for the prediction of the property evolution path; the influence of feedback on the structural response is not negligible: the hot-face plasticity history of Case C is 13% higher than that of Case A; ignoring feedback would underestimate the damage accumulation, and life-type assessment must consider feedback.

The spatial difference in the property field of the thin plate exists only under pointwise update (Case C): Case A does not evolve, and Case B updates uniformly over the field; neither has a spatial difference in the retention factor. The spatial difference (maximum

minus minimum over all integration points) of Case C grows with mission count: the spatial difference in the initial yield strength retention factor increases from 0.013 at mission 10 to 0.026 at mission 50, and that of the saturated cyclic yield strength retention factor increases from 0.012 to 0.031 (Figure 11). Whether the spatial non-uniformity of degradation is considered directly determines whether the property field has a spatial difference.

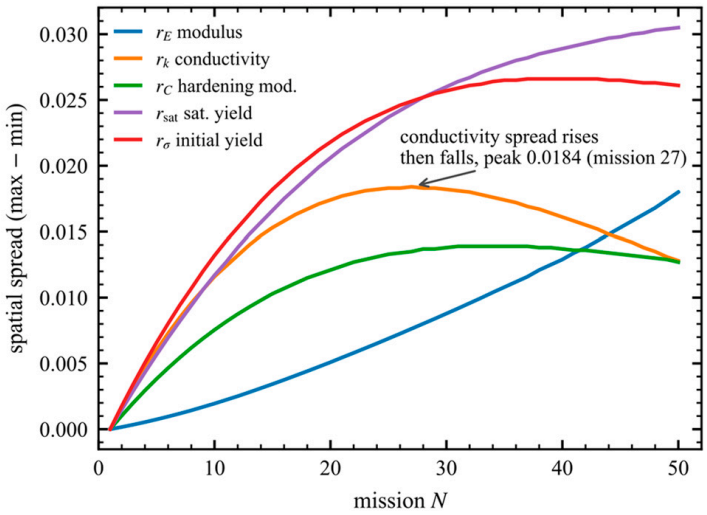


Figure 11. Variation in the spatial difference in each property retention factor of the thin-plate Case C with mission count.

The difference among the material property fields formed by the three treatments in the thin plate is mainly reflected in the spatial distribution (hot face vs. cold face), rather than in the through-thickness average property. Case B takes a single uniform retention factor over the field; its saturated cyclic yield strength retention factor is 0.9102, differing from the Case C through-thickness average of 0.9119 by less than 0.2%. Within Case C, by contrast, the values at different positions differ: the hot face is 0.012 below the through-thickness average and the cold face is 0.014 above the average, with the deviations in the two directions being opposite.

Figure 12 shows the comparison of the spatial distribution of the initial yield strength retention factor at mission 50. For the nonlinear property evolution mapping, the uniform property computed from the volume-average history (the field-reduction rule of Case B) is not equal to the volume average of the local properties at each point of Case C. The average histories of Case B and Case C are almost identical (differing by about 0.2%), but the histories at each position of Case C are strongly non-uniformly distributed along the thickness, and the nonlinear mapping amplifies this difference into a discernible local property difference.

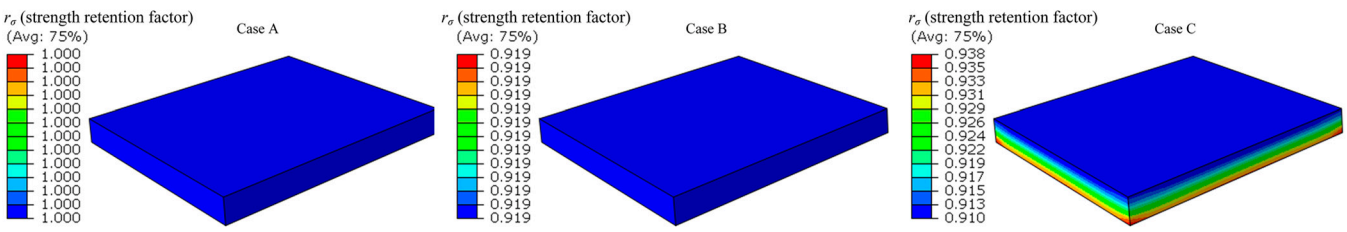


Figure 12. Comparison of the spatial distribution of the initial yield strength retention factor of the thin plate at mission 50 under the three schemes.

4.1.3. Perforated Plate with Hole-Edge Degradation

The plasticity history of the perforated plate exhibits a completely different spatial form from that of the thin plate. Figure 13 shows the variation in the history at the hole edge ($r < 8$ mm) and the far field ($r > 30$ mm) with mission count. In mission 1, the hole-edge equivalent plastic strain is 0.0051 (far field 0.0020), and the hole-edge Mises peak reaches 1496.6 MPa. The stress concentration makes the hole edge the position of concentrated plastic deformation from the first mission. Thereafter, the ratio of the hole-edge to far-field plasticity history first rises and then falls: 2.58 at mission 1, a maximum of 6.10 at mission 10, and 4.84 and 3.31 at missions 25 and 50 (Case C, arithmetic mean over the integration points of each region).

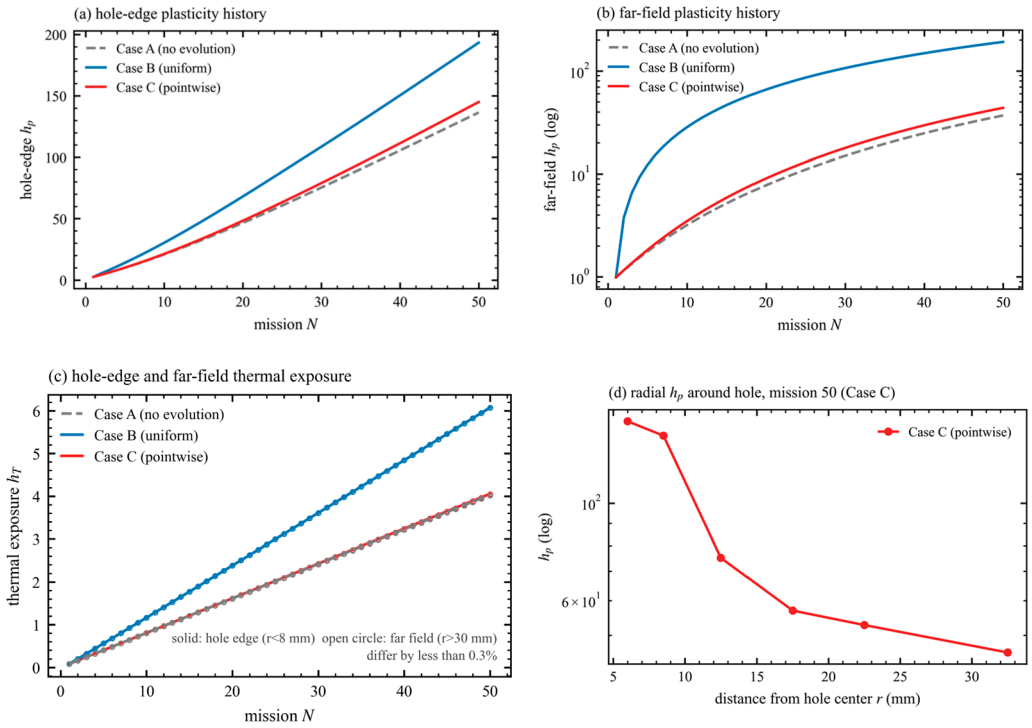


Figure 13. Variation of h_p and h_T at the hole edge and far field of the perforated plate with mission count (three schemes), and the radial distribution of h_p around the hole at mission 50. (**a**) Hole-edge plasticity history; (**b**) far-field plasticity history; (**c**) hole-edge and far-field thermal exposure history; (**d**) radial distribution of the plasticity history around the hole at mission 50 (Case C).

The ratio falls back rather than continuing to rise because the far field does not enter shakedown: its plasticity history rises monotonically from 0.99 at mission 1 to 43.8 at mission 50, and its per-mission equivalent plastic strain increment accelerates from segment to segment, from 0.00070 over missions 1–10 to 0.00128, 0.00220 and 0.00284 over missions 11–25, 26–40 and 41–50. The far field nevertheless accelerates faster than the hole edge (over the 50 missions, the segmental average increments of the two grow by factors of 4.1 and 1.6, respectively), so the ratio of the two keeps falling; at the end of the window, the increment ratio is 2.4, still below the accumulated ratio of 3.3, with no sign of leveling off. The presence of the hole barely affects the accumulation of the thermal history, because the hole wall is an adiabatic boundary condition and has little influence on the temperature distribution of the perforated plate; the hole-edge thermal exposure (4.054) and the far field (4.042) therefore differ by less than 0.3%. This indicates that the hole effect acts mainly through the plasticity history channel rather than the thermal exposure channel, in contrast to the thin-plate mode dominated by the hot-face thermal exposure.

The property field of the perforated plate superimposes variations in-plane and through the thickness. Figure 14a shows the in-plane profile around the hole at mission 50; the Case C hole-edge initial yield strength retention factor is 0.872 (degradation 12.8%), the band at 10–15 mm from the hole center recovers to 0.912 (degradation 8.8%), and the far field is 0.930 (degradation 7.0%). These in-plane values are read from the radial profile; the hole-edge values in Tables 3 and 4 are averages over the r < 8 mm region and differ slightly because the two are grouped differently. The degradation gradient mainly affects the range of about 1 hole diameter outside the hole wall, i.e., within 15 mm from the hole center (hole radius 5 mm, 10 mm outside the hole wall); beyond this, it tends to the far-field level.

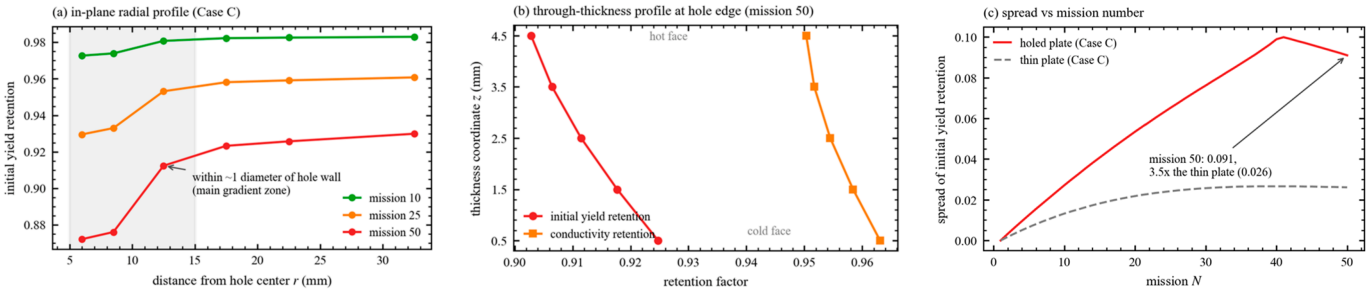


Figure 14. Property retention factor field of the perforated plate. (**a**) In-plane radial profile at mission 50; (**b**) through-thickness profile; (**c**) variation in the spatial difference in the initial yield strength retention factor with mission count (with thin-plate reference).

Table 4. Main response quantities of the three structures and their schemes at mission 50.

Structure	Scheme	Peak Compressive Stress (MPa)	Mises Peak (MPa)	Minimum Yield Margin (MPa)	Maximum Equivalent Plastic Strain	Peak Position z (mm)	r_σ
Thin plate	A	617.0	640.6	−16.79	0.1248	4.5	1.0000
Thin plate	B	594.8	621.0	−14.53	0.1387	4.5	0.9189
Thin plate	C	592.3	616.9	−14.96	0.1412	0.5	0.9104
Perforated plate	A	951.8	912.8	−18.91	0.3682	4.50	1.0000
Perforated plate	B	884.3	851.8	−13.82	0.3884	4.50	0.8553
Perforated plate	C	891.1	857.5	−16.85	0.3917	4.50	0.8753
Thick plate	A	920.8	920.7	+11.85	0.00126	18.75	1.0000
Thick plate	C	920.6	920.5	+11.74	0.00126	18.75	0.9993

Note: for the perforated plate, the maximum equivalent plastic strain is the hole-edge (r < 8 mm) region maximum and the retention factor r_σ is the hole-edge region average; for the thin plate and the thick plate, the maximum equivalent plastic strain is taken in the hot-face layer and the retention factor r_σ is the hot-face layer average.

Through the thickness (Figure 14b), the hot-face layer initial yield strength retention factor is 0.903 and the cold-face layer is 0.925; the hot face degrades deeper, with the same hot-face-dominated pattern as the thin plate; the intersection of the hole edge and the hot-face layer is the position of the deepest degradation in the field. The thermal conductivity retention factor has no in-plane gradient (0.95559 at the hole edge and 0.95563 at the far field) and only a small gradient through the thickness, because the thermal history is determined by the temperature field, and the in-plane temperature spread of the perforated plate is only 0.07 K, whereas the through-thickness difference reaches 28.4 K. The presence of the hole does not affect the thermal history channel.

In addition, along the direction outward from the hole center, the distribution curve of the retention factor at each position (circumferential profile) essentially does not change shape within 50 missions. Taking the hole-edge degradation depth as 1 and converting the degradation depth of each band to a ratio relative to the hole edge, the ratios of the bands at different distances from the hole center are essentially unchanged, and the influence range is always about 1 hole diameter outside the hole wall.

However, the ratio of each band varies with mission count: the ratio of the far-field band decreases from 0.62 at mission 10 to 0.55 at mission 50, because the far-field degradation is dominated by the thermal-exposure channel and grows slowly with missions, while the hole-edge degradation is driven by plasticity accumulation and grows faster. When the hole-edge degradation is used as the denominator to convert the ratio, the far-field proportion naturally decreases. The field spatial difference in the initial yield strength at mission 50 reaches 0.091, 3.5 times the field spatial difference in the thin plate (0.026, Figure 14c), indicating that the spatial non-uniformity of the property field of the perforated structure is far greater than that of the thin plate.

4.1.4. Thick Plate with Stagnant Degradation

The evolution of both the thermal exposure history and the plasticity history of the thick plate with mission count approximately stagnates, for two different reasons. Figure 15a,b show the variation in the Case A/C hot-face history of the thick plate with mission count, with the thin-plate curve at the same position as a reference; Figure 15c shows the evolution of each property retention factor of the thick plate Case C (enlarged display of the $r \approx 1$ interval). In terms of thermal exposure history, by the end of 50 missions, the Case C hot-face accumulation is only 0.0158, about 1/380 of that of the thin plate at the same position. The direct reason for the difference is that the hot-face layer average temperature at the end of the hold stage is 493.7 °C for the thick plate and 619.3 °C for the thin plate, a difference of 125.6 °C.

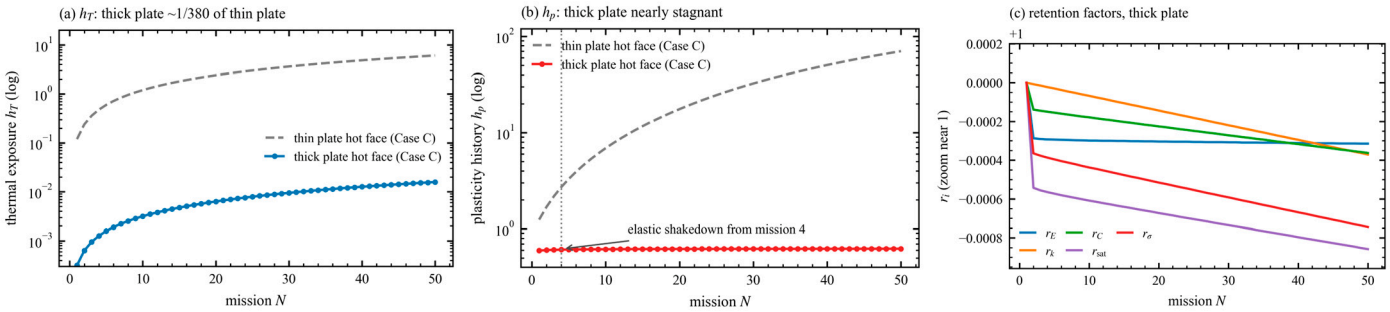


Figure 15. Service history and property evolution of the thick plate (Case A/C). (**a**) Hot-face thermal exposure history trajectory (logarithmic coordinates, with thin-plate reference); (**b**) hot-face plasticity history trajectory; (**c**) variation in each property retention factor with mission count (enlarged $r \approx 1$ interval).

In Equation (28), the temperature is weighted exponentially, and the higher the temperature, the faster the accumulation; a 125.6 °C temperature-level difference makes the thermal exposure accumulation rate differ by about 2.5 orders of magnitude. In terms of plasticity, the thermal stress in mission 1 causes the material to yield (maximum equivalent plastic strain 1.2×10^{-3}), but cyclic softening and stress relaxation bring the high-temperature hold stage of the thick plate into the elastic range from mission 4. The plasticity increment within that stage falls to zero, and the residual plasticity increment comes entirely from reverse yielding in the cooling stage, decaying from 1.5×10^{-5} at mission 2 to 1.5×10^{-7} at mission 50, tending to elastic shakedown, although shakedown is not reached

within the window, and the hot-face plasticity history within 50 missions only increases from 0.60 to 0.62 (+4.6%).

The property field of the thick plate barely evolves. By the end of 50 missions, the Case C hot-face initial yield strength retention factor is 0.9993 and the thermal conductivity retention factor is 0.9996; the field spatial difference is below the 10^{-3} order of magnitude. This is a direct consequence of the stagnation of the dual-channel history in Section 4.1; the variation in each property retention factor of the thick-plate hot-face layer with mission count is shown in Figure 15c.

4.1.5. Verification of the History-Property Correspondence

Finally, the pointwise correspondence between the property field and the local history is verified. The history at each integration point of five representative regions of the three structures at mission 50 is substituted into Equations (29)–(31), and the resulting retention factors are then averaged over each region to give the recomputed initial yield strength retention factor. The five positions are the thin-plate hot face and cold face, the perforated-plate hole edge and far field, and the thick-plate hot face; the thin plate and thick plate take layer averages, and the perforated-plate hole edge and far field take through-thickness averages. Compared with the region-averaged values output by the program for the same case, the deviation of the recomputed results does not exceed 0.003 (Table 3).

This indicates that, at the positions examined, the property field in the structural response is determined pointwise by the local history to within the deviation reported above, without the need for additional correction for a specific structure.

It should be noted that the retention factor is a nonlinear function of the history quantities, so that a region-averaged property must be obtained by computing the retention factor pointwise and then averaging, not by averaging the history quantities first and then substituting them into the mapping. The difference between the two procedures grows with the spatial variance of the history quantities and is most pronounced at the perforated-plate hole edge, where the history quantities span the widest range; the difference between the two procedures is about 0.012 there.

The same verification also shows that the degradation at different positions is dominated by different history quantities: in the degradation of the thin-plate hot-face initial yield strength, the contribution of thermal exposure (0.050) is slightly larger than that of plasticity accumulation (0.043), dominated by thermal exposure. At the hole edge, the contribution of plasticity accumulation (0.095) is larger than that of thermal exposure (0.047), shifting to plasticity accumulation dominance; at the hole far field, the contribution of thermal exposure (0.046) still exceeds that of plasticity accumulation (0.027), although the latter is no longer negligible. That is, the same material can be dominated by different history quantities at different positions, which is exactly the manifestation of the spatial non-uniformity of property evolution.

4.1.6. Synthesis Across the Three Structures

Synthesizing the results of the three structures, the history accumulation under the same mission profile covers the complete range: the thin plate has linear accumulation of the thermal exposure history and accelerating accumulation of the plasticity history, both growing continuously. The perforated plate has an approximately uniform field thermal exposure history, with the plasticity history concentrating at the hole edge and accelerating with mission count; the thick plate stagnates in both. Whether history accumulation occurs and in what spatial form is controlled by two factors directly related to the structure: the surface temperature level determines the rate of thermal exposure accumulation, and whether continuous yielding occurs determines whether plasticity accumulation can continue.

It should be noted that the separate driving of history accumulation by the two channels of thermal exposure and plasticity is a setting of the evolution model in this paper (Equations (29)–(31)); the distribution forms of the history accumulation described above are the source of the differences in the property fields of the three structures.

4.2. Reference Response and Simplified-Treatment Deviations

This section holds the treatment of material property evolution fixed and compares the thermal and mechanical responses of the three structures. First, the reference response behavior of the three structures is given using pointwise-update Case C, and then the deviations of no-evolution Case A and uniform-update Case B relative to Case C are sequentially presented. The mechanical response results include the stress field and peak compressive stress, yield margin, per-mission plasticity increment, extent of the plastically affected zone, and compressive-stress peak position.

4.2.1. Reference Response of the Thin Plate

The thin plate is analyzed first, under pointwise update (Case C). Figure 16 shows the temperature field at prescribed instants of mission 25 (Case C), and Figure 17 shows the variation curves of the cold-face average temperature and cold-face heat flux with intra-mission time. In mission 1, the maximum temperature difference among the three treatments is less than 0.01 °C; by mission 50, the through-thickness temperature differences (the difference between the hot-face and cold-face surface temperatures during the hold stage) of the three treatments are 27.13 °C (Case A), 28.42 °C (Case B), and 28.37 °C (Case C). In Case C, the region with a larger temperature gradient is located on the hot-face side, spatially corresponding to the position of the deepest thermal conductivity degradation (hot-face retention factor 0.950).

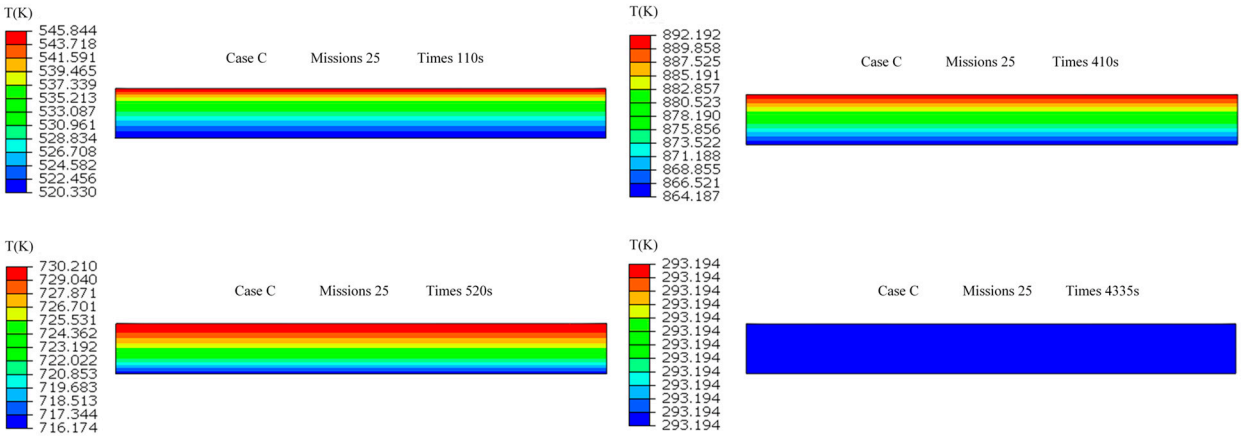


Figure 16. Temperature field of the thin plate at prescribed instants within mission 25 (Case C); each panel carries its own temperature range, so that the through-thickness gradient remains visible at every instant.

The difference in the cold-face thermal response is even smaller: in mission 50, the cold-face maximum temperature, peak heat flux, and heat transfer per mission of Case A are 591.37 °C, 114.27 kW/m^2, and 46.38 J/mm^2, respectively, and those of Case C are 590.90 °C, 114.18 kW/m^2, and 46.35 J/mm^2, respectively, with relative deviations all about 0.08% (cold-face temperature difference +0.47 °C). The direct reason for the small difference is that the degradation at the cold face itself is shallow (cold-face thermal conductivity retention factor 0.963); a more fundamental reason is that the bottleneck of the cold-face heat-transfer chain is at the cold-face boundary convection, as analyzed in the thermal-resistance composition given below.

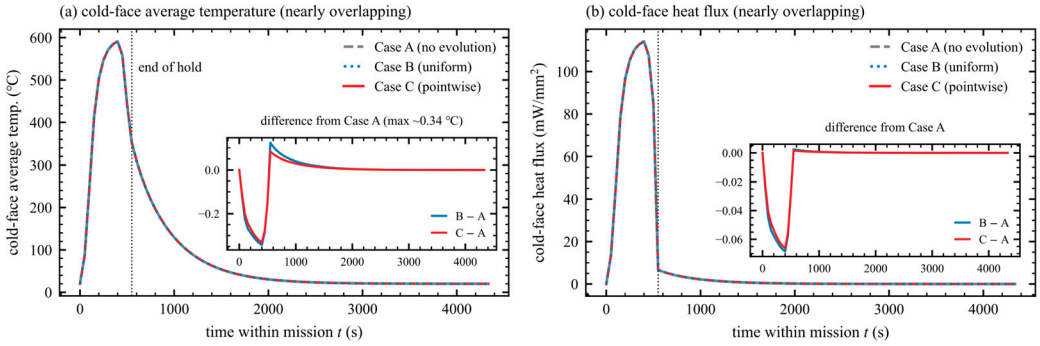


Figure 17. Cold-face thermal response of the thin plate with intra-mission time (three schemes; the curves of the three schemes nearly coincide). (**a**) Cold-face average temperature; (**b**) cold-face heat flux.

Within mission 25, the cold-face temperature variation curves with time of the three treatments nearly coincide, with a maximum difference of 0.34 °C over the whole process (between Case B and Case A; the maximum difference between Case C and Case A is 0.33 °C), less than 0.1% of the cold-face peak temperature; the heating-stage slope, hold-stage plateau, and cooling-stage temperature decay rate are essentially the same.

In addition, the temperatures of the three treatments at the end of the parking-cooling stage are completely identical (20.04 °C), indicating that the inter-mission interval is sufficient to eliminate the residual temperature from the previous mission, so that the temperature field repeats from the same initial state in every mission. The mechanical state, by contrast, is not reset: the residual stress and the plastic deformation carry over to the next mission, and the constitutive history quantities accumulate continuously from one mission to the next, which is precisely what allows the degradation evolution of this paper to advance mission by mission.

The reason why the cold-face thermal response of the thin plate is insensitive to evolution lies in the thermal-resistance composition. The cold-face temperature is determined by the series chain of in-plate conduction and cold-face convective heat transfer. In the thin-plate structure, the in-plate conductive thermal resistance $R_{cond} = B/k \approx 2.5 \times 10^{-4}$ m$^2\cdot$ K/W is only 5% of the cold-face convective thermal resistance $R_{conv} = 1/h_b = 5.0 \times 10^{-3}$ m$^2\cdot$K/W; the bottleneck of the heat-transfer chain is at the cold-face boundary. A thermal conductivity degradation of order 5% contributes only about 0.3% to the total thermal resistance, insufficient to produce a discernible temperature change at the cold face.

The hot-face temperature difference between Case A and Case C (0.62 °C) can be explained in the same way: the change in the in-plate thermal resistance first acts on the heated hot-face side, and the hot-face temperature is therefore most directly affected by the thermal conductivity change; the degradation is small but directly changes the conduction on the hot-face side.

The same series thermal-resistance relation also determines the feedback strength between the thermal conductivity degradation and the temperature field. A decrease in the hot-face thermal conductivity raises the hot-face temperature; the high temperature, through the Arrhenius weighting of Equation (28), increases the thermal exposure accumulation, and the thermal-channel degradation accelerates accordingly. This closed loop can be quantitatively resolved in the thin plate: in mission 50, the Case C hot-face average temperature is 0.62 °C higher than that of Case A, and the hot-face thermal exposure accumulation is correspondingly 1.6% larger. However, its strength is limited: the thermal conductivity degradation amplitude itself is only about 5%; the induced hot-face

temperature rise is less than 1 °C; and the amplification of the thermal exposure is less than 2%.

Next, the stress relaxation and stress distribution of the thin plate are examined. Figure 18 shows the evolution of the in-plane stress field of Case C at the end of the high-temperature hold stage with mission count, and Figure 19 shows the variation in the peak compressive stress of the three treatments with mission count. In mission 1, the stress curves of the three treatments completely coincide; thereafter, the stress of the whole plate relaxes mission by mission, and the peak compressive stress decreases from 1121.4 MPa to 617.0 MPa (Case A), 594.8 MPa (Case B), and 592.3 MPa (Case C) at mission 50, with total relaxation amplitudes of 45.0%, 47.0%, and 47.2% respectively; half of the relaxation is completed by mission 16. The relaxation amplitudes of the three treatments have a clear but small difference.

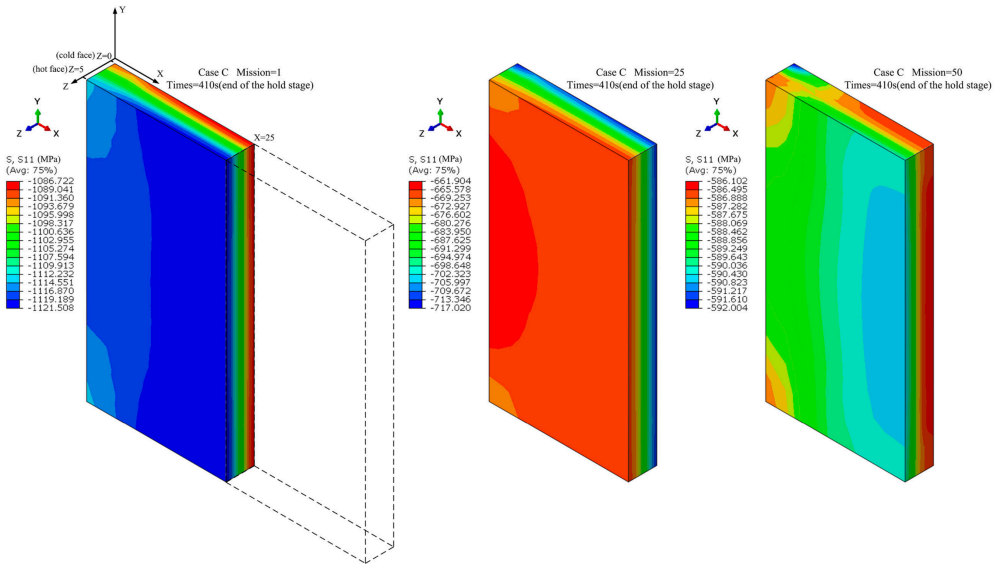


Figure 18. Evolution of the in-plane stress field of the thin-plate Case C at the end of the high-temperature hold stage with mission count.

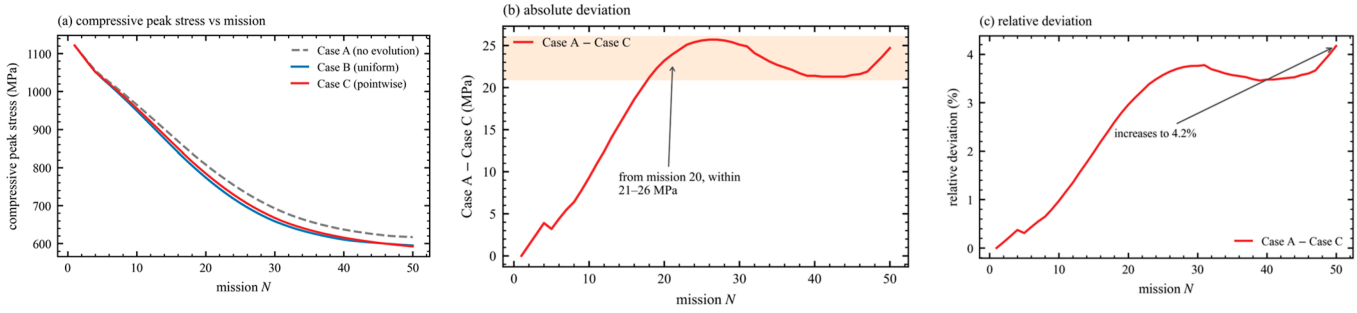


Figure 19. Variation in the peak compressive stress of the thin plate under the three schemes with mission count.

Case A is the smallest and Case C the largest, consistent with the expectation that degradation makes the yield surface smaller and the relaxation deeper; this also indicates that the main source of relaxation is the cyclic constitutive behavior during the high-temperature hold stage, and property degradation contributes about 2 percentage points of additional relaxation. The stress distribution through the thickness synchronously tends to become uniform: the difference between the maximum and minimum of the in-plane average compressive stress of each layer at the end of the hold stage decreases from

30.4 MPa at mission 1 (identical for the three treatments) to 7.7 MPa (Case A), 11.5 MPa (Case B), and 2.7 MPa (Case C) at mission 50.

The stress distribution of Case C is the most uniform, corresponding to the spatial distribution of strength degradation: the hot-face side, where the degradation is deepest, has the most yield-surface contraction, viscoplastic flow most easily occurs, and the stress relaxation during the hold stage is deepest; the initial "high at the hot face, low at the cold face" stress gradient is thereby gradually smoothed out. The uniform degradation of Case B does not make its stress distribution more uniform than that of Case A.

Case B degrades the whole field according to the same retention factor, without narrowing the strength difference between the hot face and the cold face; after the plastic development of each layer is redistributed, the inter-layer stress difference is instead slightly larger than that of Case A. The position of the peak compressive stress changes accordingly. All three treatments undergo the same early migration: the peak sits at the hot face (z = 4.5 mm) in missions 1–4 and moves to the cold-face side (z = 0.5 mm) from mission 5 onwards. Note that Case A, which does not degrade at all, migrates in the same way, so this migration originates from the structural form and the temperature gradient itself and is unrelated to property degradation. The three differ only at the end of the window: Case A returns to the hot face at mission 47 and Case B at mission 41, whereas Case C stays on the cold-face side throughout all 50 missions. This difference is what relates to the deepest degradation and the most complete hold-stage relaxation at the hot face of Case C.

4.2.2. Reference Response of the Perforated Plate

The thermal response of the perforated plate is almost identical to that of the thin plate. The in-plane temperature spread of the perforated plate is only 0.07 K and the thermal exposure is approximately uniform between the hole edge and the far field (Section 4.1); the thermal response difference between Case A and Case C is therefore of the same order as that of the thin plate.

The mechanical response of the perforated plate first manifests as the attenuation of the hole-edge stress concentration with mission count, and the manner of attenuation variation with mission count differs depending on the treatment of material property evolution. In mission 1, the full-field Mises peak is 1496.6 MPa (identical for the three treatments) and is located at the hole edge.

The peak then decays monotonically with mission count, and its location does not migrate. The mission-level maximum occurs within the hole-edge band in every one of the 50 missions: the centroid radius of the element carrying the within-mission maximum is 6.99 mm for all 50 missions, and the hole-edge maximum is the within-mission full-field maximum. It should be noted that this is a mission-level statement: over the transition frames between the heating and hold stages of a few missions, the instantaneous full-field Mises peak can appear in the cold-face layer about 11–15 mm outside the hole wall (about 10 frames each in missions 8, 10 and 12, reaching, at most, 98% of that mission's maximum); this behavior disappears after mission 25 as degradation accumulates.

The peak value therefore tracks the hole-edge behavior throughout and reflects the interaction of stress concentration with local degradation.

The reason Case B attenuates more lies in its uniform-update field-reduction rule: the spatially uniform update of the perforated plate does not take the volume average, but applies the field maximum history (i.e., the history at the hole edge) as the uniform value to the whole field, so that regions with inherently weak degradation also degrade at the hole-edge level and the stress level is therefore systematically lower. The Mises peak within the hole-edge region exhibits a different form, decaying monotonically with mission count: for Case C, it decreases from 1496.6 MPa in mission 1 through 986.6 and

868.1 MPa in missions 10 and 25 to 857.5 MPa in mission 50, a total decrease of 42.7%, while the corresponding values for Case A and Case B decrease to 912.8 and 851.8 MPa.

Case B and Case C are nearly identical at the hole edge, consistent with the setting that the uniform update directly adopts the hole-edge history. From mission 25 for Case A, mission 23 for Case B and mission 24 for Case C onward, the hole-edge maximum Mises no longer occurs within the high-temperature hold stage but at the start of the mission, i.e., at the residual stress state left by the parking-cooling of the previous mission. Regardless of the treatment, the most severe stress state at the hole edge occurs in the first mission.

Figure 20 shows the trajectories of the peak compressive stress and peak position of the three treatments with mission count, the attenuation of the hole-edge and full-field Mises peaks, and the circumferential stress contour around the hole at the end of the hold stage of mission 50.

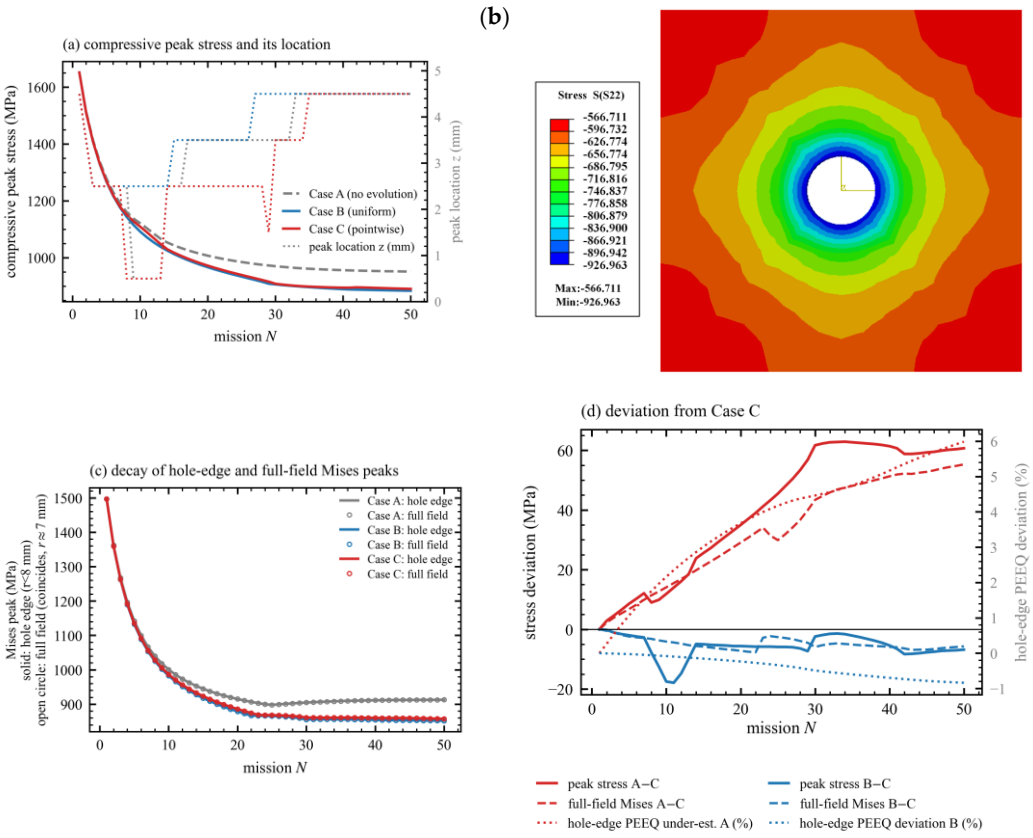


Figure 20. Mechanical response of the perforated plate. (**a**) Trajectories of the peak compressive stress and peak position of the three schemes with mission count; (**b**) circumferential stress contour around the hole in the hot-face layer at the end of the hold stage of mission 50 (Case C); (**c**) attenuation of the hole-edge (within 8 mm from the hole center) and full-field Mises peaks with mission count (three schemes; the full-field peak coincides with the hole-edge peak and stays at the hole-edge band r ≈ 7 mm throughout); (**d**) deviation trajectories of the peak compressive stress and the full-field Mises peak for Cases A–C and Cases B–C (left axis), and the deviation of the hole-edge maximum equivalent plastic strain (right axis).

4.2.3. Reference Response of the Thick Plate

The thermal response characteristics of the thick plate are opposite to those of the thin plate. Figure 21 shows the temperature field of the thick plate at prescribed instants within a mission and the parking–recovery curve. At the end of the hold stage, the hot-face surface temperature is 493.7 °C and the cold-face surface temperature is 386.1 °C, with a through-thickness temperature difference of 107.6 K; the corresponding values of the thin plate at the same mission instant are 619.3 °C, 590.9 °C, and 28.4 K.

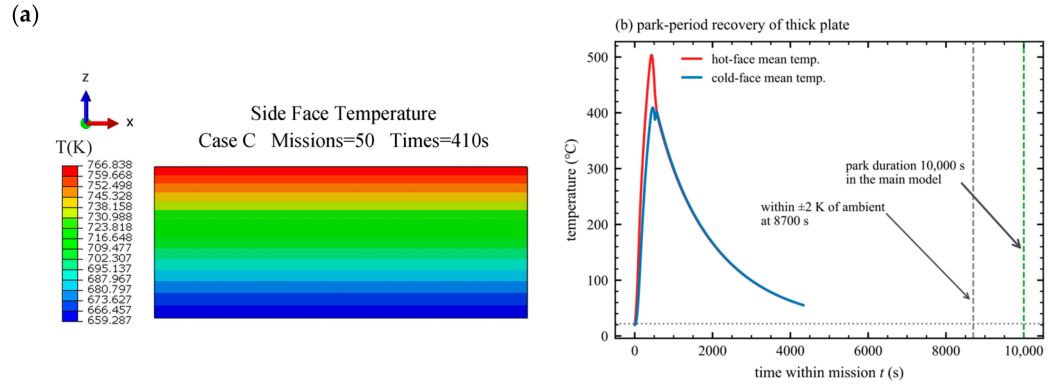


Figure 21. Temperature field of the thick plate at prescribed instants within a mission (side view) and the parking–recovery curve. (**a**) Side-view temperature field at the prescribed instants; (**b**) parking-period recovery curve of the thick plate.

The thick plate has a lower temperature level but a larger temperature gradient; the decrease in temperature level originates from heat storage: a fourfold increase in plate thickness amplifies the heat capacity accordingly, while the cold-face heat-transfer capacity remains unchanged, and the thick plate cannot reach the quasi-steady-state temperature level of the thin plate within the 520 s mission segment. The rise in temperature gradient originates from the thermal resistance: the in-plate conductive thermal resistance increases linearly with plate thickness, and under the same conductive heat flux, the thicker the plate, the larger the through-thickness temperature difference; the thermal-resistance ratio R_{cond}/R_{conv} rises from 0.05 to 0.21.

Since the evolution of both the thermal exposure history and the plasticity history stagnates, the thermal responses of Case A and Case C are consistent throughout all 50 missions: at mission 50, the end-of-parking temperatures of the two treatments agree digit by digit (the cold-face and hot-face readings being 20.89 °C and 20.90 °C, respectively), and the cold-face maximum temperature difference is less than 0.1%.

The thick plate, under the given mission profile, experiences a response of first plasticity and then a trend to elastic shakedown, without reaching it strictly within the 50-mission window. The thermal stress in mission 1 causes the material to yield; thereafter, cyclic softening and stress relaxation make the yield margin turn positive from mission 4 (+1.98 MPa), +6.9 MPa at mission 10, and +11.7 MPa at mission 50. From mission 4, the high-temperature hold stage remains elastic; the residual plasticity increment comes only from reverse yielding in the cooling stage and decays mission by mission; and the peak compressive stress value slowly decreases at a rate of about 0.04 MPa/mission. The compressive-stress peak position of the thick plate is always at the hot face ($z = 18.75$ mm) throughout all 50 missions, without the migration seen in the thin plate.

The peak-frame profile of the thick plate monotonically increases from the cold face (-795 MPa) to the hot face (-919 MPa), with an inter-layer stress difference of about 124 MPa (on the basis of the in-plane average stress of each layer). This is the stress difference caused by the through-thickness temperature gradient, far larger than the stress difference that property differences can cause, and the property differences in the thick plate are approximately zero due to the stagnation of degradation.

The stagnation of degradation does not mean that the thick plate is insensitive to property changes. To examine this, a separate comparison case is computed: without going through the evolution chain, the thermal conductivity is artificially reduced by 5% over the whole field. The results show that the thick-plate hot-face temperature rises by 3.2 °C and the cold-face temperature drops by 1.5 °C (about 0.37% of the cold-face maximum temperature), while the cold-face maximum temperature of the thin plate changes by only

0.09% under the same reduction (Figure 22a). That is, the thermal response consequence of the same property change is about 4.1 times larger for the thick plate than for the thin plate, because the in-plate conductive thermal resistance of the thick plate accounts for a larger share of the total thermal resistance (21% vs. 5%), and the influence of the thermal conductivity change on the total thermal resistance is greater.

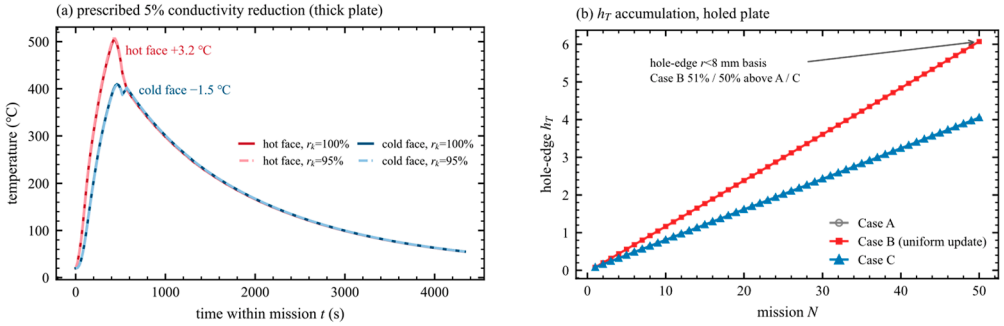


Figure 22. Fixed-degradation comparison of the thick plate. (**a**) Temperature response of the thick plate in the fixed-degradation-amplitude comparison (thermal conductivity 100% vs. 95%); (**b**) hole-edge thermal exposure accumulation of the perforated plate under the three schemes.

Synthesizing the three structures, the sensitivity of the thermal response to property changes increases monotonically with the thermal-resistance ratio, while the actual thermal effect of evolution depends on whether degradation occurs. The thin plate has low sensitivity but active evolution, and the actual effect is a relative change of 0.08% in the cold-face maximum temperature; the thick plate has high sensitivity but stagnating degradation, and the actual effect is approximately zero.

This means that although thick-section structures do not need to build an evolution model for mission-cycle degradation, once the properties change due to mechanisms other than cycling (such as oxidation, environmental erosion), the thermal consequences will be amplified by about 4.1 times by the thermal-resistance structure.

4.2.4. Case A Versus Case C Deviation

Next, the deviation of the no-evolution Case A relative to Case C is examined. The form of the Case A vs. Case C deviation of the thin-plate peak compressive stress with time depends on which metric is used for comparison. In terms of absolute difference (MPa), the deviation rapidly widens in the early service stage and enters the 21–26 MPa range from mission 20; the maximum within the range appears around missions 24–26 (compressive stress +25.7 MPa, Mises stress +31.2 MPa). Thereafter, it transitions to a form of first decreasing, then increasing, low in the middle and high at both ends (the peak compressive stress deviation drops to +21.3 MPa around missions 42–44), and slightly rebounds at the end of the window, reaching +24.7 MPa at mission 50.

In terms of relative difference (percentage relative to Case C), the deviation grows monotonically within the 50-mission window, from 1.0% at mission 10 to 4.2% at mission 50, with mission 50 being the maximum over the whole process. The two metrics have different forms because of the denominator: the stress level of Case C continuously decreases with relaxation, and the base of the absolute deviation shrinks accordingly; the relative deviation is the absolute deviation divided by the Case C stress level, and the denominator is decreasing, so even if the absolute deviation remains unchanged or slightly decreases, the relative deviation will continue to increase. The stress deviation from ignoring feedback is determined by the competition of two opposing effects: the property degradation difference accumulates with mission count and widens the deviation, while the whole-plate stress overall decreases with softening and relaxation, shrinking the absolute deviation.

When evaluating the stress deviation brought by the simplified treatment, it is necessary to first specify the metric used for comparison (absolute difference or relative difference), i.e., to compare under the same conditions; hereafter, unless otherwise specified, both the absolute difference and the relative difference are given.

The yield margin and plastic response of the thin plate exhibit a pair of coexisting opposing trends. Figure 23 shows the variation in the minimum yield margin, per-mission plasticity increment, and plastically affected zone with mission count. At mission 50, the minimum yield margin of Case C is −15.0 MPa. The yield margin is the minimum of the difference between the yield surface size and the equivalent stress over the field at the end of the hold stage; a negative value corresponds to the overstress state of Perzyna viscoplasticity, located at the hot face. The maximum per-mission plasticity increment is 4.1×10^{-3} (hot face). The plastically affected zone in Figure 23c is a cumulative measure: it is defined as the fraction of integration points whose accumulated equivalent plastic strain exceeds 10^{-6}, and records the range that has ever entered plasticity; it is non-decreasing and does not fall back on elastic unloading. This fraction has been 100% since mission 20, i.e., the whole plate has been reached by plastic deformation. This does not mean that the whole plate is flowing at every instant: within mission 50, only 24.5% of the integration points have a plastic increment during the heating stage (t = 50–100 s), 100% during the high-temperature hold stage (t = 150–400 s) and 9.2% during the unloading stage (t = 450–500 s), rising again to nearly 100% before the end of the parking stage.

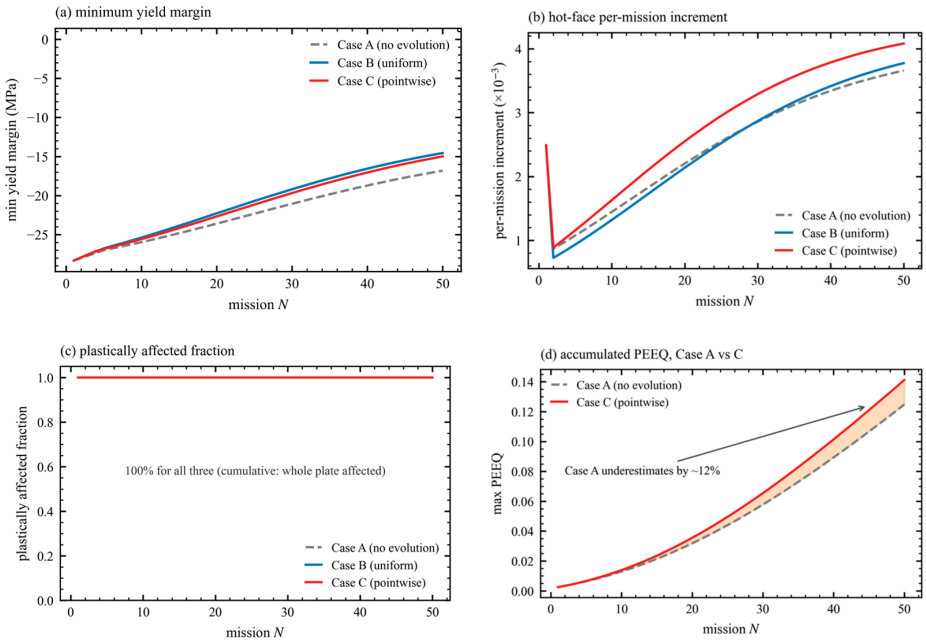


Figure 23. Variation in the yield state and plastic response of the thin plate with mission count. (**a**) Minimum yield margin; (**b**) hot-face per-mission plastic increment; (**c**) plastically affected fraction; (**d**) accumulated equivalent plastic strain of Case A and Case C, where the shaded band is the amount by which Case A underestimates the accumulation.

The yield margin slowly recovers with mission count: the three treatments recover by 11.53, 13.79, and 13.36 MPa, respectively, from −28.3 MPa in mission 1, reaching −16.79, −14.53, and −14.96 MPa at mission 50; Case A recovers the slowest throughout, and its difference from Case C continuously widens to −1.83 MPa, with no sign of ceasing to widen. At the same time, the hot-face per-mission plasticity increment continuously grows (2.5×10^{-3} to 4.1×10^{-3}), and the maximum equivalent plastic strains of the three treatments are 0.1248, 0.1387, and 0.1412, respectively. The two trends appear contradictory but share the same cause.

The yield surface size continuously decreases with cyclic softening and degradation, so that the material more easily enters viscoplastic flow and the overstress under the same load becomes greater; the per-mission plasticity increment therefore continuously grows. At the same time, the stress relaxation during the high-temperature hold stage continuously deepens, the equivalent stress at the end of the hold stage continuously decreases, and the difference between the equivalent stress and the yield surface size (yield margin = yield surface size—equivalent stress) therefore recovers. A faster recovery does not mean a larger margin.

The recovery is fastest in Case B, but the margin of Case A is still the farthest from zero; the stress level itself (Case A is the highest) is the main determinant of the absolute value of the margin. For the damage accumulation (accumulated plastic deformation, thermal exposure) on which life assessment is based, ignoring feedback underestimates the accumulated plasticity by 11.6% (in terms of the maximum equivalent plastic strain, Case A vs. Case C), and the underestimation continuously grows with mission count, biasing the life assessment toward the non-conservative side.

In the perforated plate, the Case A vs. Case C deviation of the whole-plate peak compressive stress is +60.7 MPa (+6.8%), higher than the +4.2% of the thin plate, i.e., the stress concentration amplifies the whole-plate deviation brought by ignoring feedback. This phenomenon happens for two reasons. First, the evolution relation has a saturation upper limit: the plasticity history of the hole edge is 6.10 times that of the far field at mission 10 and decays thereafter, and the property contrast into which Equation (30) maps it has narrowed to only about 1.06 by mission 50. Second, the region of concentrated degradation at the hole edge coincides with the location of the whole-plate peak compressive stress, so that the local degradation acts directly on the quantity that governs the strength assessment, and the two no longer offset one another.

However, the form of the deviation variation with time differs from that of the thin plate. The Case A vs. Case C compressive stress deviation, after small fluctuations in the early service stage, grows from mission 20 onwards (from +35.0 MPa at mission 20 to a window maximum of +62.9 MPa at mission 34, then back to +58.8 MPa at mission 42 and +60.7 MPa at mission 50), without the range-fluctuation form seen in the thin plate, because the hole-edge degradation continuously accumulates and there is no whole-plate relaxation-rebound mechanism.

The deviation magnitude also differs depending on the response quantity examined: at mission 50, the peak compressive stress deviation is +6.8% (+60.7 MPa), while the full-field Mises peak deviation is +6.4% (+55.3 MPa); the two are of the same order because both the peak compressive stress and the full-field Mises peak are located at the hole edge, so that hole-edge degradation affects the two quantities with similar strength.

The hole-edge local quantities and failure position of the perforated plate exhibit different deviation characteristics. The Case A vs. Case C deviations of both the hole-edge equivalent plastic strain and the hole-edge plasticity history are −6.0% (maximum-value basis within the hole-edge region), i.e., Case A underestimates the hole-edge plasticity accumulation, biasing the life assessment toward the non-conservative side; therefore, when conducting life assessment at the hole edge, evolution cannot be ignored. The same direction of error is reported in other structural contexts, where degradation-coupled life prediction under variable-amplitude and variable-frequency loading is an active concern and where ignoring the degradation feedback likewise biases the life estimate toward the non-conservative side [31,32].

The Case A versus Case C deviation of the hole-edge maximum Mises at mission 50 is +55.3 MPa (+6.4%), i.e., ignoring evolution overestimates the hole-edge stress level, in the same direction as the peak compressive stress deviation. At mission 50, the peak

compressive stress position of all three treatments is in the hot-face layer (z = 4.50 mm, element-layer center coordinate). This is not constant over the whole window: across the 50 missions, the peak layer of the three treatments varies between z = 0.50 and 4.50 mm, with Case A in the hot-face layer 19 times, Case B 25 times and Case C 17 times; at mission 50, all three are in the hot-face layer. At the end of the hold stage (about 400 s within the mission), the in-plane average S11 of each layer of the perforated plate has the same compressive sign as that of the thin plate. The hole-edge circumferential stress exhibits a compressive stress concentration, with the hoop average of the first ring of elements around the hole wall being about −835 MPa, more compressive than the −594 to −622 MPa of the thin plate at the same instant, which results from the hole-edge stress concentration combined with the plastic relaxation induced by degradation.

At the end of the parking-cooling stage (20 °C), residual tensile stress remains in the hole-edge band of the perforated plate in Case C, with the first ring of elements around the hole wall averaging about +871 MPa and the far-field band (r > 30 mm) still retaining +588 MPa, about 68% of the hole-edge value rather than decaying to zero. This residual stress arises because the cooling contraction is restrained by the normal elastic supports on the four side surfaces, so that the far field cannot contract freely either; the hole edge carries the highest residual tension because it accumulates the most plastic deformation.

The mechanical response of the thick plate is essentially identical between Case A and Case C. Because the degradation of both channels stagnates for the thick plate, the property retention factors of Case C remain close to 1, and its computed response is practically the same as that of a no-evolution treatment. At mission 50, the peak compressive stress difference between the two cases is 0.2 MPa (920.8 vs. 920.6), the yield margin difference is 0.11 MPa, the maximum equivalent plastic strain agrees to within 0.000001 (0.001256 for Case A against 0.001257 for Case C), and the layer-by-layer compressive stress profile at the peak compressive stress occurrence instant of the two material property treatment schemes nearly coincides point by point (Figure 24, maximum layer difference 0.3 MPa).

Next, the deviations among the three structures between Case A (no evolution) and Case C are compared. In terms of strength and insulation indicators, the deviation from ignoring evolution does not exceed about 7% for the reference parameter set within the 50-mission window in terms of peak stress: the whole-plate peak compressive stress is 4.2% higher in the thin plate, 6.8% higher in the perforated plate, and less than 0.1% in the thick plate. Comparing peak stresses alone is not, however, sufficient to establish that the strength assessment is conservative, because Case A also retains the initial strength properties whereas these properties are reduced in Case C.

The yield margin is therefore compared on the basis of the current strength. The margin is defined as the minimum over all integration points of $Y - q$, where $Y = \sigma_{y0}(T) \cdot r_\sigma + R$ is the current (degraded) yield-surface radius and q is the Perzyna overstress; a larger margin is safer. At mission 50, the Case A minus Case C margin difference is −1.83 MPa in the thin plate and −2.06 MPa in the perforated plate, i.e., ignoring evolution gives a smaller margin and is therefore conservative, but the magnitude of this deviation is 12.2% and 12.2% of the respective Case C margins (−14.96 MPa and −16.85 MPa). The margin deviation is thus noticeably larger than the 4.2% and 6.8% peak-stress deviations, because the margin is a difference in two comparable quantities and is more sensitive to the treatment of evolution than the stress itself; assessing conservatism from a stress percentage alone would underestimate the influence.

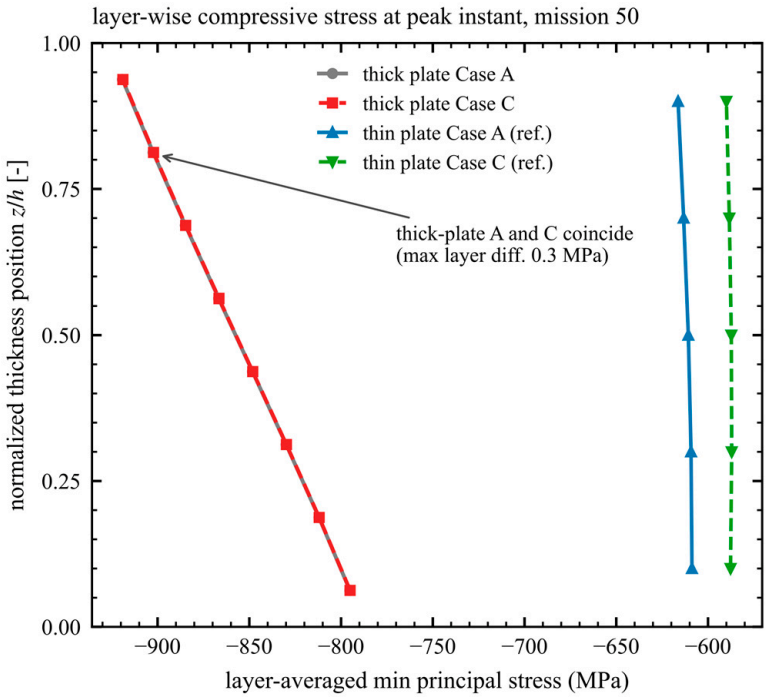


Figure 24. Layer-by-layer compressive stress profile of the thick plate at the peak frame of mission 50 (Case A/C), with thin-plate reference; the ordinate is the normalized thickness position z/h, and the thin plate is mapped by relative thickness position for morphological comparison only.

The thick plate is the exception: its margin difference is +0.11 MPa, i.e., ignoring evolution gives a marginally larger margin (0.9% of the Case C margin of 11.74 MPa) and is therefore slightly non-conservative, although the magnitude is negligible. The statement that ignoring evolution is conservative should accordingly be limited to the thin plate and the perforated plate; the cold-face temperature overestimation of the thin plate and perforated plate does not exceed 0.5 °C (Case A higher than Case C; the thick plate is approximately zero). This is because the material without strength degradation maintains a higher stress level, and strength checks based on it yield conservative results.

The damage accumulation on which life assessment and over-temperature inspection are based is the opposite. Ignoring the inter-mission feedback causes the plasticity accumulation to be continuously underestimated—by about 11.6% for the thin plate and about 6.0% at the perforated-plate hole edge at mission 50—and the shortfall widens as service proceeds, which makes the life assessment non-conservative; the hot-face temperature and hot-face plasticity history are also underestimated. The root of the opposite deviation directions of the two types of indicators lies in: strength degradation lowers the stress level, making the no-evolution assumption conservative on the strength side, while the feedback amplification of degradation with temperature and plasticity increases the hot-face damage accumulation, making the no-evolution assumption non-conservative on the life side.

From this, the first applicability conclusion is drawn: in strength checks, not considering the evolution of material properties overestimates the structural stress, and the design is conservative for the thin plate and the perforated plate, while the thick plate is slightly non-conservative in the margin by a negligible amount. In life assessment and over-temperature inspection (checking whether the hot-face temperature exceeds the material allowable temperature), not considering the evolution of material properties underestimates the damage accumulation, and a pointwise property update treatment must be adopted.

4.2.5. Case B Versus Case C Deviation

The uniform-update treatment (Case B vs. Case C deviation) is examined next. The thin-plate degradation distribution is mild (maximum through-thickness difference about 0.03), and the uniform update is approximately valid; at mission 50, the peak compressive stress deviation is only 0.4%, and the thermal-response deviation does not exceed 0.2%. The perforated-plate degradation is concentrated at the hole edge, and the sign of the resulting response deviation then depends on the representative value chosen: the field maximum lowers the peak compressive stress by 0.8% while the volume average raises it by 3.1%, so that the main consequence of spatial homogenization is not the magnitude of the response deviation but the conservatism of the retention factor it produces. To demonstrate this, two independent representative histories are compared: the field maximum and the volume average. A third choice, the history at the location of maximum stress, was also considered; that location coincides with the field maximum (the full-field Mises peak, the plasticity history peak and the equivalent plastic strain peak are all carried by the same element el801 at r = 6.9940 mm), so that choice provides no independent information (Section 4.2).

The two cases differ only in the source of the representative history; the thermal-analysis scaling, the zero-degradation injection at mission 1 and the restart protocol are identical, and the mission-1 input decks of the field-maximum case and the volume-average case are byte-identical (identical MD5 checksum), so the two results are directly comparable. At mission 50, the injected plasticity histories of the field-maximum and volume-average cases are 189.9 and 62.0, a factor of 3.06 apart, while the injected thermal-exposure histories are 5.99 and 3.97, a factor of 1.51 apart; the resulting strength retention factors are 0.8553 and 0.9174, 6.21 percentage points apart.

Correspondingly, the two thermal-exposure histories are much closer to one another than the two plasticity histories, because the thermal-exposure history is an integral of a smooth temperature field, whereas the plasticity history accumulates locally. How strongly the choice of representative value matters therefore differs greatly between the two channels, and no single scalar can bound the pointwise response. Taking the volume average would pull the hole-edge history (3.3 times the far field at mission 50) down to the average level, systematically underestimating the hole-edge degradation and biasing toward the non-conservative side.

Taking the field maximum (adopted in this case study) degrades the whole field according to the hole-edge level, with the field initial yield strength retention factor dropping to 0.855, 2.0 percentage points deeper than the 0.875 of Case C at the hole edge (the uniform histories injected into mission 50 are h_p = 189.9 and h_T = 5.99, taken from the field-maximum accumulation at the end of mission 49 of Case B), and at mission 50, the peak compressive stress is 0.8% lower and the full-field Mises peak is 0.7% lower.

The deviation is not monotonic over the window, reaching a maximum of about 1.6% around missions 10–11 and then falling back, so that "not exceeding 1%" holds for the final mission but not over the whole window, while the field-uniform thermal conductivity degradation alters the temperature field itself (thermal exposure overestimated by 2.2% relative to the field-maximum basis of Case A and by 0.5% relative to Case C, and accumulating with missions).

Case B is not computed for the thick plate: due to the stagnation of degradation, even if compared, its results would be consistent with the Case A vs. Case C comparison (both differences less than 0.1%). From this, the second applicability conclusion is drawn: under the field-maximum injection rule adopted in this case study, the main effect of the spatially uniform treatment is the conservatism of the retention factor it produces rather than the magnitude of the structural response deviation. The response deviation depends on how close the uniform value is to the actual value at the critical point: under volume-average

injection, the peak compressive stress deviation of the perforated plate is +3.1%, of opposite sign to the field-maximum injection.

The only exception in the thermal response of the perforated plate is Case B: the field-uniform thermal conductivity degradation (retention factor 0.95) raises the temperature field overall. At mission 50, the Case B thermal exposure accumulation reaches 6.07 as the hole-edge region average ($r < 8$ mm), about 51% higher than the 4.03 of Case A (4.05 for Case C), and this overestimation accumulates with mission count. Figure 22b, which plots the thermal exposure of the hole-edge region ($r < 8$ mm), namely 4.0315 for Case A, 6.0719 for Case B and 4.0537 for Case C, is not on the same basis as the field-maximum values used above (6.114 for Case B, 5.985 for Case A, 6.083 for Case C). The relative difference shown in the figure is therefore larger and the two must not be read interchangeably. As a reference, the local thermal conductivity degradation at the hole edge of Case C (4.4%) has an influence on the temperature field of less than 0.03%, and the above positive feedback is not activated. That is, the positive feedback is negligible in Case C because the degradation is confined to the hole edge (temperature change less than 0.03%), and is significantly amplified in Case B because the degradation is applied to the whole field. Under the evolution model of this paper, the uniform update of the perforated plate not only averages out the spatial distribution of degradation but also alters the temperature field itself.

4.2.6. Summary of Response Quantities

The summary of the main response quantities of the three structures at mission 50 is listed in Table 4, where the maximum equivalent plastic strain and $r\sigma$ of the perforated plate take the values of the hole-edge ($r < 8$ mm) region; those of the thin plate and thick plate take the values of the hot-face layer; the maximum equivalent plastic strain of all three structures follows a unified maximum-value basis; the Mises peak is the full-field value (for the perforated plate, the full-field peak coincides with the hole-edge peak at $r \approx 7$ mm), and the peak position z is the value at mission 50, taken as the element-layer center coordinate. The peak position of all three perforated-plate treatments lies in the hot-face layer; the peak positions of the thin plate in Case A and Case B and those of the thick plate in Case A and Case C are biased toward the hot-face side, while that of the thin-plate Case C shifts to the cold-face side, as analyzed in Section 4.2.

Synthesizing the three structures, the strength of the evolution effect on the mechanical response is determined by the relative magnitude of two quantities: the property gradient caused by degradation and the stress gradient caused by the temperature gradient of the structure itself. In the thin plate, the two are of comparable order of magnitude (the inter-layer stress difference at the end of the hold stage is about 7.7 MPa in Case A, reduced to about 2.7 MPa in Case C, i.e., a change of about 5 MPa caused by property degradation), and the stress distribution form changes with the degradation treatment.

In the thick plate, the stress difference caused by the temperature gradient is about 124 MPa (on the basis of the in-plane average stress of each layer), far larger than the influence of the property difference; the peak position is always unchanged; and the evolution effect is negligible.

In the perforated plate, the stress concentration deepens the hole-edge degradation to 12.5%, but the small region of concentrated degradation at the hole edge is uncorrelated with the dominant factor of the whole-plate peak compressive stress, and the evolution relation has a saturation upper limit (no matter how large the history difference, the property difference is compressed within a finite range). The whole-plate peak compressive stress deviation is of the same order as that of the thin plate. That is, the stress concentration deepens the hole-edge degradation by about a factor of 1.4 and enlarges the whole-plate

response deviation by about a factor of 1.6, the two amplifications being comparable, so that the deviation remains of the same order as that of the thin plate.

4.3. Engineering Consequences of the Evolution

4.3.1. How Property Change Reaches the Structural Response

The property changes reviewed in Section 4.1 reach the structural response through four channels, and the channels do not act on the same quantity. The stiffness channel acts on the thermal stress amplitude: in a structure whose thermal expansion is constrained, the stress generated by a given temperature difference scales with the elastic modulus, so the hot-face reduction in the elastic modulus to 0.956 of its initial value at mission 50 directly lowers the stress level. The strength channel acts on the size of the yield surface: the same reduction in the yield stress lowers the yield-surface radius by about 48 MPa at the hot face, which is the quantity that a strength check compares against.

The hardening channel acts on the rate of damage accumulation rather than on the stress level: cyclic softening and the reduction in the saturated cyclic yield stress make each mission accumulate more plastic strain than the last, so the damage accelerates even when the stress falls. The conductivity channel acts on the temperature field itself, and its effectiveness is not a property of the material alone but of the balance between the in-plate conductive resistance and the cold-face convective resistance, as quantified in Section 4.4.1. Superimposed on the four channels is the spatial dimension: because the channels are driven by local histories, the resulting property field is itself non-uniform, and the non-uniformity differs greatly between the plasticity and thermal-exposure channels. The consequences of each channel for design are examined in the four subsections that follow.

4.3.2. Conservative Strength Assessment

The strength consequence is examined first, because it is the point at which the intuitive argument is least reliable. Ignoring evolution raises the calculated peak compressive stress by 4.2% in the thin plate and 6.8% in the perforated plate, which suggests a modest conservative margin. The margin itself, however, is more sensitive than the stress, and the reason can be quantified directly. At the hot face at mission 50, the yield stress of the un-degraded material is 531.9 MPa and the strength retention factor is 0.9104, so the reduction in the yield-surface radius is 47.7 MPa. The net change in the minimum margin is only -1.83 MPa.

The difference between the two figures, about 46 MPa, is compensated by the over-stress term: the same degradation that lowers the yield surface also lowers the stress that pushes against it, because both are elastic-modulus driven. The margin is a difference in two comparable quantities, so a near-cancelation of the two large terms leaves a small residual whose relative magnitude is amplified: the margin deviation is 12.2% of the reference margin while the stress deviation is 4.2%, a factor of about 2.9. The perforated plate behaves in the same direction with a smaller amplification: its Case C minimum yield margin is -16.85 MPa and the Case A minus Case C margin difference is -2.06 MPa, again, 12.2% of the reference margin, while the corresponding peak-stress deviation is 6.8%, a factor of about 1.8. The two structures therefore share the same 12.2% margin deviation while their stress deviations differ, which shows that the margin deviation and the stress deviation have no fixed ratio. Assessing conservatism from a stress percentage alone therefore underestimates the influence.

For the thin plate and the perforated plate, the sign of the residual nevertheless means that ignoring evolution is conservative; the thick plate is the exception, with a margin difference of +0.11 MPa (0.9% of its Case C margin of 11.74 MPa), so that ignoring evolution is marginally non-conservative there, although the magnitude is negligible.

4.3.3. Underestimated Damage Accumulation

The life consequence runs in the opposite direction from the strength consequence, and this is the more serious of the two. Ignoring evolution underestimates the accumulated plastic strain (the time integral of the per-mission increment discussed in Section 4.1.1) by about 11.6% at the thin-plate hot face and by about 6.0% at the perforated-plate hole edge at mission 50, and this shortfall does not saturate but keeps growing as the missions accumulate. Because the accumulated plastic strain is the quantity that feeds both the property-evolution relation and any fatigue or creep damage assessment, the error propagates: an underestimated damage state gives a non-conservative remaining-life estimate, and the estimate deteriorates as the service proceeds. The direction of this error is consistent with the accelerated plastic accumulation identified in Section 4.2: the per-mission plastic increment grows by about a factor of three over the 50 missions, so the missions that accumulate the most damage are precisely those for which the no-evolution treatment is least accurate. For a design that is life-limited rather than strength-limited, ignoring inter-mission property evolution is therefore not conservative.

4.3.4. Geometric Condition for Thermal Protection

The thermal-protection consequence is conditional rather than uniform, and the condition is geometric. For the thin plate, the in-plate conductive resistance is only about 0.05 of the cold-face convective resistance, so the cold-face temperature is set mainly by the convective boundary and is almost independent of the thermal conductivity of the plate; the cold-face response is then insensitive to evolution, and, indeed, the temperature differences among the three treatments do not exceed 0.5 °C.

For the thick plate, the ratio rises to about 0.21. Here, the thermal resistance ratio is evaluated as the in-plate conductive resistance $R_{cond} = B/k$ divided by the cold-face convective resistance $R_{conv} = 1/h_b$, with the thermal conductivity taken at each structure's own working temperature (about 21.3 W/(m·K) for the thin plate and about 18.9 W/(m·K) for the thick plate, the material card rising from 13.4 to 23.6 W/(m·K) over 293–1073 K). The plate is four times as thick and the cold-face convective coefficient is the same, while the conductivity is slightly lower at the lower working temperature, so the ratio for the thick plate is about 4.5 times that of the thin plate. The in-plate conduction therefore clearly weighs more, and the same proportional change in conductivity has a much larger effect. The distinction is therefore not between structures that degrade and structures that do not, but between structures in which the degraded property lies in the controlling resistance and structures in which it does not. The following paragraph examines this for the thick plate, whose cyclic degradation stagnates for the reason given in Section 4.1, but which is nevertheless far from insensitive to property change.

The stagnation of cyclic degradation in the thick plate should not be read as insensitivity to property change in general. The comparison of Section 4.2 shows that a fixed 5% reduction in thermal conductivity changes the thick-plate cold-face temperature by 0.37%, about 4.1 times the thin-plate response under the same reduction, precisely because the thick plate has a large in-plate conductive share. For thick sections subjected to long service at elevated temperature, the mechanisms that dominate property change are therefore non-cyclic: long-term oxidation, coating degradation, and creep-oxidation interaction. The framework of this paper can accommodate such mechanisms without structural change, because the thermal-exposure channel is an integral of the temperature history and does not depend on the number of cycles; supplying the activation energy and the characteristic history of another mechanism is sufficient to add it as a further channel in Equation (31). What the framework does not currently represent is a mechanism whose driving quantity is not reducible to a history integral, such as crack initiation.

4.3.5. Critical Locations for Inspection and Repair

The location of the full-field stress peak and the location of the deepest degradation are the same place in the perforated plate: throughout the 50 missions, the within-mission stress maximum lies in the hole-edge band at r = 6.9940 mm, and the hole-edge maximum is the within-mission full-field maximum (Section 4.2).

It should be noted that this is a mission-level statement: the instantaneous full-field peak can appear in the cold-face layer in a few transition frames, and this behavior disappears after mission 25 as degradation accumulates.

The two locations coinciding does not mean that the two questions are the same one. Strength is governed by the stress peak and remaining life by the degradation depth, and these are different quantities. The hole-edge Mises peak decays monotonically with mission count, from 1496.6 MPa at mission 1 to 857.5 MPa at mission 50 for Case C, a total decrease of 42.7%, whereas the degradation at the hole edge keeps deepening, with its initial yield strength retention factor falling to 0.875 at mission 50. The two move in opposite directions within the window of this paper, so it is not defensible to relax hole-edge inspection on the grounds that the stress peak is falling.

Inspection and repair should be planned by degradation depth, i.e., at the hole edge and within about one hole diameter outside the hole wall, rather than by the stress peak position of the first mission or by the trend of the stress peak. This affected range remains stable over the 50 missions, as shown in Section 4.1.3.

4.4. Validity Conditions and Scope of the Results

4.4.1. Thermal-Response Conditions and the Cold-Face Convection Coefficient

The conditions for the validity and robustness of the above results need to be clarified. The thermal-response conclusions rely on three conditions. First, the ratio of plate thickness to thermal conductivity is small enough that the in-plate conductive thermal resistance is much smaller than the cold-face convective thermal resistance; second, the thermal conductivity degradation amplitude is limited to no more than 5% in this paper; third, there is no additional insulation layer or oxide layer that significantly changes the interface thermal resistance. If any condition is broken, the in-plate conductive thermal resistance share rises, and the sensitivity of the thermal response to the local update will increase.

The robustness of the evolution parameters is verified by a parameter sweep with amplitudes of 0.5–2 times; during the sweep, the degradation amount and spatial difference in each property vary approximately linearly with the amplitude, and the spatial distribution form—deepest at the hot face, shallowest at the cold face—and the relative magnitude of the degradation of each property remain unchanged. When the thermal conductivity degradation amplitude is doubled to 10%, the cold-face thermal-indicator deviation is still within the 1% engineering tolerance.

The thermal-response conclusion is further examined over the cold-face convective coefficient, because the ratio of the in-plate conductive thermal resistance to the cold-face convective thermal resistance increases with this coefficient. Twelve single-mission thermal analyses are carried out, combining a thin and a thick plate, three values of the convective coefficient (20, 200 and 1000 $W/(m^2 \cdot K)$; the case studies use 200) and two thermal-conductivity retention factors (1.00 and 0.95). The sensitivity of the cold-face temperature to conductivity degradation is non-monotonic in the convective coefficient: it is largest at 200 $W/(m^2 \cdot K)$ (0.090% for the thin plate and 0.367% for the thick plate) and falls back at 1000 $W/(m^2 \cdot K)$ (0.029% and 0.343%). Across all six combinations, the relative change in the cold-face temperature remains below 0.4%.

The reason is that a larger convective coefficient tends to clamp the cold face to the ambient temperature, so that the through-thickness temperature difference is accommo-

dated almost entirely within the plate; a change in conductivity then redistributes the temperature inside the plate rather than changing the absolute cold-face temperature. The hot-face temperature behaves in the opposite way: it rises when the conductivity degrades, and its sensitivity does increase with the convective coefficient, from 0.001% to 1.094% for the thin plate and from 0.122% to 2.208% for the thick plate, which remains below 2.3% in absolute terms. The cold-face conclusions of this paper are therefore stated for the range of 20–1000 W/(m^2·K) rather than for the single adopted value.

Beyond the amplitude sweep, the characteristic histories, the shape parameters and the channel contributions are varied separately in the extended analysis of Section 4.5. The limitations of the computation in this paper likewise need to be clarified. The computation does not consider oxidation and surface environmental effects, material microstructural evolution, or crack initiation and propagation.

At mission 50, the local maximum equivalent plastic strain of the thin plate is about 0.14 and that at the perforated-plate hole edge is about 0.39, well beyond the usual numerical range of the small-strain assumption. The accumulated equivalent plastic strain, however, is the path length of reversed plastic flow and is not a direct measure of geometric change.

At mission 50, the measured hole diameter changes by 1.5%, the thickness by 0.55% and the maximum displacement is 0.17% of the in-plane dimension, and apart from the displacement gradient (0.017 rad, i.e., 1.7%, of which the pure rotation component does not exceed 0.0037 rad), all geometric changes are within 1.5%, so the kinematic condition of the small-strain assumption holds.

It should also be noted that the displacement of the perforated plate still grows slowly within the 50-mission window (the increment per five missions falling from 0.0020 mm to 0.0005 mm) and has not reached full shakedown, so this judgment still requires re-examination for longer service. The results of this paper should be understood as a mechanistic analysis of the comparison of the three material property treatment schemes within the given parameter range.

4.4.2. Limits of Applicability

Two further limitations of the scope should be stated. First, the conclusion on the spatial uniformization of the property update is obtained for one hole diameter (10 mm) and one constraint condition (elastic edge support with $\eta = 4$).

The quantity that controls the error of the uniform update is the spatial non-uniformity of the degradation field. In this case study, the plasticity history ratio between the hole edge and the far field peaks at 6.10 at mission 10, falls back to 3.31 at mission 50, and corresponds to a strength retention factor difference of 0.056 (0.875 at the hole edge against 0.931 in the far field). At this level of degradation gradient, the whole-plate response deviation caused by the uniform update is of the same order as that of the thin plate with its mild degradation distribution, no more than 1% at mission 50 in both structures.

Over the whole window, the deviation stays within about 1.6%, the largest excursions being 1.5% at mission 24 for the thin plate and 1.6% at mission 11 for the perforated plate; injecting the field-maximum history does, however, give a lower retention factor than the pointwise hole-edge value (0.855 against 0.875).

The uniform update is therefore applicable to structures with a mild degradation distribution, whereas structures whose degradation is concentrated at a notch such as a hole or slot must be assessed case by case following Section 4.2.5, and the specific threshold has to be computed for each case.

Second, the mission profile, the aerodynamic heat flux and the boundary conditions are fixed as specified in Section 3.3, and the temperature during the hold stage remains below about 620 °C; the gamma-double-prime to delta transformation that GH4169 undergoes

above its long-term service temperature limit of about 650 °C [38], and the oxidation-dominated mechanisms of property change, are outside the scope examined here.

4.5. Extended Sensitivity Analysis

4.5.1. Design of the Extended Sensitivity Analysis

A sensitivity analysis that scales only the degradation amplitudes does not vary the characteristic histories, the shape parameters of the degradation functions or the relative contributions of the two history channels independently. This section reports a broader analysis in which those three groups are perturbed separately.

Seven cases are compared, namely the reference and six perturbed cases; the perturbed cases keep the identifiers they carry in the underlying case set, so the labels S1, S2, S5, S6, S7 and S8 are not consecutive. The reference is Case C of the thin plate (Section 4.2), so the extended analysis is a thin-plate analysis. Case S1 halves the characteristic plasticity history of all five properties, which doubles the corresponding degradation rates. Case S2 multiplies the characteristic plasticity history by about 1.5, slowing the degradation and bracketing S1 on the slow side. Case S5 doubles the history coefficient of the thermal-exposure channel and raises its saturation amplitude by a factor of 1.5. Case S6 does the same for the plasticity channel. Case S7 halves the shape parameter of both channels, which delays the early degradation and steepens the approach to saturation. Case S8 doubles the shape parameter, which brings the early degradation forward and softens the approach to saturation. Each case is a full 50-mission chain on the same mesh, with the same program and the same boundary conditions as the main cases; only the evolution parameters differ.

The comparability of the six chains is verified rather than assumed. Because mission 1 injects zero accumulated history, and because the degradation relation returns zero change when the history is zero irrespective of the history coefficient and the shape parameter, the first mission must reproduce the reference exactly. This is confirmed: the accumulated plasticity history at mission 1 is 1.24919 for all six perturbed cases and for Case C alike, and the peak compressive stress is 1121.4 MPa for all six, agreeing with the reference value to within its 0.1 MPa rounding. The mission-1 input decks of the cases and the reference are also identical.

4.5.2. Effect on the Case A Versus Case C Deviation

The quantity examined is the deviation of the peak compressive stress between the no-evolution treatment (Case A) and the reference treatment (Case C) at mission 50, which is the deviation that the strength assessment discussion of Section 4.3.2 is based on. Table 5 lists the results together with the retention factors reached at mission 50.

Three conclusions follow. First, the sign of the deviation is the same in every case: ignoring evolution raises the calculated peak compressive stress throughout, so the qualitative conclusion that the no-evolution treatment is conservative for the peak stress does not depend on the parameter choice.

Second, the magnitude of the deviation does depend strongly on the parameter choice: it ranges from 16.7 MPa in the case with the slowest degradation to 57.1 MPa in the case with the fastest, a factor of 3.4 relative to the smallest, against 24.7 MPa for the reference parameters, so that the reference value lies in the lower part of that range. Expressed as a fraction of the Case A peak stress, the range is 2.7% to 9.3%. Reporting a single figure for the deviation is therefore not defensible, and the range is reported instead.

Table 5. Extended sensitivity analysis of the thin plate: parameters perturbed, retention factors at mission 50, and the Case A versus Case C deviation of the peak compressive stress.

Case	Perturbation	r_E	r_{Ysat}	$r_{\sigma y}$	Peak Compressive Stress (MPa)	A−C Deviation (MPa)	% of Case A
Reference	reference parameters (Table 1)	0.963	0.912	0.921	592.3	+24.7	4.0
S1	plasticity history × 0.5	0.915	0.846	0.875	570.9	+46.1	7.5
S2	plasticity history × 1.5	0.977	0.936	0.940	598.5	+18.5	3.0
S5	thermal channel × 2; saturation × 1.5	0.954	0.884	0.889	583.8	+33.2	5.4
S6	plasticity channel × 2; saturation × 1.5	0.877	0.795	0.844	559.9	+57.1	9.3
S7	shape parameter × 0.5	0.980	0.944	0.946	600.3	+16.7	2.7
S8	shape parameter × 2.0	0.940	0.872	0.892	579.5	+37.5	6.1

Note: the retention factors in the table are arithmetic averages over the integration points of the whole field. They are therefore not on the same basis as the hot-face-layer or regional averages of Tables 3 and 4, the two bases differing by about 0.01 for the same case. Within a row, the three retention factors and the deviation are on the same basis and can be compared directly. A positive deviation means that ignoring evolution overestimates the peak compressive stress, and the percentage takes the Case A peak compressive stress of 617.0 MPa at mission 50 as the denominator; the relative differences quoted in Section 4.2.4 instead take the Case C value as the denominator, so the same comparison reads 4.2% there and 4.0% here. Both denominators are stated and the two figures must not be interchanged. In the Perturbation column, the plasticity history is the characteristic plasticity history of all five properties, the thermal and plasticity channels are the history coefficients of the respective channels, saturation is the saturation amplitude, and the shape parameter is that of the degradation function.

Third, the deviation broadly increases as the degradation becomes deeper, but not strictly monotonically. Ordering the six perturbed cases by their strength retention factor at mission 50, from deepest to shallowest, gives S6 (0.844, +57.1 MPa), S1 (0.875, +46.1 MPa), S5 (0.889, +33.2 MPa), S8 (0.892, +37.5 MPa), S2 (0.940, +18.5 MPa) and S7 (0.946, +16.7 MPa). S8 and S5 form one inversion, with S8 degrading less deeply yet deviating more. The deviation is therefore not determined by the depth of degradation alone but also by how that degradation is distributed over the service life: S8 concentrates the degradation in the early missions, so that although its retention factor at mission 50 is higher, the earlier degradation has already changed the whole response trajectory.

4.5.3. Parameters Which Control the Deviation

The monotonic relation above suggests that the deviation is controlled simply by how much the strength degrades. The comparison between the two channel cases shows that this is only part of the picture. Case S5, which doubles the thermal-exposure contribution, reaches a strength retention factor of 0.8885 and a deviation of 33.2 MPa. Case S6, which doubles the plasticity contribution instead, reaches a lower retention factor of 0.8439 but a much larger deviation of 57.1 MPa. The two cases differ in the elasticity retention factor as well, 0.954 for S5 against 0.877 for S6, because the thermal channel acts weakly on the elastic modulus by construction while the plasticity channel acts on it strongly.

The channel through which the parameters are varied therefore matters, not only how far the properties are pushed. The plasticity channel lowers the elastic modulus and so lowers the thermal stress that drives the whole response, whereas the thermal channel acts

mainly on the thermal conductivity and the strength, leaving the stress level closer to the reference. This is consistent with the four-channel description of Section 4.3.1 and with the finding there that the margin deviation is much larger than the stress deviation, since both reflect one property change propagating into several response quantities at once.

The two-channel cases also differ in when their effect appears. At mission 25, the deviation of S5 is the largest of all six perturbed cases at 53.2 MPa, while that of S6 is 37.6 MPa; by mission 50, the order is reversed, S5 having fallen to 33.2 MPa while S6 has risen to 57.1 MPa. The thermal-exposure history accumulates quickly in the early missions and then saturates, so the thermal channel expresses itself early; the plasticity history accumulates slowly at first and accelerates with mission count, so the plasticity channel expresses itself late. A sensitivity study carried out over a shorter service window would therefore identify a different controlling channel than one carried out over the full 50 missions. This is the substantive reason why sweeping the amplitudes alone is not sufficient, and it is reported here because it is not visible from the amplitude sweep.

4.5.4. Deviation Bound and Range of Validity

The practical form of these results is a bound rather than a single number. Within the parameter range examined here, and for the thin plate, taking the retention factor of the initial yield strength at mission 50 as the indicator of the degradation level, the Case A versus Case C deviation of the peak compressive stress remains below 25 MPa, or 4% of the Case A peak stress, provided the strength retention factor remains above about 0.92. Below that level, the deviation rises, though not monotonically: 37.5 MPa (6.1%) at 0.892, 33 MPa (5.4%) at 0.889, 46 MPa (7.5%) at 0.875, and 57 MPa (9.3%) at 0.844. The highest value among the six perturbed cases, 57 MPa, corresponds to a strength retention factor of 0.84, which is a substantially deeper degradation than the reference parameters produce. The bound above is a thin-plate bound and is not transferred to the other structures: the perforated plate, whose degradation is deeper and concentrated at the hole edge, reaches a larger deviation of the same sign, +60.7 MPa or 6.8% of its Case C peak compressive stress (Table 4).

Two limitations of the range should be stated. First, the six perturbed cases cover the fast-degradation side (S1, S6), the slow-degradation side (S2, S7), the relative channel contribution (S5) and the distribution of degradation over the service life (S8), but they are not a symmetric sample about the reference parameters. The reported range should therefore be read as the range covered by these six cases rather than as a confidence interval on the reference result. Second, the case in which the two channels are perturbed together, and the case in which the coupling exponents are varied, have not been examined; the coupling exponents are held at unity throughout this work because no experimental basis exists for assigning them a preferential value, and varying them would add a second free parameter acting on the same effect as the channel amplitudes.

None of these limitations affects the qualitative conclusion. Across the full range examined, and in every channel combination, ignoring inter-mission property evolution gives a conservative estimate of the peak stress and a non-conservative estimate of the accumulated plastic strain. What the extension establishes is that the magnitude of the strength-side margin should not be quoted from a single parameter set, and that the controlling channel changes over the service window.

The conditions on the mission profile, the heat flux and the boundary conditions stated in Section 4.4.2 apply to this extended analysis as well.

5. Conclusions

From the perspective of structural response, this paper examines the influence of the evolution of material properties with reuse on thermal protection structures. The computation is carried out under a unified cyclic thermo-mechanical mission profile, adopting the dual-history-driven (thermal exposure and plasticity accumulation) degradation model established in Section 2. Three structures—a thin plate, a perforated plate, and a thick plate—are set up, together with three treatments of material property evolution—no evolution (Case A), uniform update (Case B), and pointwise update (Case C)—each executed for 50 missions. The deviations in the structural response caused by the three treatments of material property evolution are comparatively analyzed, yielding the following main conclusions:

From the perspective of material evolution, the three structures exhibit distinct evolution behaviors. In the thin plate, both the thermal exposure history and the plasticity history grow continuously: the degradation is distributed deeper at the hot face and shallower at the cold face through the thickness. After 50 missions, the hot-face yield strength retention is 0.910 and the cold-face value is 0.934; the plasticity accumulation accelerates mission by mission, with the per-mission plasticity increment increasing about threefold within 50 missions. However, the main source of this acceleration is the cyclic softening and back-stress evolution themselves: Case A, which does not consider degradation, likewise accelerates by a factor of about 2.7. Property degradation plays two roles on this basis: first, it lowers the yield strength and hardening modulus, further shrinking the yield surface, so that the overstress under the same load is greater and the per-mission plasticity increment is 2–16% higher than that of Case A. Second, the degradation is spatially non-uniform, and the position with deeper degradation (the hot face) accumulates faster, so the gap between the hot face and the cold face gradually widens.

In the perforated plate, the thermal exposure history is approximately uniform over the field, while the plasticity history concentrates at the hole edge; after 50 missions, the hole-edge yield strength retention is 0.875 (degradation 12.5%), the band at 10–15 mm from the hole center retains 0.912 and the far field retains 0.930 in the radial profile. The degradation is concentrated within about one hole diameter outside the hole wall and does not spread outward within 50 missions; the position of the deepest degradation in the field is at the intersection of the hole edge and the hot-face layer.

In the thick plate, both types of history approximately stop accumulating, and the 50-mission cycling barely produces degradation (the yield strength decreases by only 0.07%), for two reasons. First, the hot-face surface temperature of the thick plate during the hold stage is 125.6 °C lower than that of the thin plate, and the thermal exposure accumulation rate grows exponentially with temperature—the higher the temperature, the faster the accumulation—so the thermal exposure accumulation of the thick plate over 50 missions is only about 1/380 of that of the thin plate. Second, the thick plate keeps the high-temperature hold stage elastic from mission 4, while the only remaining plasticity is reverse yielding during the cooling stage, and its increment decays mission by mission (to 1.5×10^{-7} at mission 50), so that it tends to elastic shakedown without reaching it strictly within the window.

From the perspective of the influence of the structure on the response, taking the pointwise update (Case C) as the reference, conclusions can be drawn at two levels. The first level concerns the influence brought by the treatment of material property evolution: keeping properties unchanged (Case A) overestimates the structural stress, with the strength-check deviation not exceeding about 7% for the reference parameter set within the 50-mission window (thin plate +4.2%, perforated plate +6.8%, relative to Case C), and the design is conservative for these two structures; the thick plate is the exception, being marginally

non-conservative, by a negligible amount. At the same time, it underestimates the damage accumulation (thin plate accumulated plasticity about 11.6%, perforated-plate hole edge about 6.0%), with the underestimation growing with mission count, biasing the life assessment toward the non-conservative side; the same direction of error is reported in other structural contexts, where degradation-coupled life prediction under variable-amplitude and variable-frequency loading is an active concern [31,32].

Uniform update (Case B) differs from pointwise update by only 0.4% in the thin plate with a mild degradation distribution and can be approximately applied; in the perforated plate with concentrated degradation, the response deviation at mission 50 also stays within about 1% (maximum over the whole window about 1.6%), because the absolute magnitude of the degradation gradient is limited. The choice of the uniform value does, however, govern how conservative the resulting retention factor is, with the field maximum giving 0.855 against the pointwise hole-edge value of 0.875, and the field-uniform thermal conductivity degradation also feeds back on the temperature field, raising the thermal exposure by 2.2% and 0.5% relative to the Case A field-maximum basis and Case C, respectively.

The second level concerns the patterns reflected by the comparison of the three structures: whether degradation occurs is determined by the surface temperature level and whether continuous yielding occurs, and the thin plate and the perforated-plate hole edge yield continuously and degrade actively, while the thick plate keeps the hold stage elastic from mission 4 and its degradation stagnates; therefore, the strength deviation is of the same order of magnitude in the thin plate and the perforated plate (4.2% and 6.8%) and is less than 0.1% in the thick plate. The thermal-resistance ratio of the structure determines the sensitivity to property changes: the ratio of the in-plate conductive resistance to the cold-face convective resistance is 0.21 for the thick plate (0.05 for the thin plate), and when the thermal conductivity is artificially reduced by 5% over the whole field, the thick-plate cold-face temperature changes by 0.37%, about 4.1 times that of the thin plate (0.09%). That is, although the per-mission cyclic degradation of the thick plate is negligible, it is more sensitive to property changes from mechanisms other than cycling.

Accordingly, within the degradation amplitude assumed and the 50-mission window of this paper, performing strength checks with unchanged material properties is acceptable (overestimating the stress by no more than about 7% for the reference parameter set, on the conservative side, for the thin plate and the perforated plate), while life assessment and over-temperature inspection should adopt a pointwise degradation model. Structures with a mild degradation distribution can adopt a field-uniform degradation for thermal protection thickness design, while for structures with connection holes and piping openings, the uniform value should be chosen so that the resulting retention factor is conservative. The two rules must be distinguished: the field-maximum rule lowers the peak compressive stress by 0.8%, whereas the volume average raises it by 3.1%, so only the field-maximum rule avoids underestimating the hole-edge degradation (Section 4.2.5); the degradation-concentrated region (about one hole diameter outside the hole wall) is the key position for inspection and life assessment.

The verification in Section 2.3 is a numerical verification: it establishes that the program implements the assumed constitutive and property-evolution relations correctly, and does not establish how accurately those relations reproduce the actual behavior of GH4169. The degradation parameters of this paper are assumed following GH4169 test data and literature trends rather than calibrated against dedicated tests, so the quantitative results should be read as a sensitivity study over the assumed parameters, not as experimentally validated predictions of material behavior. Within this scope, the main conclusions remain

robust under the parameter sweep and the extended sensitivity analysis of Section 4.5; the model does not include oxidation, crack initiation, or microstructural evolution.

The accumulated equivalent plastic strain reaches 0.39 at the perforated-plate hole edge at mission 50, well beyond the usual numerical range of the small-strain assumption; this quantity, however, measures the path length of reversed plastic flow rather than the geometric change itself, the corresponding net plastic strain amplitude being only 0.0203, a ratio of 19.3, because the material is repeatedly loaded in tension and compression under the thermal cycle. The geometric change is assessed directly—at mission 50, the peak displacement reaches only 0.17% of the in-plane dimension—and the geometric changes themselves remain small—the hole diameter changes by 1.5% and the thickness by 0.55%, while the largest displacement gradient between adjacent nodes, which carries both the strain and the rotation, is 0.017. The second-order terms omitted by the small-strain measure are therefore of order 1.4×10^{-4} in strain, below 1% of the strain itself, and because this truncation belongs to the formulation rather than to the treatment of evolution, it affects the cases compared here alike and largely cancels in the differences on which the conclusions rest. The displacement of the perforated plate nevertheless still grows slowly and has not reached full shakedown, so this judgment requires re-examination for longer service.

On this basis, the small-strain formulation is retained, and the conclusions of this paper are limited to the geometric range of the cases computed here, in which the peak displacement does not exceed about 0.17% of the in-plane dimension and the displacement gradient does not exceed 0.017. Future work includes recomputation after parameter calibration, real structural details such as hole arrays and stiffeners, and finite-strain extension.

Author Contributions: Conceptualization, P.Y., Y.G., L.L., D.W., X.Y., J.X. and Y.H.; methodology, P.Y., Y.G., L.L. and D.W.; software, P.Y. and Y.H.; validation, P.Y. and X.Y.; formal analysis, X.Y. and J.X.; investigation, P.Y.; writing—original draft preparation, P.Y., Y.H., J.X. and X.Y.; writing—review and editing, P.Y., Y.G., D.W., Y.H., J.X. and X.Y.; visualization, P.Y. and Y.H.; supervision, Y.G., L.L. and D.W. All authors have read and agreed to the published version of the manuscript.

Funding: This research was funded by the National Natural Science Foundation of China, grant number 92571203, and the National Numerical Wind Tunnel Project of China.

Data Availability Statement: The data presented in this study are available on request from the corresponding author. The raw finite element models and post-processing scripts can be provided upon reasonable request.

Acknowledgments: The authors gratefully acknowledge the financial support of the National Natural Science Foundation of China (92571203). This research was co-supported by the National Numerical Wind Tunnel Project of China. Generative AI tools (DeepSeek) were used to assist with text drafting and formatting. The authors have reviewed and edited the content and take full responsibility for the content of the publication. The simulation, result processing, and scientific conclusions are entirely the responsibility of the authors.

Conflicts of Interest: The authors declare no conflicts of interest.

References

1. Uyanna, O.; Najafi, H. Thermal protection systems for space vehicles: A review on technology development, current challenges and future prospects. *Acta Astronaut.* **2020**, *176*, 341–356. [CrossRef]
2. Hu, F.; Wang, J.; Sui, Z.; Lin, G.; Zhao, W.; Jin, H.; You, Y. A review on research progress of large area thermal protection structures for hypersonic vehicles. *Acta Astronaut.* **2025**, *232*, 541–556. [CrossRef]
3. Guo, Q.; Wang, S.; Hui, W.; Li, Y.; Xie, Z. Thermo-mechanical optimization of metallic thermal protection system under aerodynamic heating. *Struct. Multidiscip. Optim.* **2020**, *61*, 819–836. [CrossRef]

4. Mooij, E.; Vo, Q.T.; Offerman, J.W.P.I. Technology status and developments of metallic hot structure and thermal protection systems. In Proceedings of the 5th European Workshop on Thermal Protection Systems and Hot Structures, Noordwijk, The Netherlands, 17–19 May 2006. ESA SP-631.
5. Gui, Y.; Yang, P.; Liu, L.; Zeng, L.; Wei, D. Thermal protection issues for reusable high-speed vehicles under combined thermal effects. *Acta Aerodyn. Sin.* **2026**, *44*, 1–8. (In Chinese)
6. Le, V.T.; Ha, N.S.; Goo, N.S. Advanced sandwich structures for thermal protection systems in hypersonic vehicles: A review. *Compos. Part B Eng.* **2021**, *226*, 109301. [CrossRef]
7. Le, V.T.; Han, C.; Goo, N.S. Design assessment of metallic thermal protection system for reentry vehicles: Thermomechanical and impact properties. In Proceedings of the AIAA Scitech 2023 Forum, Online, 23–27 January 2023.
8. Akca, E.; Gürsel, A. A review on superalloys and IN718 nickel-based INCONEL superalloy. *Period. Eng. Nat. Sci.* **2015**, *3*, 15–27. [CrossRef]
9. Fayed, E.M.; Brailovski, V.; Jahazi, M.; Medraj, M. Stability of the microstructure and elevated-temperature mechanical properties of additively manufactured Inconel 718 superalloy subjected to long-term in-service thermal cycling. *Mater. Sci. Eng. A* **2022**, *838*, 142790. [CrossRef]
10. Huang, W.; Li, S.; Yang, X.; Shi, D.; Qi, H. Experimental investigation and modelling of microstructure degradation in a DS Ni-based superalloy using a quantitative cross-correlation analysis method. *J. Alloys Compd.* **2018**, *762*, 488–499. [CrossRef]
11. Boismier, D.A.; Sehitoglu, H. Thermo-mechanical fatigue of Mar-M247: Part 1—Experiments. *J. Eng. Mater. Technol.* **1990**, *112*, 68–79. [CrossRef]
12. Moverare, J.J.; Lancaster, R.J.; Jones, J.; Stekovic, S.; Whittaker, M.T. A review of recent advances in the understanding of thermomechanical fatigue durability and failure mechanisms in nickel-based superalloys. *Metall. Mater. Trans. A* **2025**, *56*, 1115–1134. [CrossRef]
13. Sun, J.; Yuan, H. Life assessment of multiaxial thermomechanical fatigue of a nickel-based superalloy Inconel 718. *Int. J. Fatigue* **2019**, *120*, 228–240. [CrossRef]
14. Le, V.T.; Goo, N.S.; Kim, J.Y. Thermomechanical behavior of superalloy thermal protection system under aerodynamic heating. *J. Spacecr. Rockets* **2019**, *56*, 1432–1448. [CrossRef]
15. Pan, B.; Yu, L.; Wu, D. Thermo-mechanical response of superalloy honeycomb sandwich panels subjected to non-steady thermal loading. *Mater. Des.* **2015**, *88*, 528–536. [CrossRef]
16. Yang, Q.; Gao, B.; Xu, Z.; Xie, W.; Meng, S. Topology optimisations for integrated thermal protection systems considering thermo-mechanical constraints. *Appl. Therm. Eng.* **2019**, *150*, 995–1001. [CrossRef]
17. Brevault, L.; Balesdent, M.; Hebbal, A. Multi-objective multidisciplinary design optimization approach for partially reusable launch vehicle design. *J. Spacecr. Rockets* **2020**, *57*, 373–390. [CrossRef]
18. Peters, A.B.; Zhang, D.; Chen, S.; Ott, C.; Oses, C.; Curtarolo, S.; McCue, I.; Pollock, T.M. Materials design for hypersonics. *Nat. Commun.* **2024**, *15*, 3328. [CrossRef] [PubMed]
19. Zhang, B.; Wang, R.; Hu, D.; Jiang, K.; Hao, X.; Mao, J.; Jing, F. Constitutive modelling of ratcheting behaviour for nickel-based single crystal superalloy under thermomechanical fatigue loading considering microstructure evolution. *Int. J. Fatigue* **2020**, *139*, 105786. [CrossRef]
20. Yin, B.; Zreid, I.; Zhao, D.; Ahmed, R.; Lin, G.; Kaliske, M. Thermomechanical fatigue life prediction of metallic materials by a gradient-enhanced viscoplastic damage approach. *Int. J. Numer. Methods Eng.* **2022**, *123*, 2042–2075. [CrossRef]
21. Li, D.H.; Shang, D.G.; Chen, H.; Cong, L.H.; Wang, J.-J.; Mao, Z.-Y.; Chen, C.-L.; Guo, Y.-E.; Yin, X. Viscoplastic constitutive model considering strain rate sensitivity under multiaxial thermomechanical fatigue loading. *Fatigue Fract. Eng. Mater. Struct.* **2023**, *46*, 1455–1472. [CrossRef]
22. Choi, H.; Lim, H.J.; Yun, G.J. An integrated unified elasto-viscoplastic fatigue and creep damage model with characterization method for structural analysis of nickel-based high-temperature structure. *Int. J. Damage Mech.* **2023**, *32*, 73–102. [CrossRef]
23. Othman, A.M.; Dyson, B.F.; Hayhurst, D.R.; Lin, J. Continuum damage mechanics modelling of circumferentially notched tension bars undergoing tertiary creep with physically-based constitutive equations. *Acta Metall. ET Mater.* **1994**, *42*, 597–611. [CrossRef]
24. Sabnis, P.A.; Forest, S.; Cormier, J. Microdamage modelling of crack initiation and propagation in FCC single crystals under complex loading conditions. *Comput. Methods Appl. Mech. Eng.* **2016**, *312*, 468–491. [CrossRef]
25. Zhang, D.X.; Wang, J.P.; Wen, Z.X.; Liu, D.S.; Yue, Z.F. V-notched bar creep life prediction: GH3536 Ni-based superalloy under multiaxial stress state. *J. Mater. Eng. Perform.* **2016**, *25*, 2959–2968. [CrossRef]
26. Pei, H.; Wang, S.; Zhang, H.; Yu, H.; Shi, X.; Yang, Y.; Wen, Z.; Yue, Z. Oxidation-creep damage assessment of Ni-based single-crystal superalloy and coated system. *J. Mater. Sci. Technol.* **2026**, *260*, 13–29. [CrossRef]
27. Larson, F.R.; Miller, J. A time-temperature relationship for rupture and creep stresses. *Trans. ASME* **1952**, *74*, 765–771. [CrossRef]
28. Lemaitre, J. A continuous damage mechanics model for ductile fracture. *J. Eng. Mater. Technol.* **1985**, *107*, 83–89. [CrossRef]
29. Li, Z.; Zhang, Y.; Zhong, W.; Zhang, Y.; Sun, Z.; Hu, N. Research on the repeated folding mechanism of membrane antennas based on crease endurance degradation. *Int. J. Solids Struct.* **2026**, *329*, 113856. [CrossRef]

30. Guo, K.; Liu, D.; Liao, Y.; Lu, Y. Dynamic response of U-corrugated sandwich plates subjected to repeated slamming loads. *Thin-Walled Struct.* **2026**, *227*, 115065. [CrossRef]
31. Wang, Q.; Hong, Z.; Shen, L.; Shi, L.; Li, L.; Zheng, Q.; Ren, Z. Multiscale analysis of dynamic degradation and fatigue life prediction of slender-strip entangled metallic pseudo-rubber under variable amplitude-frequency loading. *Nonlinear Dyn.* **2026**, *114*, 778. [CrossRef]
32. Li, L.; Zhang, Y.; Ding, R.; Hu, H. Temperature, loading rate and stress triaxiality effects on tensile failure of polymethyl methacrylate (PMMA). *Eng. Fail. Anal.* **2026**, *196*, 111105. [CrossRef]
33. Jin, L.; Jia, S.; Zhang, Z.; An, Z.; Lu, Z. Study on creep mechanical properties of HTPB solid propellant. *Materials* **2026**, *19*, 1951. [CrossRef] [PubMed]
34. Wei, J.; Han, J.; Jia, Y.; Wang, T.; Huang, Q. Evolution of multiscale heterostructures and comprehensive properties improvement in the large thickness ratio Ti/Al/Mg clad plates under heterothermal rolling. *J. Magnes. Alloys* **2026**, *18*, 101863. [CrossRef]
35. Jin, X.; Wang, L.; Zhang, Z.; Guo, Y.; Xia, X. Optimizing L-DED repair of arc-shaped grooves via defocus control: Thermodynamic modeling and aspect ratio-defocus distance matching mechanism. *J. Mater. Process. Technol.* **2026**, *347*, 119147. [CrossRef]
36. Chaboche, J.L. A review of some plasticity and viscoplasticity constitutive theories. *Int. J. Plast.* **2008**, *24*, 1642–1693. [CrossRef]
37. Perzyna, P. Fundamental problems in viscoplasticity. In *Advances in Applied Mechanics: Vol. 9*; Elsevier: Amsterdam, The Netherlands, 1966; pp. 243–377.
38. Editorial Committee of the China Aeronautical Materials Handbook. *China Aeronautical Materials Handbook: Vol. 2, Deformed Superalloys and Cast Superalloys*, 2nd ed.; China Standard Press: Beijing, China, 2002. (In Chinese)
39. Special Metals Corporation. *INCONEL Alloy 718 (UNS N07718/W.Nr. 2.4668)*; Special Metals Corporation: Huntington, WV, USA, 2007.
40. Zhang, L.; Yu, Z.W.; Zhang, L.C.; Jiang, R.; Song, Y.D. Mechanism and numerical simulation of cyclic damage of GH4169 superalloy under thermo-mechanical fatigue. *Acta Metall. Sin.* **2023**, *59*, 871–883. (In Chinese)
41. Ma, Q.; Yu, W.; Chai, Y.; Yang, X.; Li, Y. Modification of the intermediate-temperature stress relaxation behavior and creep constitutive equation of GH4169 alloy. *Mater. Mech. Eng.* **2024**, *48*, 112–120. (In Chinese)
42. Morrow, J.D. Cyclic plastic strain energy and fatigue of metals. In *Internal Friction, Damping, and Cyclic Plasticity*; (ASTM STP 378); American Society for Testing and Materials: Philadelphia, PA, USA, 1965; pp. 45–87.
43. Coffin, L.F., Jr. A study of the effects of cyclic thermal stresses on a ductile metal. *Trans. ASME* **1954**, *76*, 931–950. [CrossRef]
44. Manson, S.S. *Behavior of Materials Under Conditions of Thermal Stress*; NACA TN-2933; US Government Printing Office: Washington, DC, USA, 1953.
45. Dassault Systèmes. *Abaqus 2022 Documentation*; Dassault Systèmes Simulia Corp.: Providence, RI, USA, 2022.

Disclaimer/Publisher's Note: The statements, opinions and data contained in all publications are solely those of the individual author(s) and contributor(s) and not of MDPI and/or the editor(s). MDPI and/or the editor(s) disclaim responsibility for any injury to people or property resulting from any ideas, methods, instructions or products referred to in the content.